RESPONSE OF TENSION PILES TO VERTICAL SEISMIC MOTION IN SATURATED FINE SAND

by

Michael W. O'Neill

Cumaraswamy Vipulanandan

Mauricio Ochoa

December 1989

Phase I Report

for

Minerals Management Service

Amoco Production Company

Exxon Production Research Company

Texaco, Inc.

Unocal, S & T Division

Department of Civil and Environmental Engineering

University of Houston

Report No. UHCEE 89-14

PREFACE / ACKNOWLEDGMENTS

This study was performed by the Department of Civil and Environmental Engineering, at the University of Houston, under contract to the Minerals Management Service; Amoco Production Company; Exxon Production Research Company; Texaco, Inc.; and Unocal, S & T Division.

The authors wish to express their appreciation to the sponsors of this project. The completion of this study was made possible only by the contributions of many at the University of Houston. Special thanks are due:

Roy Henson and Martin Kowis, Civil and Environmental Engineering technicians, for their help during the testing set up,

Mike Irwin, for his help during the programing phase of the testing machine, and

The Engineering Media Center, for painstakingly preparing the figures.

TABLE OF CONTENTS

TABLE OF CONTENTS (Cont'd)

LIST OF TABLES

LIST OF FIGURES

LIST OF FIGURES (Cont'd)

LIST OF FIGURES (cont'd)

LIST OF FIGURES (Cont'd)

LIST OF FIGURES (Cont'd)

LIST OF FIGURES (Cont'd)

CHAPTER I

Introduction

This study addresses the problem of vertical dynamic response of axially loaded piles with tension bias under the vertical component of earthquake loading. Of specific concern are (a) whether the pile loses capacity during the period of strong ground motion and thereby either fails or operates under a lower-than-desirable factor of safety, and (b) if the pile loses capacity, whether that loss is permanent or whether it is regained after the conclusion of the seismic event. While mathematical models exist that can provide computations for these phenomena, very little experimental data are known to exist against which to test these models.

The problem has been studied experimentally using modelling techniques. The response of axially loaded piles with uplift biases have been simulated as accurately as possible under a given set of controlled conditions in the laboratory. Such behavior has been studied for an impact-driven pile in saturated fine sands of varying permeabilities and subjected to the scaled vertical component of a seismic soil motion that has been measured on the seafloor during the Oceanside earthquake (offshore California) of July 13, 1986. Principles of scaling an earthquake to a higher magnitude, and scaling relationships, similar to those applied to centrifuge models, have been utilized in an attempt to simulate the problem more realistically.

Even where the strongest component of soil motion is horizontal, produced by upward propagating shear waves, it is essential to understand whether the potential loss of axial capacity of a pile developed from excess pore water pressures and effective stress changes in the soil due to the vertical component of relative pile-soil motion, or whether such interaction can be effectively neglected. This study provides insight into that issue by defining the magnitude of the effects of vertical soil motion on a pile under biased tension loading.

OBJECTIVES

A laboratory experimental study has been conducted in order to evaluate the effect of several parameters affecting the capacity of axially loaded piles subjected to biased uplift loads in a saturated sand deposit that is subjected to the simulated vertical component of seismic excitation. Generally the zone of greatest susceptibility to loss of side shear capacity is the uppermost 40 ft of pile penetration, where mean ambient effective stresses in most offshore sand deposits are 5 psi or less. In that zone soil stress waves can produce pore water pressures that are a significant percentage of the in-situ effective stresses (inducing near-field and/or free-field liquefaction). Therefore, this study is focused on simulation of pile-soil interaction in that zone, which has been accomplished by placing a pile segment in an isotropically pressurized chamber in which mean initial effective stresses of 2.5 and 5.0 psi (corresponding to pile penetrations of 20 and 40 ft, respectively) were applied. The pile segment to be tested simulates only that portion of the pile in the zone of interest.

The particular event chosen for this study was the Oceanside event of July 13, 1986, a Richter Magnitude 5.8 earthquake whose epicenter was 74 km southeast of the instrumentation site from which the data were acquired, known as the "SEMS" site. This moderate event appeared to produce a typical record for an offshore California earthquake. The SEMS unit was a three dimensional accelerometer buried in sediments 5 feet below the mudline off the coast of Long Beach, California. The site is a deep, soft soil site, as characterized in Appendix A. Low peak accelerations of the vertical component (3-4 milli-g's) suggested no loss of pile capacity . Therefore, the actual earthquake was scaled to a higher magnitude, i.e., Richter Magnitude 8.0. Furthermore, scaling effects of the small-scale prototype were considered.

The specific parameters investigated were:

(a) Magnitude of mean initial effective pressure in the sand (prior to pile driving),

(b) Ratio of static uplift bias load to peak static uplift capacity,

(c) Relative density of the sand, and

(d) Type of static loading tests (controlled displacement test or controlled load test).

In order to scale the effect of drainage distance and its effect on pore pressure generation and dissipation, both the earthquake frequency and soil permeability were also scaled in some tests.

Components of behavior that were investigated were:

(a) Dynamic uplift capacity of the pile during simulated seismic motion for selected combinations of the above parameters (i.e, under what conditions does the pile fail by pull out during the simulated seismic event?), and

(b) Residual static uplift capacity of the pile after the simulated seismic event (i.e., capacity under monotonic uplift loading).

The controls (non-variables) were the follows:

(a) Length (embedment) of the pile segment,

(b) Degree of saturation of the test sand (100%),

(c) Pile segment shape (circular steel pile with closed end and uniform diameter and wall thickness), and

(d) Method of pile insertion (impact driving).

The information developed should provide practical guidance concerning the permissible tension bias loads that can be sustained by piles in fine saturated sand for the seismic event that is modelled and by reference to typical Magnitude 8 California-type seismic events.

RESEARCH APPROACH

The response of piles loaded in biased uplift to the vertical component of a Magnitude 8 seismic event was studied systematically using experimental modelling. The soil stresses were simulated to ground stresses in a saturated pressure chamber under various parametric conditions. The general sequence of testing was as follows. A given set of soil conditions were duplicated within a pressurized test chamber for each individual test. Several static uplift load tests were conducted on piles driven into the saturated soil in the chamber to develop a consistent relationship between penetration rate (blow count per inch) and static pull out capacity.

Dynamic tests were then conducted in which the pile was driven into the pressurized chamber and its static uplift capacity evaluated from the penetration rate. A given ratio of static biased load to static capacity was then applied to the pile through a one-degree-of-freedom weight and spring system to model a long-period structure to which the pile was secured, and the simulated earthquake was applied to the base of the chamber

through a servo-controlled testing machine. If the pile failed during the simulated earthquake, no further testing was done. If the pile did not fail, additional static load was applied at the conclusion of the dynamic test to determine whether the post-earthquake static capacity was reduced from the static capacity that was inferred from the driving rate. In this manner the ratio of biased load that could be present on the pile to the pile's static capacity without producing failure during the seismic event could be determined.

The remaining chapters in this report describe the details of the testing apparatus, the test results and the conclusions developed from the study. The testing sequence performed to achieve the stated objectives is shown in Table 1.1. A relatively large number of baseline (static) tests (A1-F) were conducted to confirm the repeatability of the static uplift capacity, to define appropriate failure criteria and to assess the sensitivity of the static uplift capacity to relative density and mean effective stress in the soil mass. In order to investigate failure criteria, both controlled load (CL) and controlled displacement (CD) tests were conducted during the static phase of testing. The dynamic tests (G-N2) were then performed under conditions identical to those that existed in the static tests.

Table 1.1. Testing Sequence

Test No.	Type of Test: Static (Base Line)/ Dynamic	Type of Static Loading: CD/CL[e]	Condition: Dr(%)/σ_c (psi) / Q bias (lbs)
A1	Static	CD	55 / 5 / 0
A2	Static	CD	55 / 5 / 0
A3	Static	CL	55 / 5 / 0
B1	Static	CD	70 / 5 / 0
B2	Static	CL	70 / 5 / 0
C	Static	CD	78 / 5 / 0
D	Static	CD	85 / 5 / 0
E1	Static	CD	55 / 2.5 / 0
E2	Static	CL	55 / 2.5 / 0
F	Static [a]	CL	55 / 5 / 0
G	Dynamic	CD	55 / 5 / 60
H1	Dynamic	CL	55 / 5 / 123
H2	Dynamic	CL	55 / 5 / 80
I1	Dynamic	CL	55 / 5 / 156
I2	Dynamic	CL	55 / 5 / 243
J	Dynamic	CL	70 / 5 / 228
K	Dynamic	CL	70 / 5 / 335
L1	Dynamic	CD	55 / 2.5 / 184
L2	Dynamic	CL	55 / 2.5 / 87
M1	Dynamic [a,c,d]	CL	55 / 5 / 100
M2	Dynamic [a,c,d]	CL	55 / 5 / 160
N1	Dynamic [c]	CL	55 / 5 / 111
N2	Dynamic [c]	CL	55 / 5 / 214

a. Tests conducted with micro-fine sand[b]. Other static tests conducted with standard test sand (SJR sand).

b. Sand with a coefficient of permeability approximately 0.12 times that of SJR sand (standard test sand) to scale drainage distance.

c. Time scaled by a factor of 0.14 in the acceleration record to scale drainage distance and other length factors.

d. Accelerations scaled by a factor of 7 in the acceleration record.

e. CD refers to a controlled displacement test. CL refers to a controlled load test.

CHAPTER II

Background

The dynamic response of axially loaded piles has been the focus of considerable research, both analytical and experimental, for several years. Mathematical models that that the supporting soil as linear, viscoelastic media are presently in use (1,2,3), although most applications have been in the area of machine foundations. However, nonlinear solutions more suitable to the analysis of piles during seismic events have been developed recently. One class of such model considers radiational damping through the soil in a generally rigorous way (4), while another class requires that assumptions be made regarding radiation damping but which models near-field hysteretic damping accurately based on time series response of nonlinear unit load transfer curves ('t-z' curves) (5). In the latter, it is possible to replicate seismic events through specified time-motion history of the free-field soil (physically, motion of the supports for the nonlinear springs that model the t-z curves). However, effects of losses in pile-soil shearing and base resistance during the event due to cyclic loading must be supplied by the user of the method and hence are presumed to be at least approximately predictable. The primary use of the mathematical models described in Refs. 4 and 5 has been to model problems in which dynamic load is applied through the pile head and/or where assumed degradation models have been applied to the soil undergoing seismic excitation. The objectives of these analyses have generally been to develop dynamic response curves for foundations in order to permit analysis of the superstructure and not specifically to model the capacity of the pile during loading.

Some experimental data exist against which to test the mathematical models, but most of the experiments have not simulated earthquake loading or have not included one or more important variables. The most reliable data are those developed under conditions in which the effective stresses simulate those found in situ, that is, either full-scale field tests or tests conducted in a centrifuge. For example, full scale experimental studies of piles subjected to harmonic dynamic loads large enough to impart nonlinear behavior have been reported (6,7,8), and recent attempts have been made toward applying measured soil base motion response to piles and pile groups in dry sand in the centrifuge (9). A study by Scott et al. (8), which involved only lateral pile-head excitation, indicated that liquefaction (and instantaneous reduction in soil reaction) may have been induced by pile head-loading in a

saturated fine sand. Except for this study, none of the referenced studies was conducted to loads large enough to produce significant degradation of capacity.

Another source of data are laboratory and field tests that have been performed on piles to a sufficient magnitude of combined cyclic load and static bias load to produce failure. Most of these tests have been conducted under a slow rate of loading. The results may be misleading regarding their application to earthquake problems, therefore, because rapid, high-amplitude, cyclic axial loading tends to produce two counteracting effects: (a) loss of capacity, principally in skin friction (10, 11), and (b) increase in capacity due to viscoelastic effects (14,15,18). Studies show, however, that the net capacity loss (i.e., degradation) occurs in both cohesive soils (12,13) and cohesionless soils (11). Studies have also indicated that relative motions between the pile and soil required to initiate cyclic degradation are approximately equal to the relative displacement required to initiate side shear failure in static loading (10).

Holmquist and Matlock (12) determined from slow cyclic test in soft clay that one-way loading produced less severe degradation than two-way loading and recommended an envelope unit load transfer curve that terminated at 0.67 times the static ultimate capacity for one-way loading and at 0.33 times the static capacity for two-way loading. Karlsrud et al. (13) independently arrived at similar conclusions for piles in overconsolidated clay in the field and further observed that large-amplitude, post-failure loading produced additional degradation in available side shear to about 30% of its static value. In low-plasticity, overconsolidated, cohesive glacial till, McAnoy et al. (16) observed that piles tested with a tensile bias of 40% of the static uplift capacity and a superimposed cyclic load of 40% of the static uplift capacity produced a degradation of about 20% in average ultimate unit side shear after application of over 500 cycles of load. With lower amplitudes of either static bias or cyclic load, insignificant loss of capacity occurred with in excess of 13000 cycles of applied load.

In sands, Poulos (10,11) found that short, stiff piles suffer degradation sooner and degrade more severely than long, flexible piles, and that degradation of skin friction in calcareous sands tends to be more severe than in siliceous sands (in the range of 25% loss of capacity in siliceous sands and 50% loss in calcareous sands). Poulos (10) also found that neither the soil modulus nor the ultimate base bearing capacity appeared to be seriously affected by cyclic loading. Chang and Hanna (17) performed one-way cyclic loading tests on laboratory model piles in dry medium dense sand to a large number of cycles. They

found that pile behavior was highly dependent on the magnitude of the repeated load and that pile failure could occur with cyclic loads of 30% of the ultimate static load. They also found that one of the effects of repeated loading was to cause a redistribution of loads from the shaft to the base.

Separate sources of data providing information about the effects of capacity gain due to rate-of-loading effects (14,15) suggest that axial pile capacity increases by about 5% per log cycle decrease in total time to failure in clay, suggesting that load excursions at primary earthquake frequencies could produce capacity increases relative to static capacity, of perhaps 20 to 30% in the absence of cyclic degradation. In sands, the effect appears to be slightly less pronounced (15).

Since the data from slow cyclic tests suggest losses due to cyclic degradation of from 20 to 70% of static capacity, and data from rate-of-loading studies suggest that viscous loading effects will independently produce gains in capacity of 20 to 30%, it would appear that, if the result of the two type of studies can be superimposed, earthquake frequency loading could produce a net loss of capacity, provided that the induced amplitude of relative pile to soil displacement during the seismic events exceeds perhaps 10% of pile diameter, the approximate value required to initiate static side shear failure.

Other factors, however, also appear to be relevant when considering the response of axially loaded piles to seismic excitation. Stress waves in a saturated granular soil can produce either liquefaction or cyclic mobility in the free field which, when superimposed on the effects of cyclic pile motion described above, may further reduce the capacity of the pile. Liquefaction and cyclic mobility phenomena have been extensively investigated during the last two decades (i.e, 19, 20, 21). Liquefaction denotes a condition where soil will undergo continued deformation at a constant low residual resistance or with no residual resistance, due to the build-up and maintenance of high pore water pressures which reduce the effective confining pressures to a very low value. Cyclic mobility denotes a condition in which cyclic shear application produces a condition of initial liquefaction and subsequent cyclic stress applications cause limited strains to develop either because of the remaining resistance of the soil to deformation or because the soil dilates, which causes the pore water pressure to drop, and the soil to stabilize under the applied loads. Liquefaction has been observed in situ on many occasions (i.e, 22,23) and it has been reproduced in the laboratory (24,25). Generally, liquefaction appears not to occur when shear strains (γ) induced by loading are less than 0.01 per cent. In laboratory undrained cyclic tests (triaxial,

direct simple shear) on saturated sand, cyclic mobility has been observed to develop and to result in large strains (26,27). Available computer programs, such as SHAKE (32), can be used to evaluate the dynamic response of a soil deposit . In SHAKE, the soil deposit is modelled as a system of homogeneous, visco-elastic layers of infinite horizontal extent subjected to vertically propagating shear waves. The evaluation of liquefaction potential of the free-field soil can be accomplished by using either the simplified procedure developed by Seed and Idriss (33) or a computer program APOLLO (34) for the analysis of generation and dissipation of pore pressures with time in horizontal sand layers during cyclic or earthquake loading. Using today's design practice, for instance, in a nonlinear seismic response analysis of a jacket platform founded in liquefiable soil in the Adriatic sea, Vanzini, et al.. (35) evaluated the soil-pile behavior by considering the free-field and the near-field liquefaction potentials separately, and subsequently incorporated them into the soil-pile-structure interaction analyses. Very few attempts have been made to study how liquefaction and/or cyclic mobility interact with cyclic degradation due to relative pile-soil movement to affect pile capacity, especially in uplift. In one experimental study, De Alba (28) reported that the capacity of piles in small scale (either single or within groups) in saturated sand during simulated strong seismic motion in the laboratory was reduced in proportion to the ratio of induced pore water pressure to the initial effective stress in the sand mass when the sand was loaded horizontally. No attempt was made to scale length or to model the seismic signature of a specific event or class of events.

It would therefore appear that any serious experimental study of the seismic axial response of piles in granular soils should include the effects of pile-soil degradation due to both relative pile-soil movement and to the build-up of excess pore water pressures in the free field that are generated by the seismic motion. These effects could best be simultaneously modelled by conducting tests in which the soil, and not the pile, is excited. Such is the manner in which the present experiments were conducted.

The response of the pile to soil-induced excitation depends on the characteristics of the ground motion, the dynamic characteristics of the pile and the superstructure that the pile supports and, possibly, to the direction and magnitude of any biased load on the pile. Some modern offshore structure concepts, such as tension leg platforms (TLP's) and compliant tower frames, require that piles be designed with biased quasi-static uplift loads (e.g., 29). The fundamental periods of framed structures are usually in the range of 0.2 to 0.5 seconds (rotational motion producing push-pull action in the piles) (14), while those for TLP's are somewhat higher. Components of ground motion having similar periods are

present in most seismic events, particularly where deep deposits of soil exist above a rock base (31). The presence of these components may produce magnification of structural loads that can potentially feed back into the pile and affect its response. However, Takashi et al.. (30) have recently published a study of measured response of piles supporting a large bridge in Japan to real seismic events. They concluded, through back-analysis of the data, that while superstructure feedback influenced pile response, the response of the piles was governed more significantly by direct ground motion. These results suggests that this experimental study should focus on excitation of the pile through the soil and that simulation of the soil motion only, independent of the specific details of the superstructure feedback response, is a reasonable testing condition for the pile. Superstructure feedback was simulated in a very simple and generic manner by applying the biased tension load through a dead weight-spring system having a period of approximately 1.0 second.

CHAPTER III

Description of Testing System

The complete testing system described in this chapter includes the test chamber / loading system, test pile, soil instruments, drop hammer, data acquisition system, sand placement and calibration constants. Fig. 3.1 provides a picture of the testing arrangement, which is shown in schematic form in Fig. 3.2.

TEST CHAMBER / LOADING SYSTEM

The test chamber, consisting of 3 separate pieces (3/4-in.-thick top and bottom plates and a 1/4-in.-thick containment cylinder, all made of aluminum) is shown in Fig. 3.3. The assembled test chamber was 22.2 in. in height and 24 in. in diameter. Top and bottom plates were attached to the containment cylinder by eight equally-spaced, 1/2-in-diameter threaded rods. A rubber membrane, 1/8-in. thick, folded to the inside of the cylinder and sealed to the outside by hose clamps, provided uniform lateral confinement to the soil inside the chamber, while a separate pressure membrane (pancake bladder), affixed to the underside of the top plate, provided the vertical confinement. Appropriate sealing was obtained when the cylinder (with the folded membrane) was inserted in a 1/2-in. groove in each end plate and the bolts tightened. A perforated metal diffusion ring at the base of the chamber was used to flush the sand with carbon dioxide immediately after it was placed in the dry. Such flushing reduces the concentration of nitrogen in the soil pores, which tends to form air bubbles in the soil pores when the soil is saturated. Once this process had been completed, deaired water was introduced into the specimen through the same ring. It was allowed to rise slowly within the soil column until the specimen was saturated.

Two quick connectors were placed through small holes on opposite sides of the chamber to serve as pressure ports for the lateral membrane. As the soil was placed into the chamber, the membrane remained collapsed, allowing the chamber wall to retain the deposited soil with zero lateral strain, thus preventing changes in the density in the soil mass during deposition. Once the chamber was charged and saturated, air pressure was

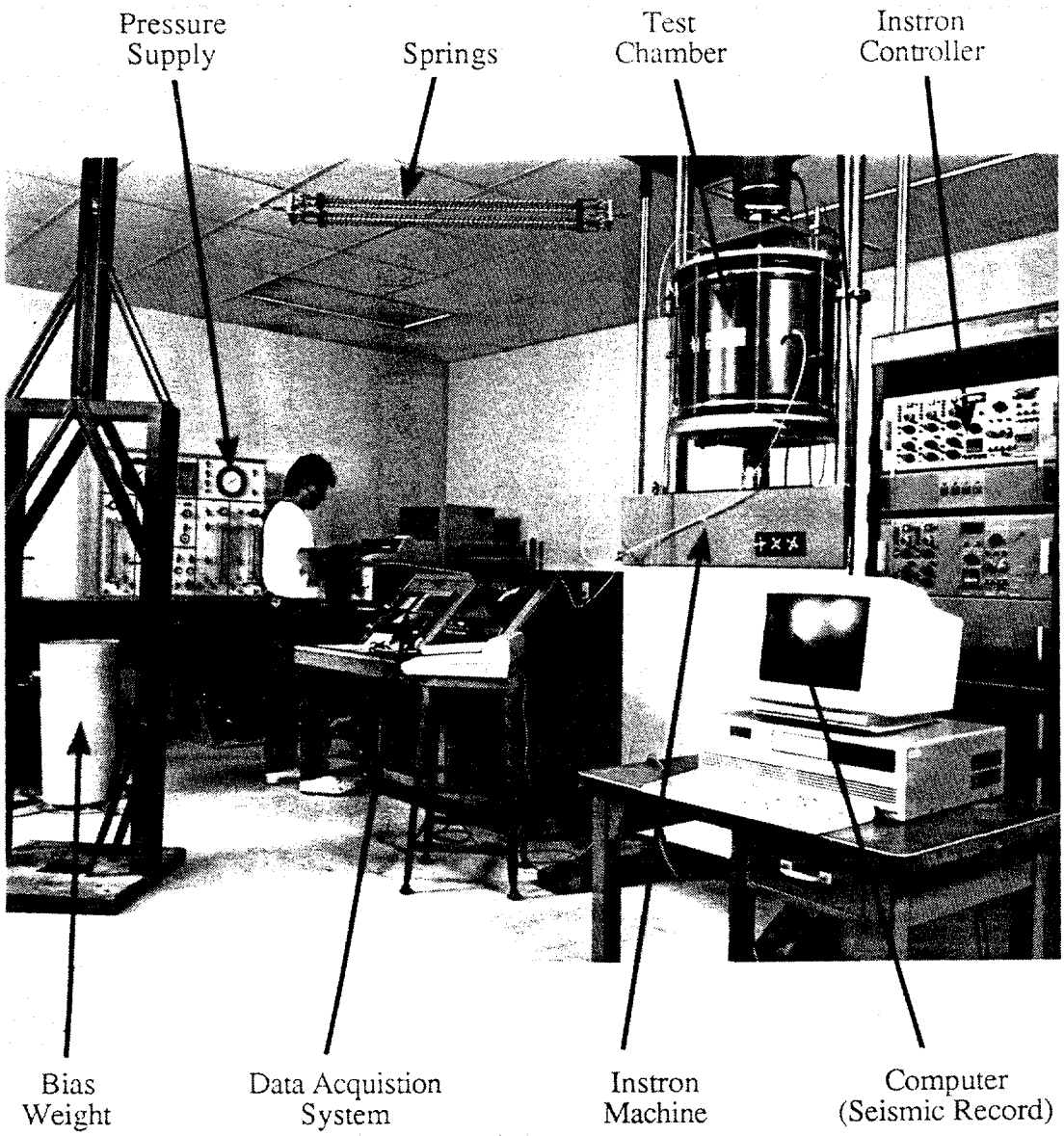

Fig. 3.1. Overall Testing Arrangement

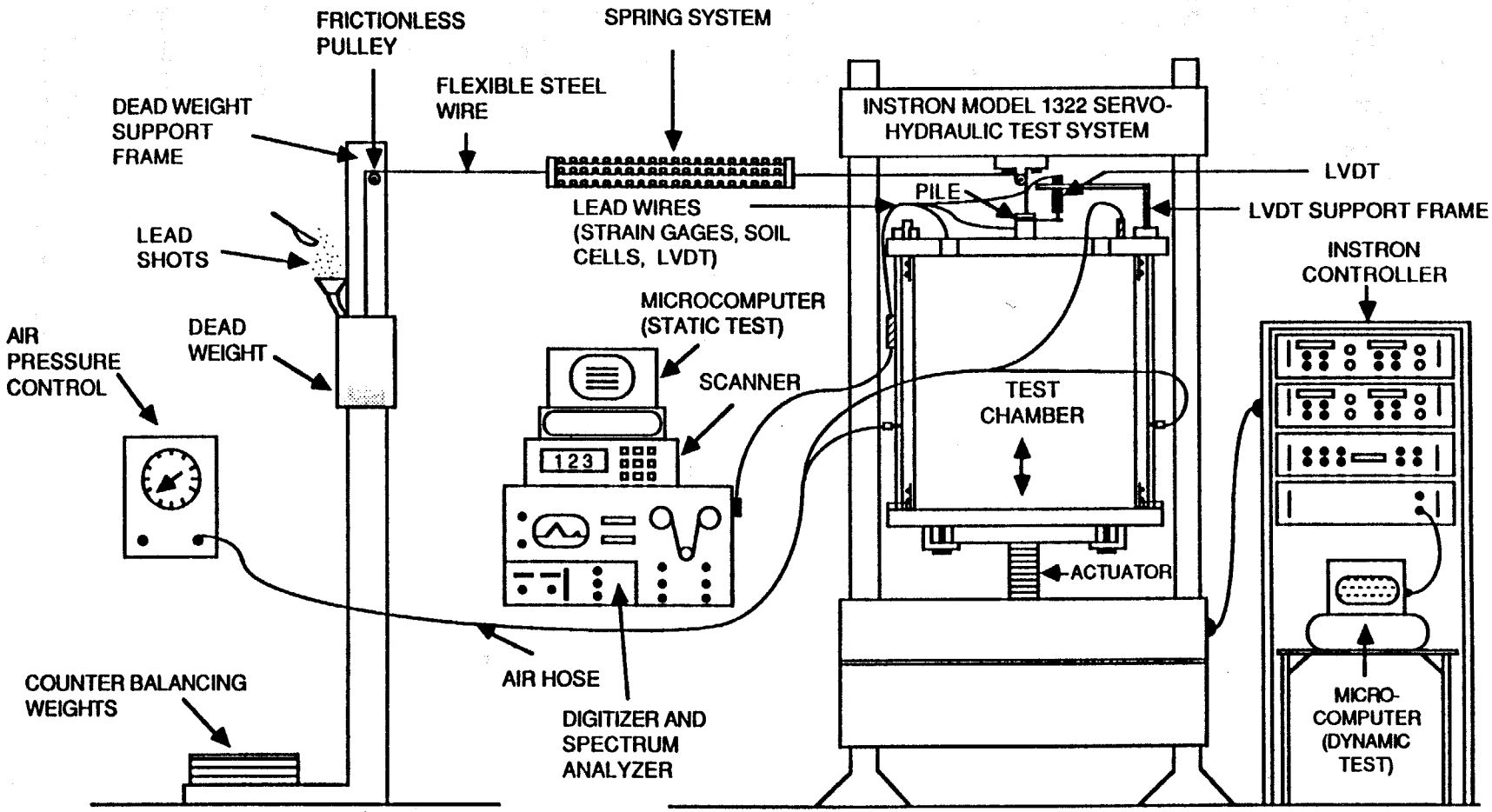

Fig. 3.2. Schematic of Testing Arrangement

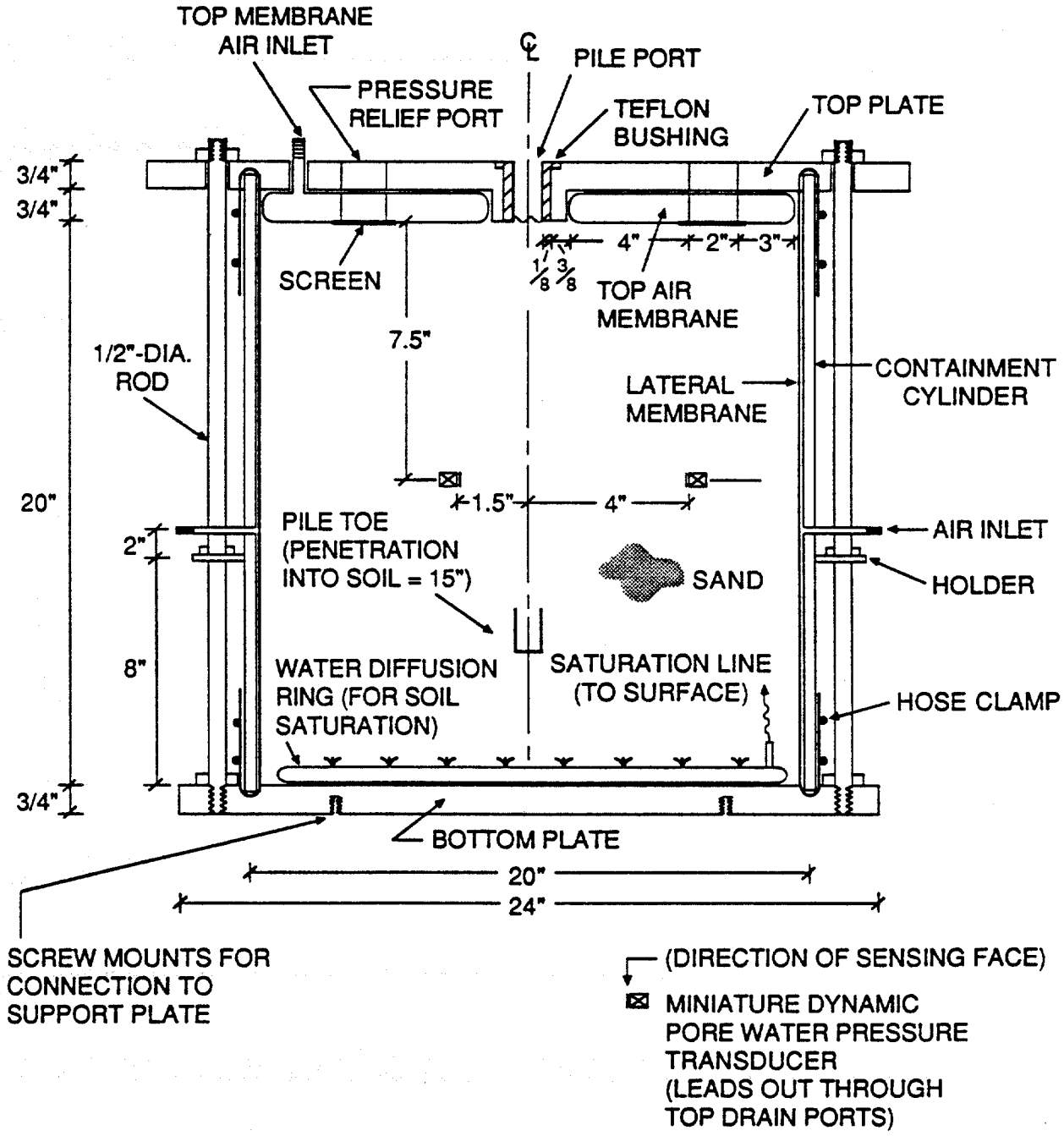

Fig. 3.3. Schematic Elevation of Test Chamber

applied to the lateral membrane that allowed it to lift slowly off the sides of the chamber a distance sufficient to produce a controlled total stress condition at the lateral boundary during subsequent testing.

The top of the chamber, and the top of the soil column, was drained by means of six ports in the top plate: four drainage ports, one port for the pile (which was not pressure tight) and one port that allowed for passthrough of the single air valve for the top membrane.

Dynamic loading was applied to the base of the chamber containing the biased-tension-loaded pile through an Instron (TM) servo-controlled testing machine that was programmed to follow a prescribed vertical deflection time history, defined by the scaled earthquake of interest.

The boundary conditions for the internal surface of the test chamber can be summarized as:

Top: Controlled effective stress, with drainage;
Sides: Controlled total stress, no drainage; and
Base: No drainage, no relative soil chamber motion.

The condition of upward flow of water through the soil pores during simulated seismic activity (an important factor in liquefaction in loose soils) has been permitted.

Figure 3.4 provides a simplified schematic of the types of waves that can be expected in the soil with the existing test system. The imposed vertical base motion produces upward-propagating compression waves, which, in turn, serve both to excite the pile and to generate excess pore water pressures in the free-field soil. Relative motion is allowed to develop between the pile and the soil, which produces radially propagating shear waves (primarily) which may further produce excess pore water pressures and otherwise degrade the pile/soil resistance. The ratio of chamber radius to pile radius of 10 and the presence of a flexible lateral membrane minimize the effects of boundary reflections.

Static uplift tests were conducted on the model pile driven into the chamber by controlled load (CL) and controlled displacement (CD) methods. The definition of static failure load was not straightforward, and the mechanism of failure in static uplift had to be investigated. The fundamental problem is illustrated in Fig. 3.5. If a pile in the chamber is subjected to a static load test in which the load Q is applied under conditions of controlled

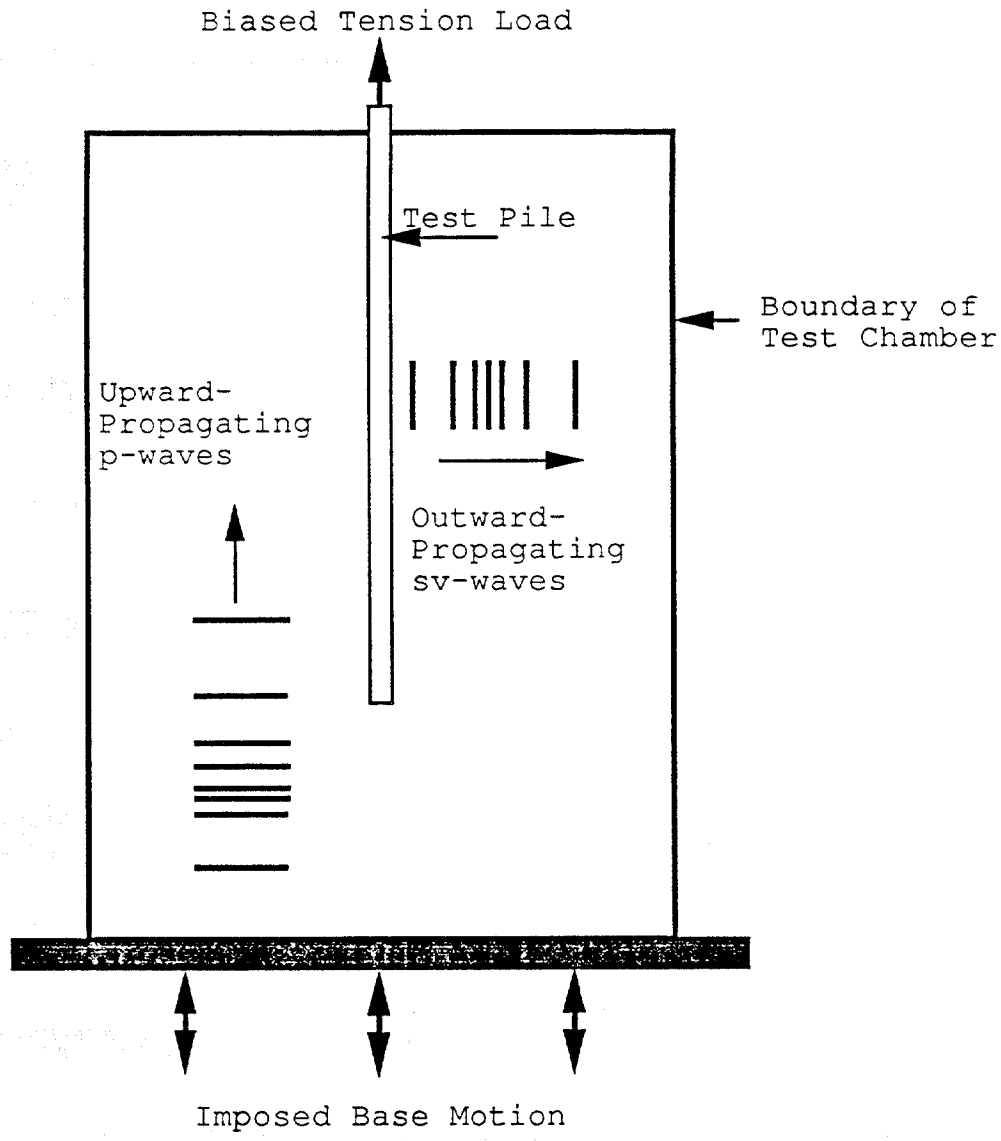

Fig. 3.4. Idealization of Waves in Test Chamber

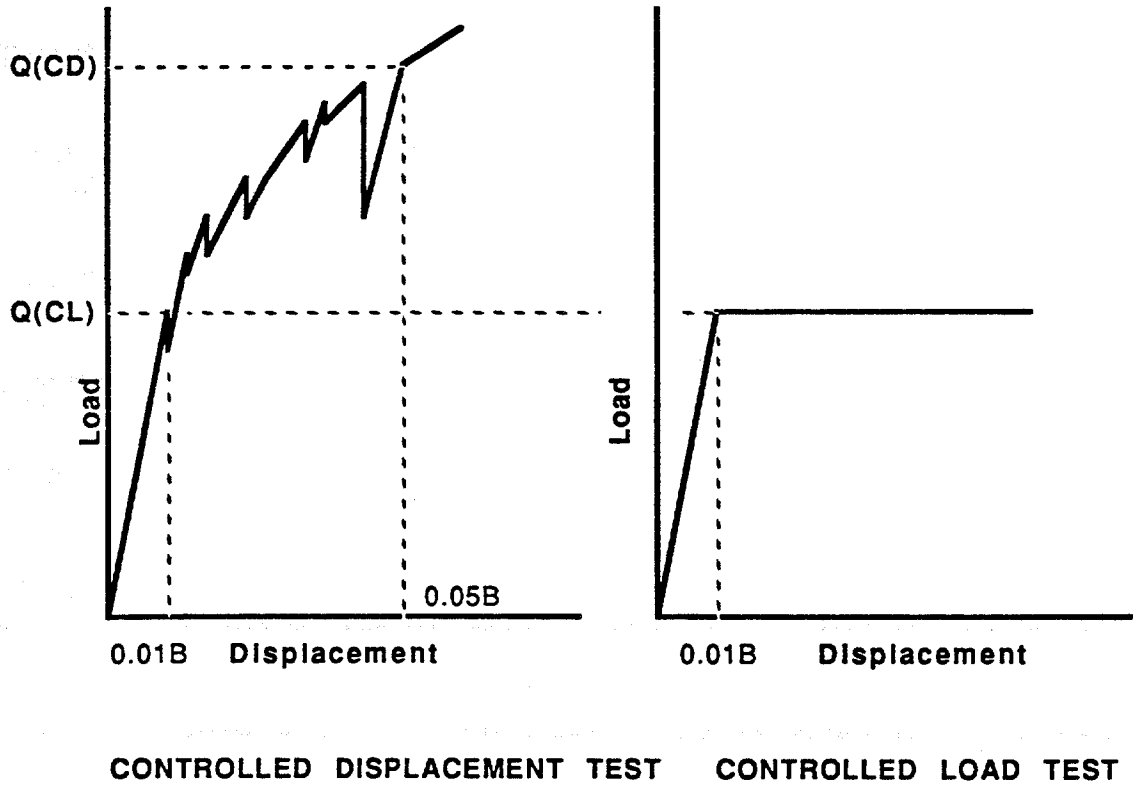

Fig. 3.5. Schematic Comparison of Baseline Static Capacities from Controlled Displacement (CD) and Controlled Loading (CD) Tests

displacement (CD), the load movement relation on the left is produced. Initial slippage occurs when static friction first develops into sliding friction. But sliding friction is quickly arrested because the pile loses elastic energy and becomes less elongated, allowing static friction to once again develop, after which further frictional capacity is realized. This cycle is repeated perhaps several times, each of which results in a slight increase in uplift capacity following minute amounts of slippage. In a controlled load (CL) test (which represents many conditions of loading, such as loading from a tension leg platform (TLP), better than the CD test), depicted on the right side of Fig. 3.5, no opportunity for arresting initial sliding friction exists, and pullout occurs at the time that initial sliding friction develops. The result of this behavior is that CL tests appear to produce lower capacities than those obtained from CD tests. The decision was made at the completion of the static tests to define failure in uplift from the CL tests rather than the CD tests.

The loading system for CL tests (Figs. 3.1 and 3.2) consisted mainly of a flexible high-strength cable, 1/16"-in. thick, a threaded steel plug inserted into the pile head, a simple steel loading frame, a flexible spring system (need for the dynamic tests), two frictionless pulleys made of brass (one supported by the Instron's frame and the other supported by the loading frame), a plastic container, lead shots poured into the container acting as dead weight, and a funnel used to control the loading rate (16 lb/min). Stability of the loading frame was assured by the presence of counterbalancing weights placed on an extended arm welded to the base plate of loading frame. Static post-shaking CL tests were performed by adding more weight (lead shots) into the plastic container until the pile failed. The ratio of spring constant in the static load application system to bias weight was always such that the resonance period of the weight-spring system was 1-2 seconds, which was selected because it is in the general range of the lowest fundamental frequency of typical compliant offshore structures.

For the preliminary static CD tests, the pile head was affixed to the Instron's load cell and the actuator engaged to provide a controlled displacement rate of 0.0033 in./min. For CD tests, conducted after dynamic tests, the bias load was applied by the dead-weight-spring system and held during the dynamic portion of the test, after which the Instron's actuator was used to apply the additional load to fail the pile in the post-shaking static test.

TEST PILE

This section describes the reusable model test pile that was employed during this entire study. The choice of the diameter of the pile and chamber represented a compromise between minimizing scale effects between maximum sand particle size (which was 1 mm in the case of the coarsest sand used in the chamber tests, San Jacinto River Sand) and minimizing pile size utilizing a minimum pile diameter-to-soil particle size ratio of 20 to reduce particle scale effects, resulted in the choice of the 1.0-inch-diameter pile. The diameter of the test chamber containing the sand was limited by the presence of lateral supports of the Instron testing machine, resulting in a 20-in.-diameter test chamber and a test chamber-to-pile diameter ratio of 20. With this test chamber-to-pile diameter ratio, some boundary effects may have occurred in the chamber, although they would have been minimized by the flexible boundary (lateral membrane) that was employed.

A longitudinal view of the closed-ended pile is shown in Fig. 3.6. The pile, 1.0 inch in diameter and having a 0.05 wall thickness, was constructed of drawn, seamless steel tubing. The pile was divided into four segments to facilitate the placement of the strain gages and then reassembled as a unit using the inside threads in every end of each segment. The threads in the uppermost segment (head) of the pile were used to attach a loading plug to a flexible cable from the loading system. The total length of the pile was 17.5 in., with an effective penetration into the soil of 15 inches. 1.5-in. section of the pile was in frictionless contact with a Teflon bushing in the top plate to assure the verticality of the pile during driving. The top 1.0 in. was encase within the anvil during the driving operation and remained exposed above the chamber during a test. After every test, minor grease and rust deposits were removed from the outside wall of the pile by rubbing the pile with emery cloth impregnated with a degreasing substance to assure the uniformity of the potential shear surface along the outside of the pile.

The pile instrumentation was placed permanently on the pile prior to the first test and remained on the pile throughout the entire study. Three levels of strain gages were placed in the pile wall, as shown schematically in Fig. 3.6. Each level was a full-bridge circuit. The levels are denoted by the numeral "1-3." All three levels were read before and during the pile installation, and during the static and dynamic tests to develop static and dynamic load transfer curves. At each gage level, two linear strain gages were epoxy-bonded to the inside of the pile wall and situated 180^{o} apart. The two gages were wired as active gages in a Wheatstone bridge, permitting the cancellation of any bending stresses that

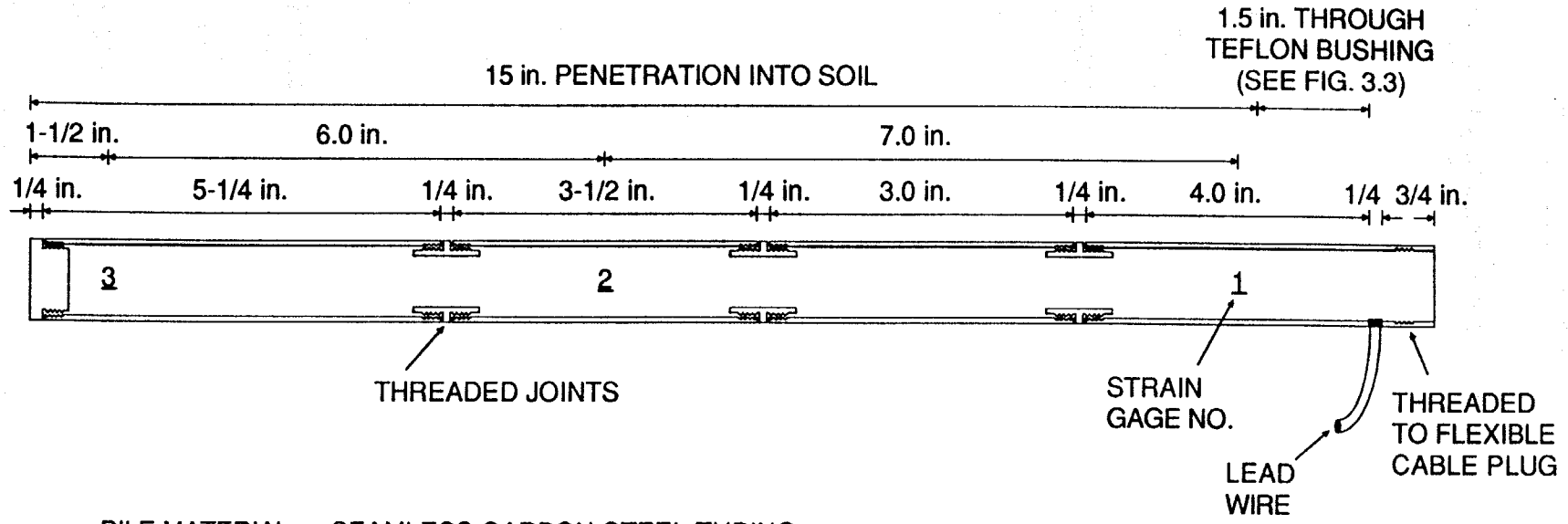

Fig. 3.6. Longitudinal Cross-Sectional View of Test Pile

might have been inadvertently applied to the pile and simultaneously doubling the sensitivity of the circuit to axial stress. The dummies for this bridge were precision resistors placed directly outside the test chamber to avoid differences in temperature with that of the active gages on the pile. Lead wires for the active gages were carried through the inside of the pile to a plug that could be connected with a mating plug from the data acquisition system. The bridge circuits were completed outside the pile using the external dummy resistors.

SOIL INSTRUMENTS

Two miniature pore water pressure transducers were embedded in the soil mass, one near the surface of the pile and one in an area influenced mainly by free-field effects as shown in Fig. 3.2. These transducers which had approximately the same mass as the soil they displaced, consisted of a simple crystal silicon diaphragm with a fully active strain gage bridge diffused into the surface. In order to resist the effective stress of the soil a ceramic porous plate was place in front of the diaphragm. Dimensions of the miniature pore water pressure transducers are given in Fig. 3.7.

Since these instruments are required to be fully saturated at all times, the test chamber was filled to the level in which each of these instruments had to be placed (Fig. 3.2) and the soil saturated. Soil deposition, density control and saturation procedures are described later in this chapter. Each instrument was then placed by hand slightly embedded in the saturated sand in its designated orientation (facing the pile). Some wet sand was then carefully placed and slowly tamped directly above the instruments to attempt to produce the same density at the recording faces of the instruments as existed in the general soil mass. Raining then continued followed by completion of saturation. Lead wires were brought directly to the side of the chamber and up the the inside surface of the chamber to the top, where they were brought out under the top plate and fed directly to the data acquisition system.

DROP HAMMER

A schematic of the hand-operated, single-acting drop hammer is given in Fig. 3.8. The hammer, consisted mainly of an 11.2-lb ram, an aluminum cylinder to guide the ram, plywood cushions and an anvil. The free-fall distance of 15 inches produce an average rate

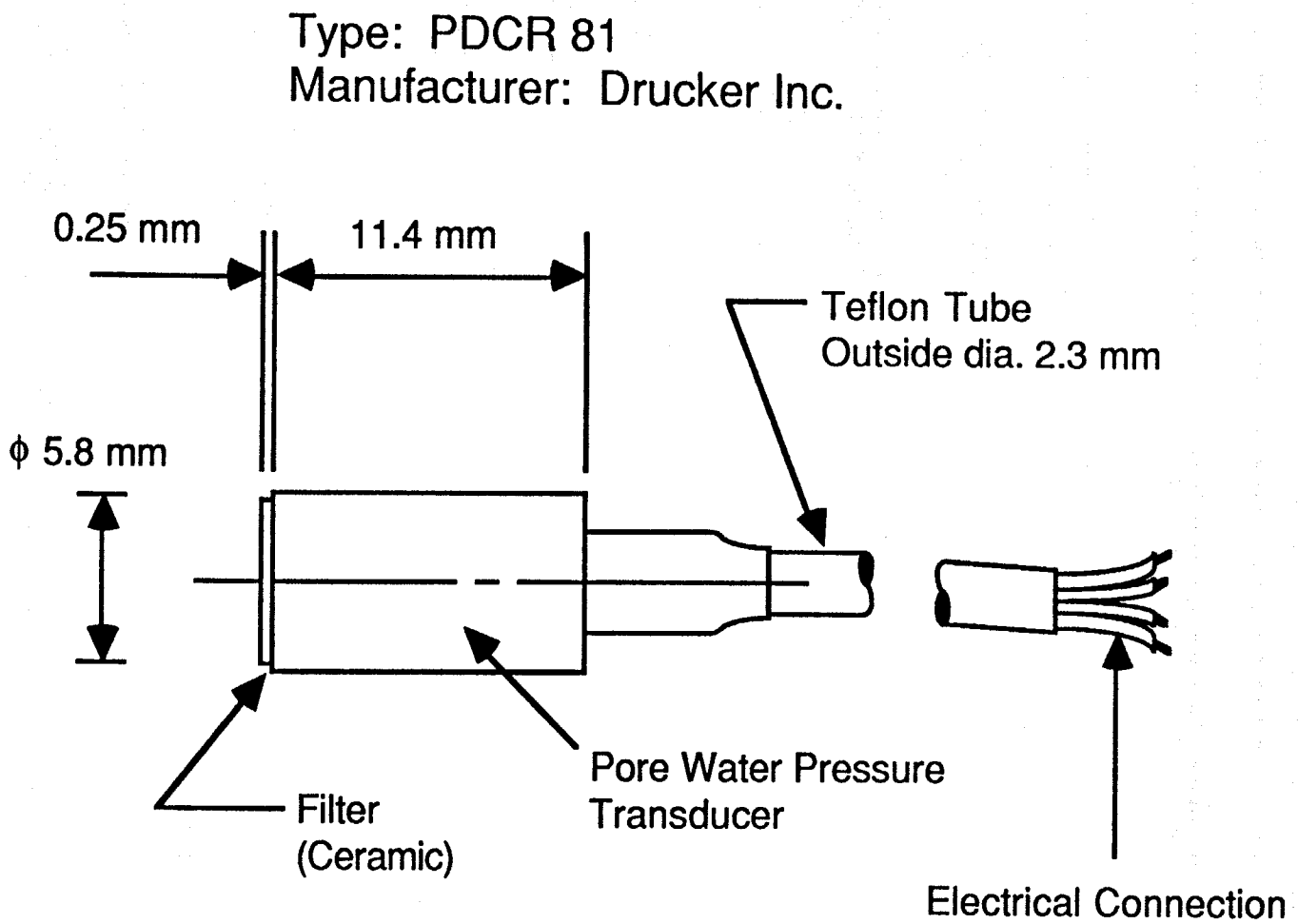

Fig. 3.7. Dimensions of Miniature Pore Water Pressure Transducer

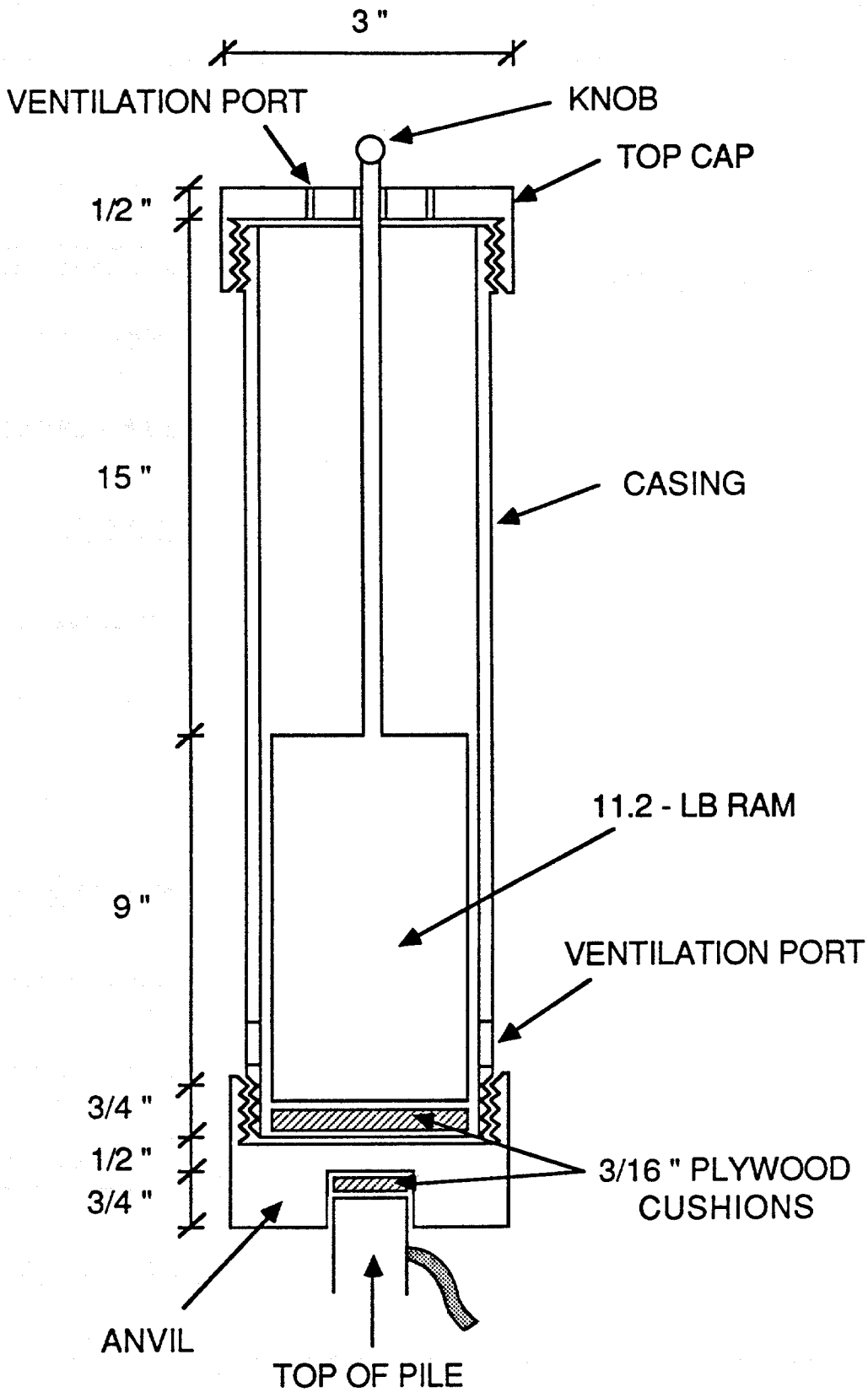

Fig. 3.8. Schematic of Drop Hammer

of penetration of 8 blows per inch for a relative density of 55% and applied confining pressure of 5 psi. At full stroke the operating speed of hammer was approximately 25 blows per minute. Ventilation ports at top and bottom allowed the air to escape during the hammer operation. The cushions consisted of plywood sheets, 3/16-in. thick. The cushions in contact with the ram did not appear visually to have suffered crushing during driving. Cushions in contact with the pile were replaced about 4 times (every 4 inches) during driving to protect the pile-head from damage. A photograph of the pile being installed with the pile-driving system is shown in Fig. 3.9.

DATA ACQUISITION SYSTEMS

Two separate data acquisition systems were used during testing: one for the acquisition of dynamic data during pile installation and the dynamic test, and one for the static uplift test and the static part of the dynamic test (monitoring of static bias load and static post-shaking test to failure).

Dynamic Data Acquisition System

The dynamic data acquisition system is shown in schematic form in Fig. 3.10. During the pile installation and simulated seismic events, the following time series data were recorded on an eight-channel analog magnetic tape recorder: top (pile head), middle and toe strain gage outputs in the pile, near-field and free-field pore water pressures, pile displacement (during shaking tests), and rate of penetration and start/stop events during seismic tests (on the voice channel). Acoustic time marks were placed on the voice channel during pile driving. An observer indicated the passage of various depth marks on the pile past the top of the top plate of the test chamber, which tied the data on the other channels to a particular penetration into the chamber. Acoustic time marks were also employed during the seismic tests. The tape recorder was run continuously during every dynamic test, and during the pile installation of two tests.

The resulting data tapes are recordings of voltage outputs for the various instruments on the channels that are indicated in fig 3.10, and are valid for a tape speed of 7.5 inches per second. The voltages that are recorded on those tapes were multiplied by the appropriate instrument calibration factors to obtain engineering units. The dynamic data on the analog tape was digitized off line at a rate that was appropriate to replicate the analog

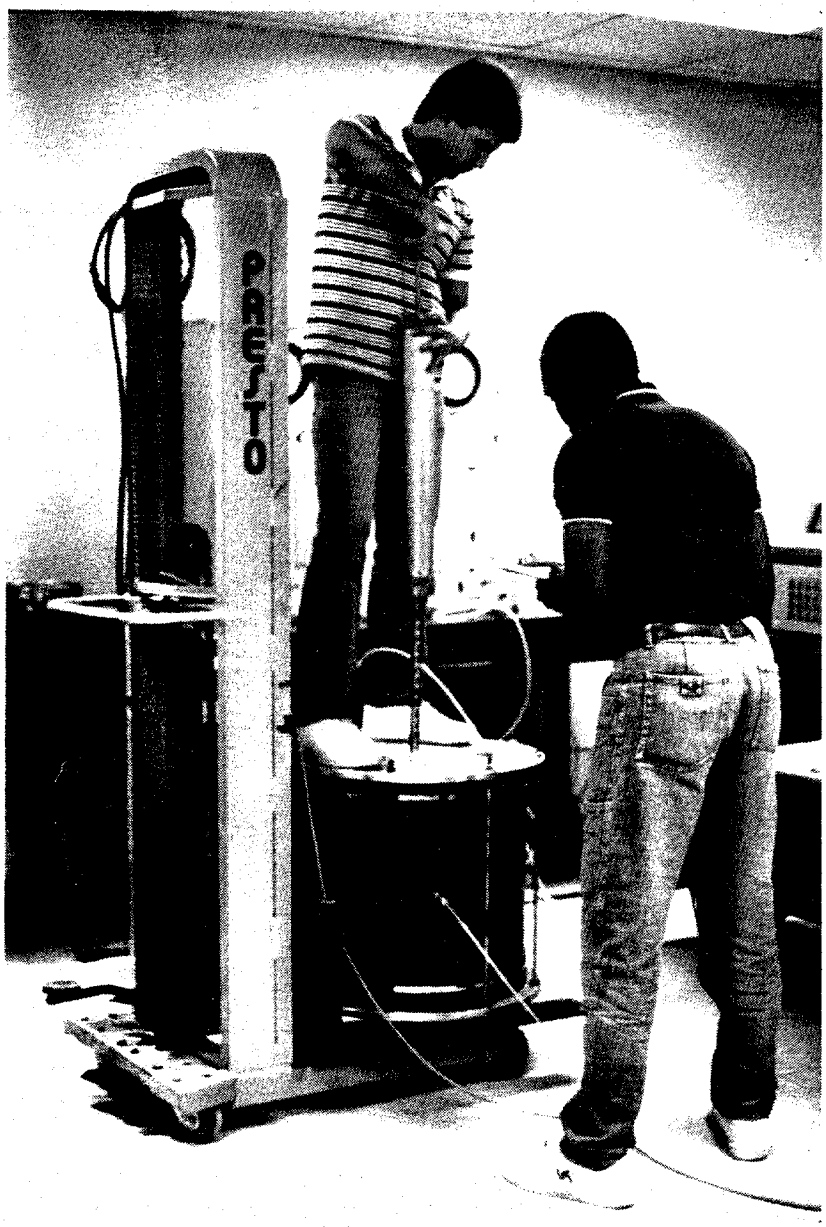

Fig. 3.9. Pile Installation Display

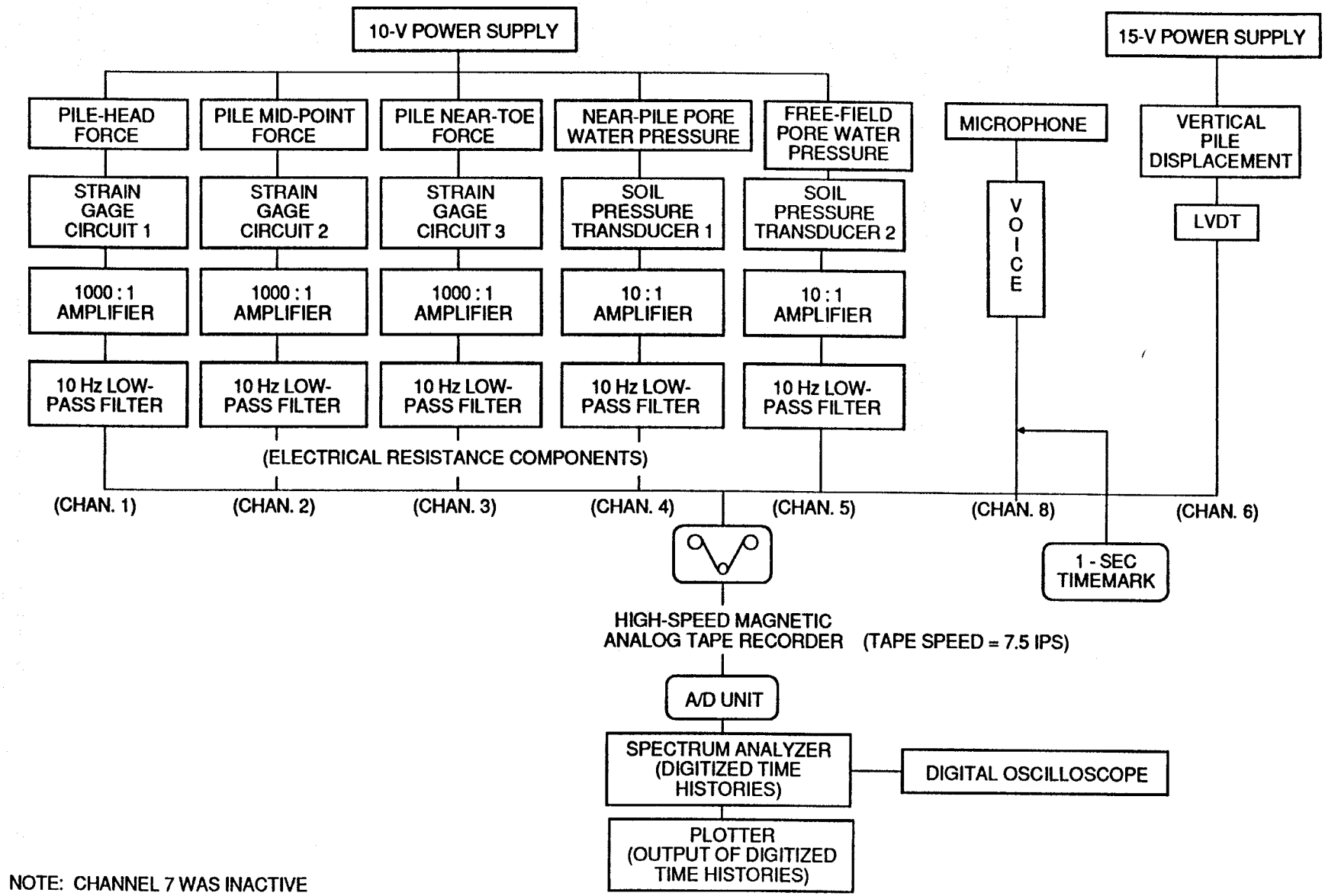

Fig. 3.10. Schematic of Dynamic Data Acquisition System

signals by an A/D converting unit that was coupled to the spectrum analyzer (Fig. 3.10). Digitized data were stored in the memory of the spectrum analyzer for further processing (simple multiplication by calibration factors) after which they were output to a pen plotter for interpretation. After every test, digitized data were reviewed for apparent correctness using the digital oscilloscope.

Filtering was employed to remove the effects of frequency components of any signals that are of no importance in the analysis of the tests. Low-pass filters employed during the data acquisition process used a 10-Hz rolloff for the circuits in the pile strain gages and pore water pressure transducers (in which predominant frequencies of the simulated earthquake were of the order of 1 to 4 Hz).

Although not explicitly shown in Fig. 3.10, each electrical resistance strain-gage-type circuit (pile strain gages and soil pressure cells) was connected to a shunting resistor to balance each circuit individually prior to each test. The strain gages were always zeroed with the test pile resting vertically on top of the chamber without the weight of the hammer resting on it. By this method it was possible to trace the true zero of the strain gages through the entire sequence of events during a test, even though data files were opened and closed many times (as they were on both the static and dynamic data acquisition systems), provided that the final reading before closing a file was taken under identical conditions as the opening reading of the next file. In this manner, residual stresses in the pile during driving could be included in the computation of the load-transfer curves.

Static Data Acquisition System

The data acquisition system that was used during the static load test and during the static parts of the dynamic tests (application of static bias load and static post-seismic test to failure) is shown in Fig. 3.11. Data from seven channels (plus the power supply) were acquired on command from the microcomputer, which was manually operated. Reading of data from all channels were made at intervals of applied pile-head load of 5 lbs, resulting in about 40 readings during the loading phase of a test. Keying the computer sent a command to the scanner to read each channel serially (requiring about 2.0 seconds). The digital voltmeter used with the scanner permitted acquisition of five digits of significant data. The digitized voltages were sent to a buffer from which they were read immediately by the microcomputer. Physically, all of the system shown within the dashed boundary in Fig. 3.11 was contained in one unit.

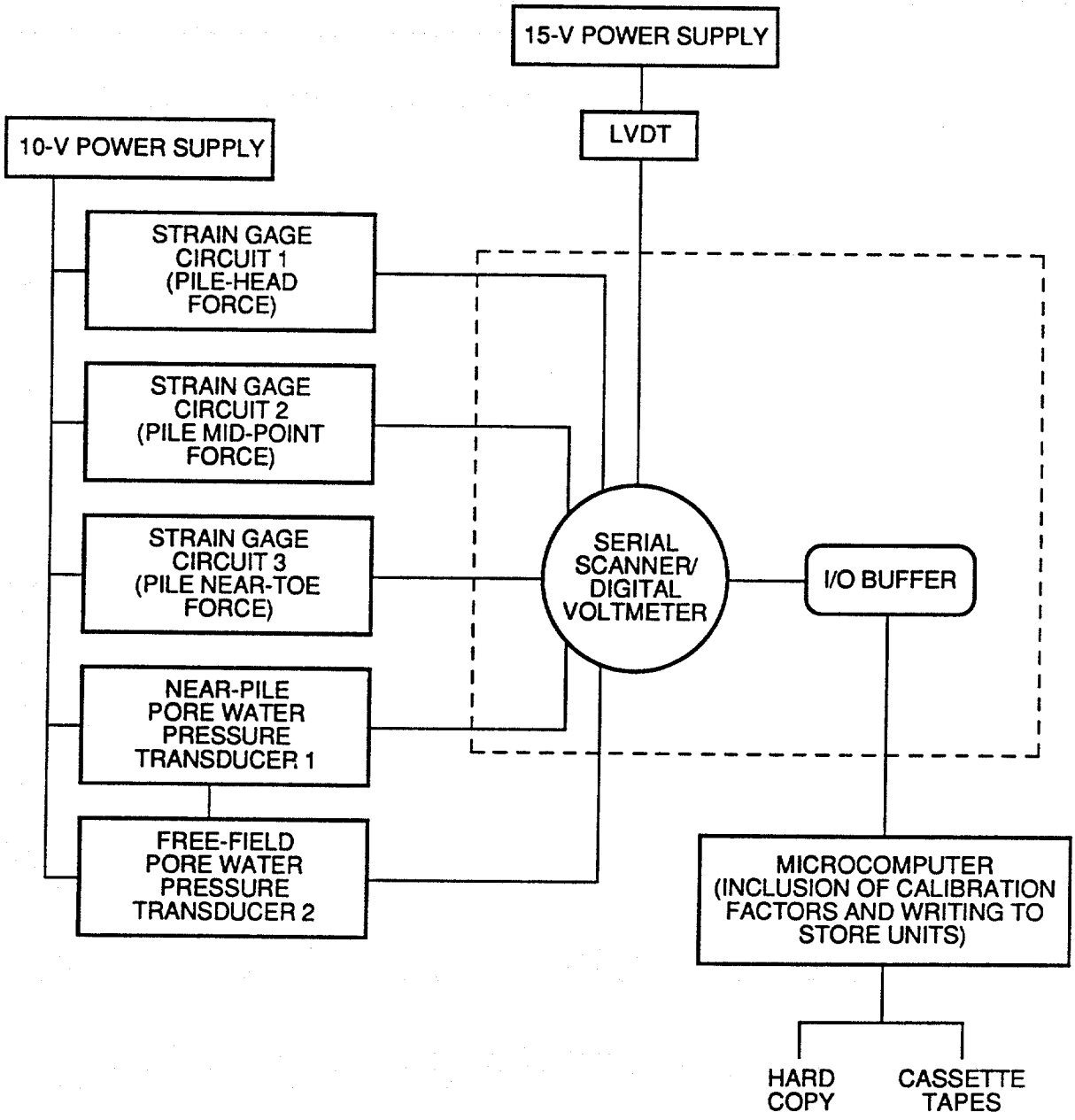

Fig. 3.11. Schematic of Static Data Acquisition System

The computer then performed simple mathematical operations (multiplying the voltage on each channel by the appropriate calibration factor) and wrote the resulting output (in engineering units) to both paper tape and a magnetic tape cassette. The hard copies (paper tapes) have been archived as permanent records of the static tests, and further used to develop load transfer curves and load-movement curves. As with the dynamic data acquisition system, the various strain gage circuits in the static system were balanced while the pile was stress free (sitting vertically on the top of the chamber). These zero conditions were used for the static load tests (i.e., no rebalancing was done once pile installation started), so that the stresses reported for static load tests contain the effects of any residual stresses that were induced in the pile during installation. Since a data file was also opened before each static event (i.e., initial static loading, post-seismic test static loading), all readings in such a file were subtracted from the first reading (datum) to obtain the true applied load at that particular moment, allowing the top strain gage readings to be used to compute the load-movement curves for the static pre- and post-seismic tests.

SAND PLACEMENT

It was judged that sand densities of practical interest for this study would be those in the medium dense to dense range (relative densities of approximately 55% to 85%), which are typical of offshore California deposits. The relative density of 55% in one of greatest practical interest since liquefaction problems are most likely to occur in looser soils. Experience indicated that the most appropriate means of preparing specimens of approximately 4 cubic feet in volume, with the relative densities between 55% and 85%, was to place them into the chamber by raining through air ("pluviate compaction").

A schematic diagram of the raining system used for deposition of the two sands employed in the study (fine SJR sand and micro-fine sand) in all density states is given in Fig. 3.12. Prior to the beginning of the sand raining process, a water diffusion ring and riser were placed at the bottom of the test chamber. The drop height was then adjusted depending upon the particular target relative density. Drop heights for each relative density were determined before the testing program started by placing aluminum sampling cans (standard laboratory moisture sample cans, two inches in diameter and 1.5 inches in height) inside the chamber and proceeding with the raining in 2-in. lifts from a known height. Each sample can was then carefully removed and the overburden properly trimmed. The weight of the dry soil within the sample can (which had a known volume) was measured,

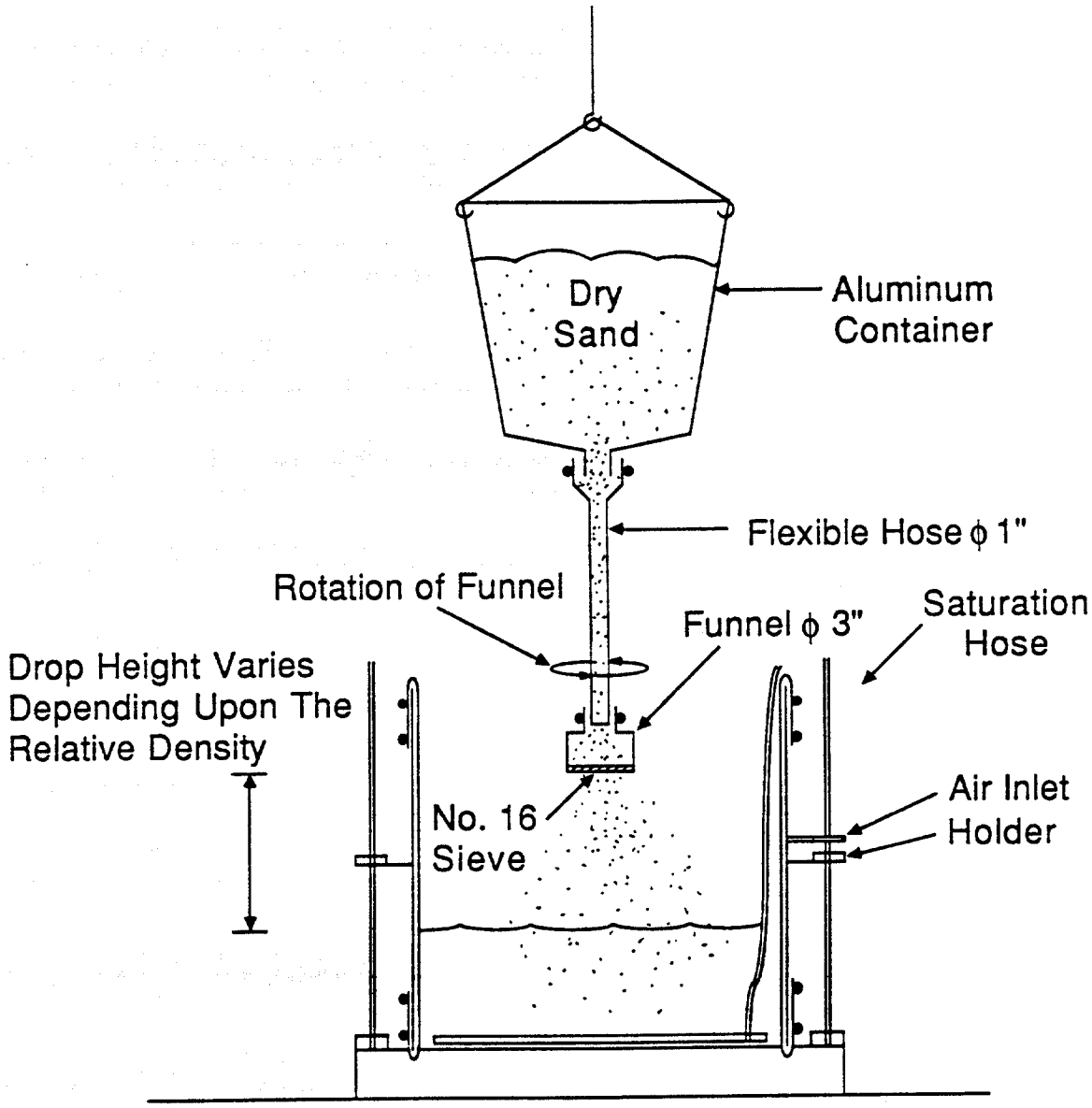

Fig. 3.12. Schematic of Sand Placement Arrangement

the dry unit weight calculated and the relative density determined based upon the known minimum and maximum index densities (Chapter IV). These procedure was repeated with different drop heights and for a given drop height until repeatability of the relative density for a particular drop height was achieved.

Once the drop height was properly set, the raining of the sand was done continuously, moving the funnel from the outside of the chamber to the inside in a circular pattern. Adjustments of drop height were made to keep it constant as the soil surface raised. The raining was then interrupted at the level of the soil instruments. Once the soil instruments were in place and the soil flushed with carbon dioxide and saturated with deaired water, the raining continued until the sand surface reached the top. The top membrane followed by the top plate were then placed and the bolts properly tightened. The remaining portion of dry sand (above soil instruments) was then saturated and equal confinement pressure applied to the membranes. On average, the time required to saturate the SJR sand was 1 hour, while for the micro-fine sand the saturation took about 36 hours.

Following the completion of a given test, the chamber was depressurized and the pile extracted. The top cap and top membrane were then removed, and the moist sand shovelled. Soil instruments were also carefully removed during this process. The moist sand was then placed in a forced-air conventional oven for drying. The oven-dry sand was then placed back into the stockpile bin for reuse in future tests. The drying process required about 24 hours and 48 hours for the 4 cubic feet of SJR sand and the micro-fine sand respectively.

CALIBRATION PROCEDURES

Pile Axial Strain Gages

The test pile was calibrated in tension to a load of 500 lbs prior to the beginning of the testing program. Fig. 3.13 shows the pile calibration arrangement. The calibration procedure was as follows: The pile was initially placed in a standard loading frame commonly used for triaxial tests in the laboratory. A calibrated load cell was then inserted between the pile head and a reaction beam to sense the applied load. A tension load was then applied by means of a hand-operated wheel engaged to a system of gears assembled in a particular configuration. Loading (tension) and unloading cycles to 100 lbs were repeated five times in order to exercise the pile and mitigate the effects of existing residual stresses in

Fig. 3.13. Test Pile Calibration Arrangement

the steel. The pile was then loaded in increments of 50 lbs and each strain gage along with the calibrated load cell and power supply were read using the static data acquisition system and bridge completion circuit that was used during the testing program. Graphical depictions of strain gage circuit output as a function of load for Gages 1 to 3 are given in Appendix B.

Miniature Pore Water Pressure Transducers (PDCR 81)

The calibration constants used during testing were provided by the manufacturer (Druck Inc.) and given in Appendix B. A check was performed by submerging the instruments in to a water tank to different levels of known hydrostatic pressure and sensing the voltage output response of each instrument using a voltmeter. Such a procedure verified that calibration constants given by the manufacturer were correct.

Test Chamber

The effective confining pressure applied to the soil mass through the 1/8-in-thick rubber membranes was checked. Two large calibrated electrical resistance pressure cells were embedded in the dry soil mass within the chamber, which was then pressurized through its membranes to a known value of pressure. Location and orientation of the sensing faces were different for both instruments to sense, approximately, the pressure distribution within the soil mass. It can be concluded from a table of known applied pressure versus the pressure response obtained from the pressure cells (Appendix B) that the "membrane effect" in the chamber membranes was negligible for the ranges of pressure considered in this study.

CHAPTER IV

Sand Properties

Laboratory tests were conducted to characterize the SJR sand and micro-fine sand. The tests performed were as follows: Grain-size distribution (sieve analysis), minimum and maximum index densities, permeability, triaxial compression, and interface shear. Although these tests do not necessarily represent the stress paths to which the sand was subjected in the test chamber during pile driving and static and dynamic testing, they provide information on the mechanical properties of the sands. In selecting effective pressures in the chamber, it was assumed that the soil stresses for penetrations up to 40 ft could be simulated within a reasonable approximation by applying an isotropic effective stress within the test chamber equal to the ground stress that could occur at the middepth of the pile if K_o in the soil deposit being simulated were 1.0. The in-situ isotropic effective stress levels of interests were in the range of 2.5 to 5 psi. Most of the pile tests were conducted with initial isotropic effective chamber pressure of 5 psi. However, the mean effective stress in the soil mass during and after installation would be expected to increase the level of mean effective stress around the pile considerably above the initial in-situ value. Therefore, laboratory strength tests were conducted with confining pressures of 10, 20 and 40 psi.

Grain-Size Distribution

Two types of sand were used in the study: a fine, uniform siliceous sand, or San Jacinto River (SJR), represented the prototype sand, and a mixture of a very fine sand ("Blasting Sand No. 5") and finely ground glass beads, termed "micro-fine sand," was used as the model sand in some tests. The grain-size distributions for the two test sands are shown in Fig. 4.1. For the SJR sand, the effective grain size, d_{10}, is 0.2 mm, and the coefficient of uniformity, C_u, is 1.74. From visual inspection the typical shape of the grains was observed to be subrounded, and the SJR sand can be classified according to the Unified Soil Classification System as "SP," or a poorly graded fine sand. For the micro-fine sand, the effective grain size, d_{10}, is 0.06 mm, the coefficient of uniformity, C_u, is 1.66, and can be classified as "SM," a very fine silty sand to sandy silt.

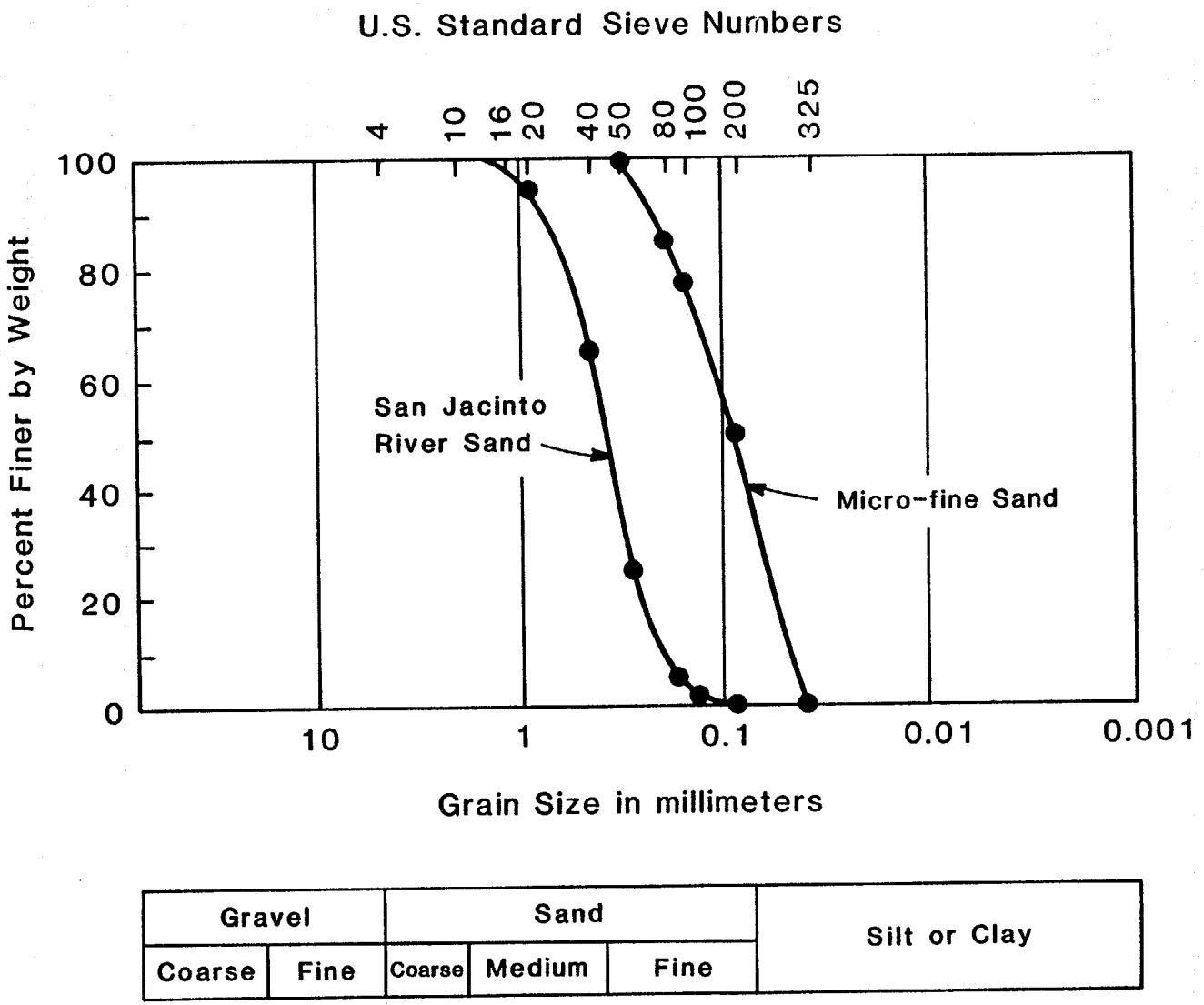

Fig. 4.1. Grain Size Distributions for Sands Selected for the Study

Minimum and Maximum Densities

Volume-change characteristics of the sand are considered to be one of the factors influencing the behavior of the pile-soil system under load. The volume-change characteristics are complex functions of the effective stresses and initial relative density of the sand. In order to control the actual density required for the attainment of target values of relative density, it was necessary to determine the minimum and maximum densities as defined by ASTM standards D 4253 and D 4254 (36). The values of the maximum and minimum index densities were 110.4 pcf and 94.2 pcf for the SJR sand and 112.9 pcf and 96.6 pcf for the micro-fine sand.

Permeability

Falling-head permeability tests were conducted on both sands deposited with a relative density of 55%. Tests were conducted by depositing oven-dry soil by raining through air into rigid wall cylinders, three inches in diameter and six inches in height, and saturating the samples very slowly with deaired water from bottom to top to simulate, approximately, the procedure that was used to deposit and saturate both sands in the test chamber. Coefficients of permeability for each sand are summarized in Table 4.1. It is observed that SJR sand (the coarser of the two test sands) is about 8 times more permeable than the micro-fine sand.

Table 4.1. Permeability Test Results

Sand	Coefficient of Permeability (cm/sec)
San Jacinto River	1.0×10^{-2}
Micro-fine Sand	1.21×10^{-3}

Triaxial Compression

Consolidated-drained triaxial compression tests were done on saturated samples of medium dense (60% nominal relative density) SJR sand, which was the relative density employed in most chamber tests. These tests were conducted to provide information of stress-strain properties and shear strength, as characterized by the angle of internal friction. The samples were prepared by raining of oven-dry sand, as per the permeability test. After gravity saturation (and verification of saturation by measurement of the B-parameter), the 1.5-in-diameter by 3.0-in-high specimens were consolidated isotropically and then loaded to failure by increasing the major (vertical) principal stress at a constant displacement rate of 0.23 mm/minute. During the application of load, volume change was measured by recording the amount of water that flowed into or out of the specimen from a calibrated burette that communicated with the pores of the specimens. The stress-strain and volume-strain response are shown in Fig. 4.2. Volumetric changes are expressed as volumetric strain (change in volume / initial volume, as a percent). The results for the medium dense conditions (relative density of 60%) indicate that SJR sand contracts initially upon shearing, with the magnitude of contraction depending on the value of the confining pressure, and then dilates after shear failure begins.

A plot of mean effective normal stress versus maximum shear stress ("p'-q diagram") is shown in Fig. 4.3. The angle of internal friction, ϕ, can be derived from the slope of this relation as

$$\phi = \sin^{-1} [\tan \xi] \qquad (4.1)$$

where ξ is the slope of the line in Fig. 4.3. The measured value of the angle of internal friction, ϕ, is about 39°.

Interface Shear

It was also considered important to investigate the interface shear strength properties of both sands and the material comprising the outer wall of the pile. In order to study this effect, interface shear tests were conducted in a direct shear apparatus. Sand was deposited by raining the soil in a dry state at an approximate relative density of 60% onto a prepared flat steel plate in the bottom half of a circular direct shear box, 3 in. in diameter. In order to represent the pile surface closely, the steel plate was made of the same material as the pile

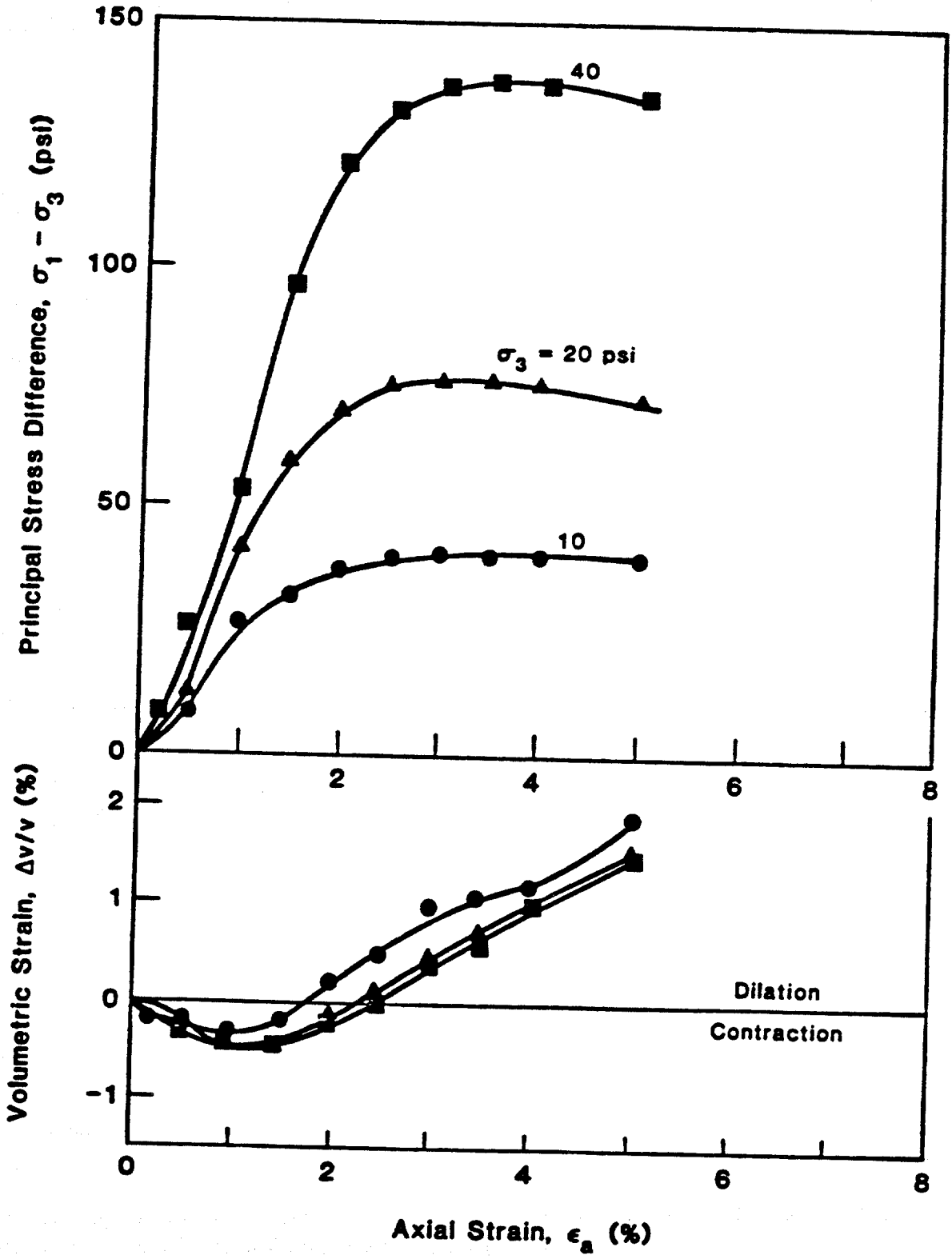

Fig. 4.2. Results of Consolidated-Drained Triaxial Compression Tests for SJR Sand at 60% Relative Density

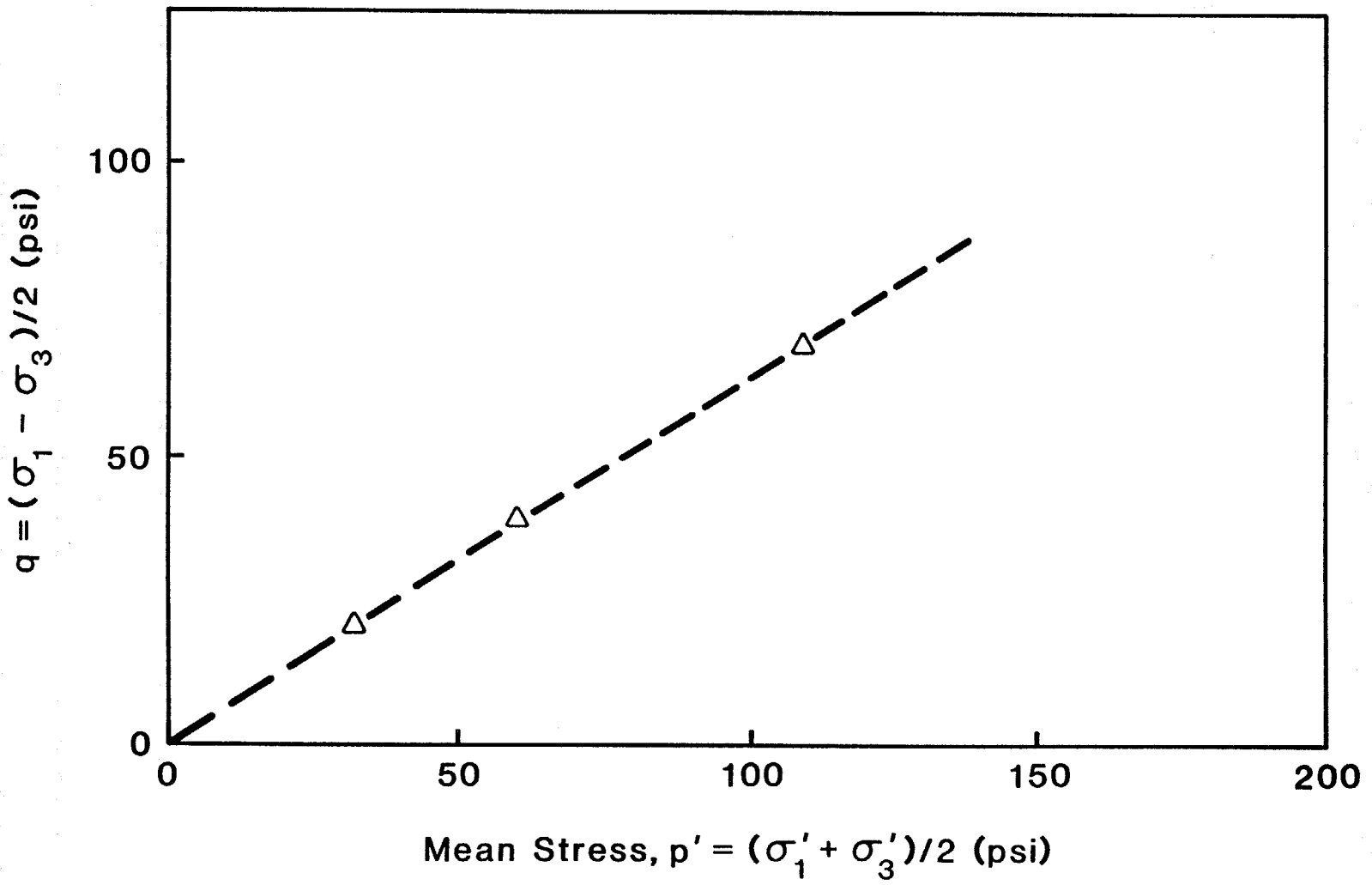

Fig. 4.3. Failure Envelope for Triaxial Compression Test on p'-q Diagram on SJR Sand

and was given the same finish as that on the pile by lightly machining it with an end mill and rubbing it with an emery cloth prior to depositing the sand. After placement, the sand was saturated and tested in a consolidated-drained mode under normal interface stresses of 10, 30 and 50 psi for SJR sand, and 11, 22 and 45 psi for micro-fine sand. Both shear stress-displacement and vertical-horizontal-displacement relations are given in Figs. 4.4 and 4.6 The contractive behavior of both sands placed at 60% relative density can be observed for different normal pressures.

The interface frictional failure envelope are shown in Figs. 4.5 and 4.7. The interface friction angle were 27° and 20° for SJR sand and micro-fine sand, respectively. It is noted that the interface friction angle of the SJR sand is considerably lower than the angle of internal friction obtained from triaxial compression tests for peak principal stress differences.

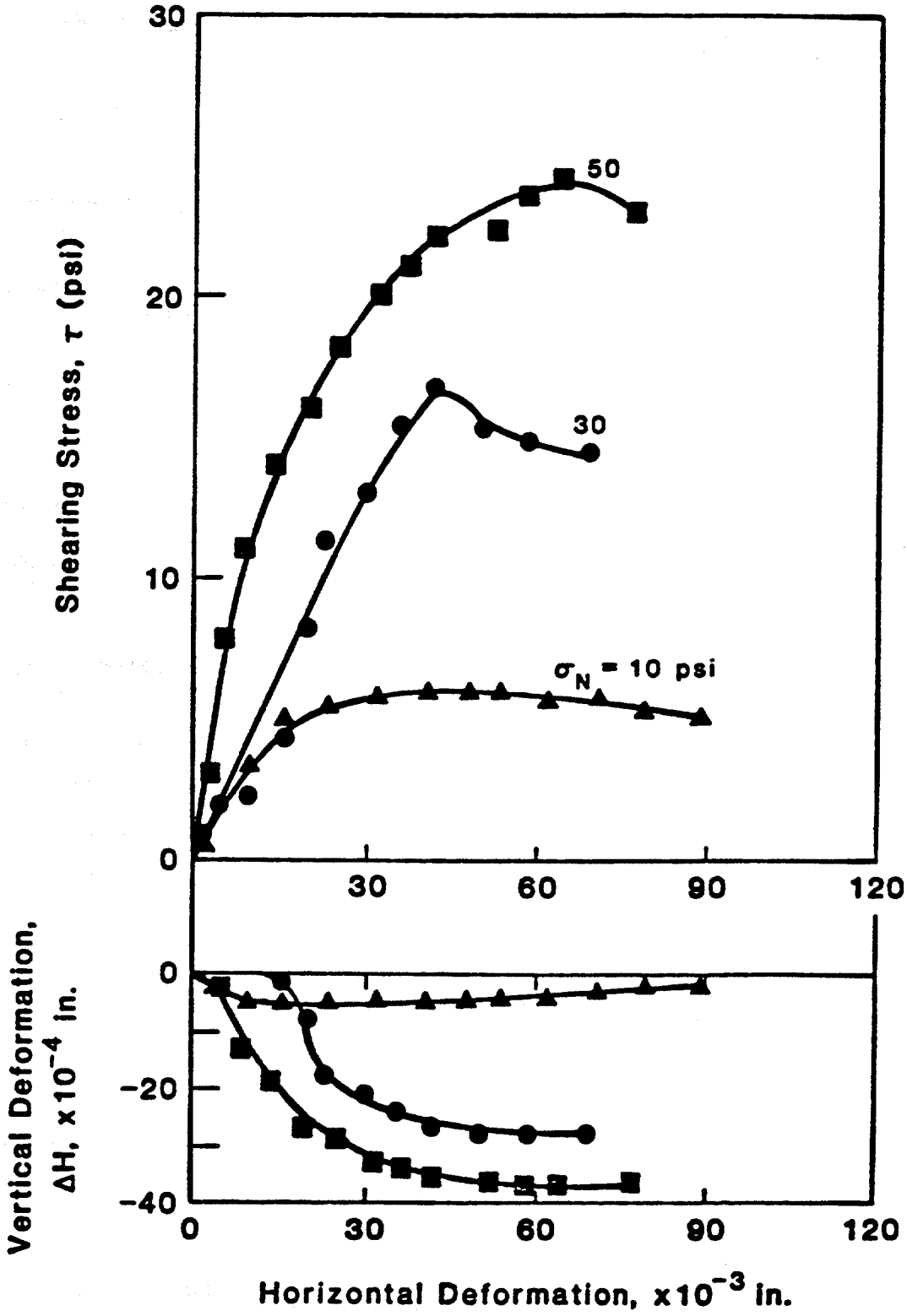

Fig. 4.4. Results of Direct Interface Shear Tests for SJR Sand at 60% Relative Density

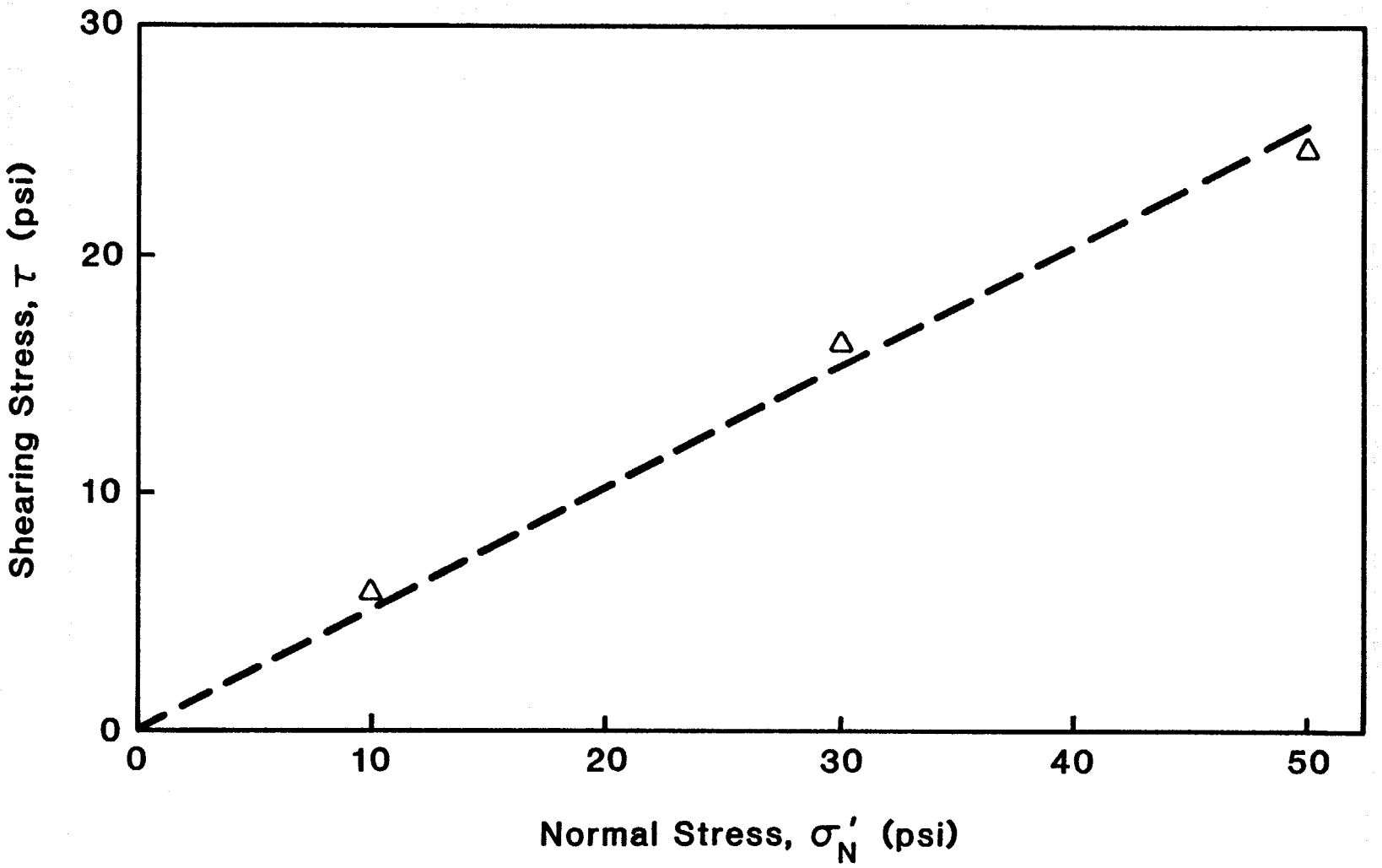

Fig. 4.5. Failure Envelope for the Direct Interface Shear Test on SJR Sand

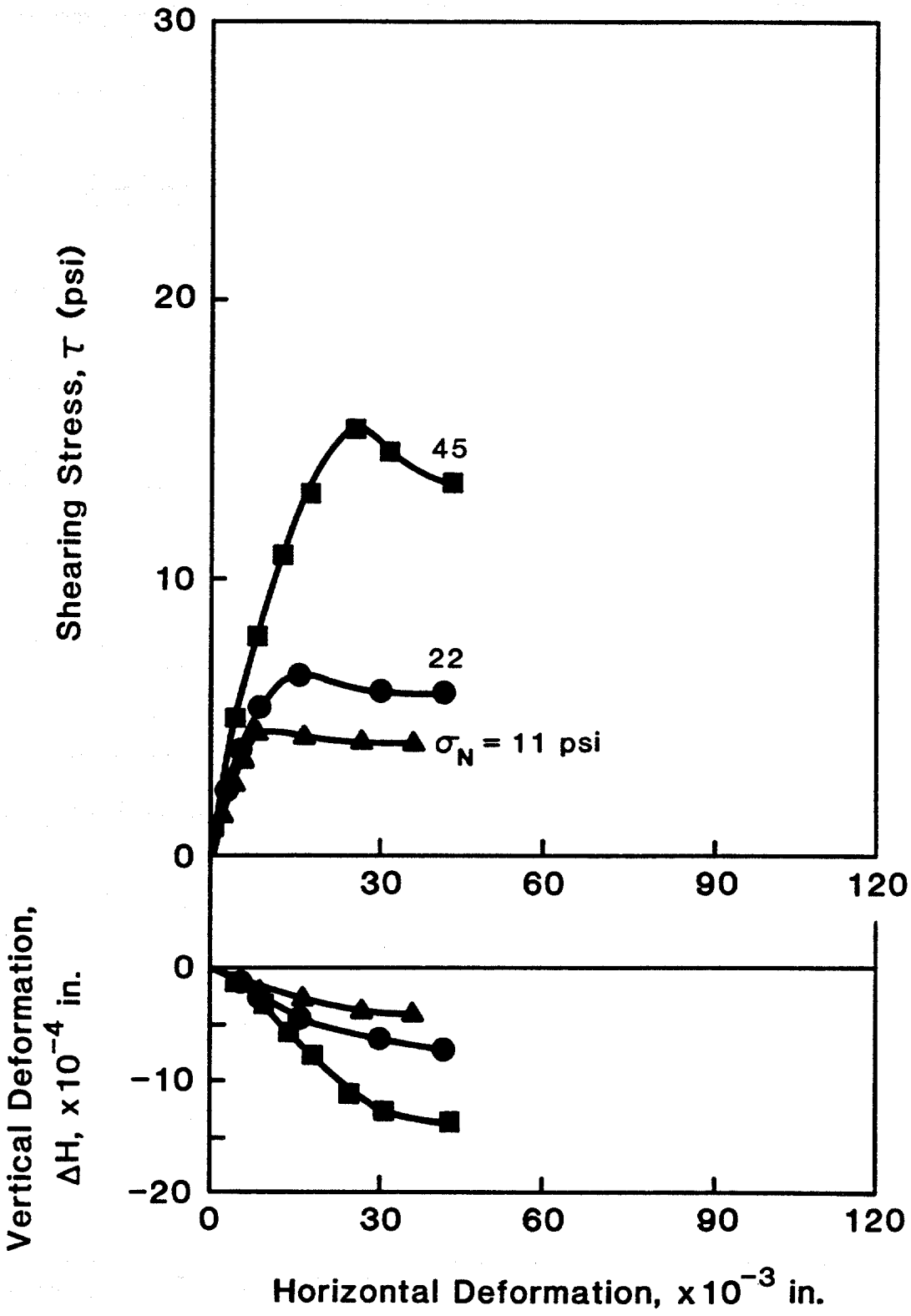

Fig. 4.6. Results of Direct Interface Shear Tests for Micro-fine Sand at 60% Relative Density

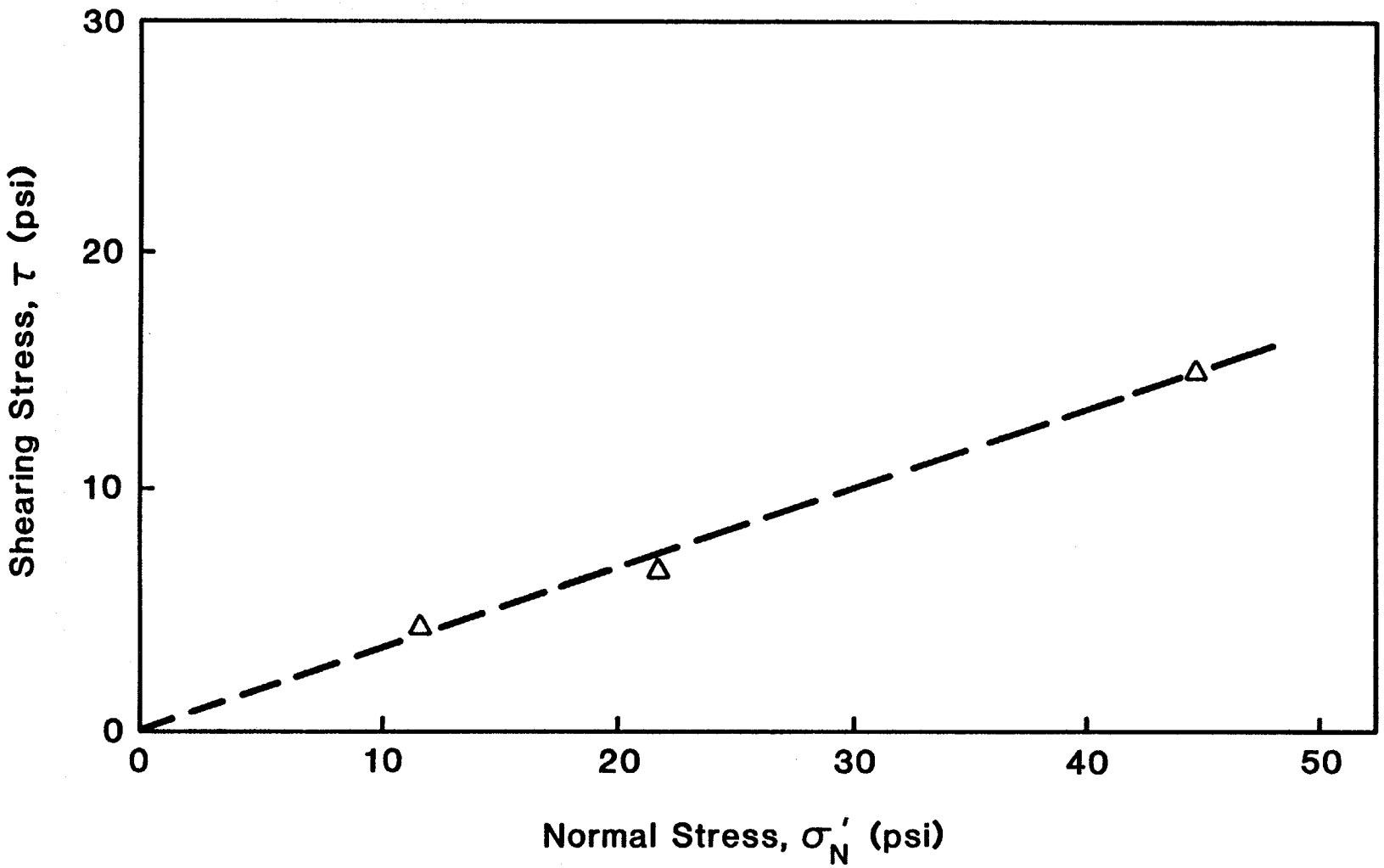

Fig. 4.7. Failure Envelope for the Direct Interface Shear Test on Micro-fine Sand

CHAPTER V

Scaling Procedures

The site that was chosen for simulation was the SEMS (Seafloor Earthquake Measurement System) site off Long Beach, California, a deep soil site at which strong-motion seismic records were recorded in three dimensions during two seismic events in 1986 (37). The particular event chosen for this study was the Oceanside event of July 13, 1986, a Magnitude 5.8 earthquake whose epicenter was 74 km southeast of the instrumentation site. Epicentral distance, time of first motion, depth of focus, location of the instrumentation site and orientation of the horizontal (X and Y) accelerometers are shown in Fig. 5.1.

The recorded vertical, or Z, component of motion is shown in Fig. 5.2. Peak vertical accelerations were of the order of only 3 - 4 milli-g's, and the strong shaking duration was 80 seconds. Experience and intuition suggested that tension pile response to such an event would not produce any measurable loss of capacity. Therefore, a scaling procedure was used to scale upward the Z component from a Magnitude 5.8 to a Magnitude 8.0 which was perceived to be an upper limit to any seismic event that could occur along faults within 74 km of the recording site. The following section describes the procedure for first-level scaling the earthquake.

Earthquake Scaling

Simple scaling of earthquakes can be performed either in the time domain or in the frequency domain. In the time domain, the time axis and/or the acceleration axis of the seismic record are multiplied by respective ratios (scaling factors) computed by comparing the significant characteristics (maximum acceleration amplitude, predominant frequency, and duration of strong motion) of existing and desired earthquake records. An example of this is the simplified procedure proposed by Seed and Idriss (38) for scaling rock motions. When using this approach, care must be exercised to avoid possible physical instabilities. In the frequency domain approach (chosen for this study), the scaling procedure involves transforming the time history into the frequency domain, scaling to a spectrum that would

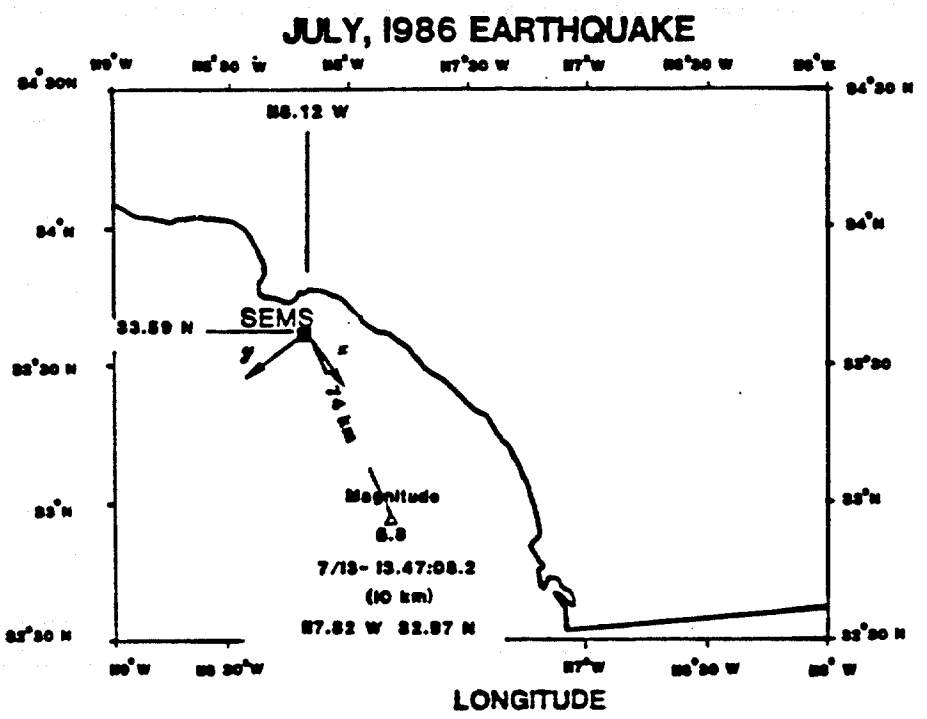

Fig. 5.1. Location of SEMS Unit (After (37))

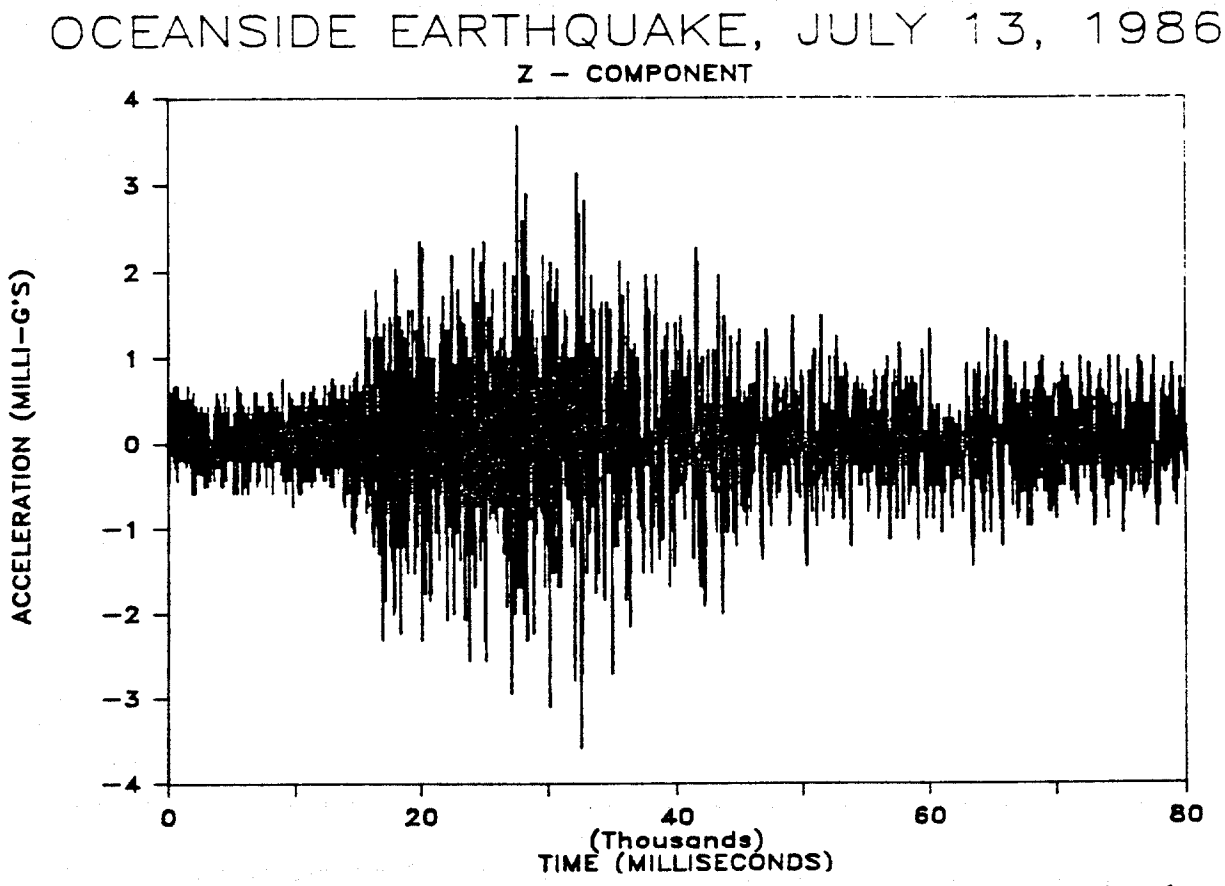

Fig. 5.2. Seismic Record of Vertical, or Z, Component of Oceanside Earthquake

represent a higher magnitude event (for instance, Magnitude 8.0), termed the target spectrum, and deconvolving back into the time domain while maintaining the same phase relationship that existed in the original unscaled record.

A step-by-step description of the frequency-domain scaling procedure for the Z-component of the Oceanside earthquake follows. First, the frequency content of the acceleration versus time record of the z-component of the earthquake in Fig. 5.2 is computed using the algorithm named the 'Fast Fourier Transform' (FFT), developed by Cooley and Tukey (39). This algorithm makes the involved computations feasible for its use in microcomputers. The frequency content of the Z-component is given in Fig. 5.3. After analyzing its frequency content and considering the low acceleration values of the original record, it was judged necessary to filter some of the undesirable high frequencies, the result of recording instrumentation noise. In order to do so, a recursive type of low-pass digital filter (40) was used, which is characterized by the following equation:

$$Y_n = (1 - A)\, X_n + Y_{n-1} \ , \qquad (5.1)$$

where

Y = Filtered value of acceleration,
X = Original, unfiltered value of acceleration,
A = Parameter indicating the degree of filtering (A = 0 corresponds to no filtering, A = 1 corresponds to maximum filtering), and
n = Time step designator.

The original record was filtered using a value for A (selected by initial inspection of the frequency spectrum) of 0.7, which resulted in unfiltered predominant frequency content between 1 and 4 Hz, a characteristic range for strong seismic events at deep soil sites. The frequency content of the filtered signal is given in Fig. 5.4. For completeness, Fig. 5.5 displays the phase angles of the filtered but unscaled seismic record.

The second step is to establish an appropriate 'target' spectrum. In the development of scaling accelerograms for use in earthquake-resistant design, it is common practice to utilize some type of standard response spectrum shape, often scaled by an engineering estimate of the appropriate peak acceleration. Response spectra represent the maximum response (in acceleration, velocity and displacement) as a function of frequency, for a given damping, of a single-degree-of-freedom system subjected to a time-dependent

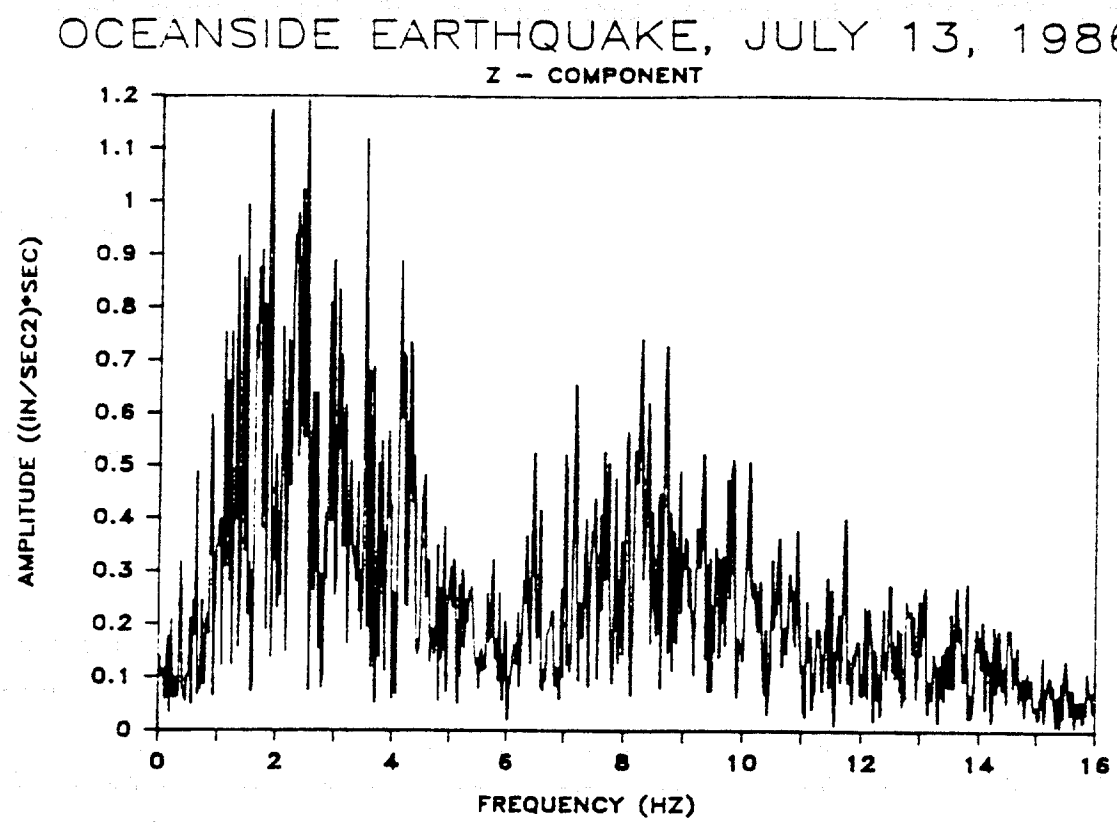

Fig. 5.3. Frequency Spectrum of Unfiltered Z-Component Record

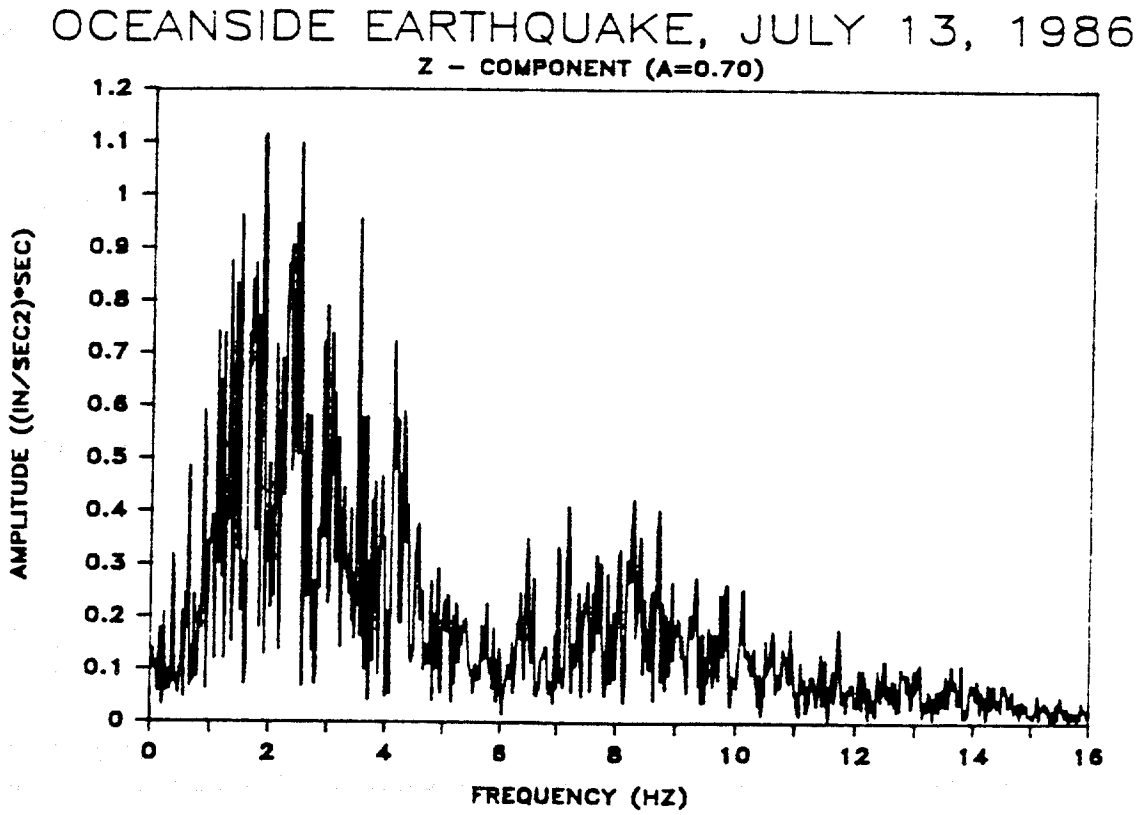

Fig. 5.4. Frequency Spectrum of Filtered (A = 0.7) Z-Component Record

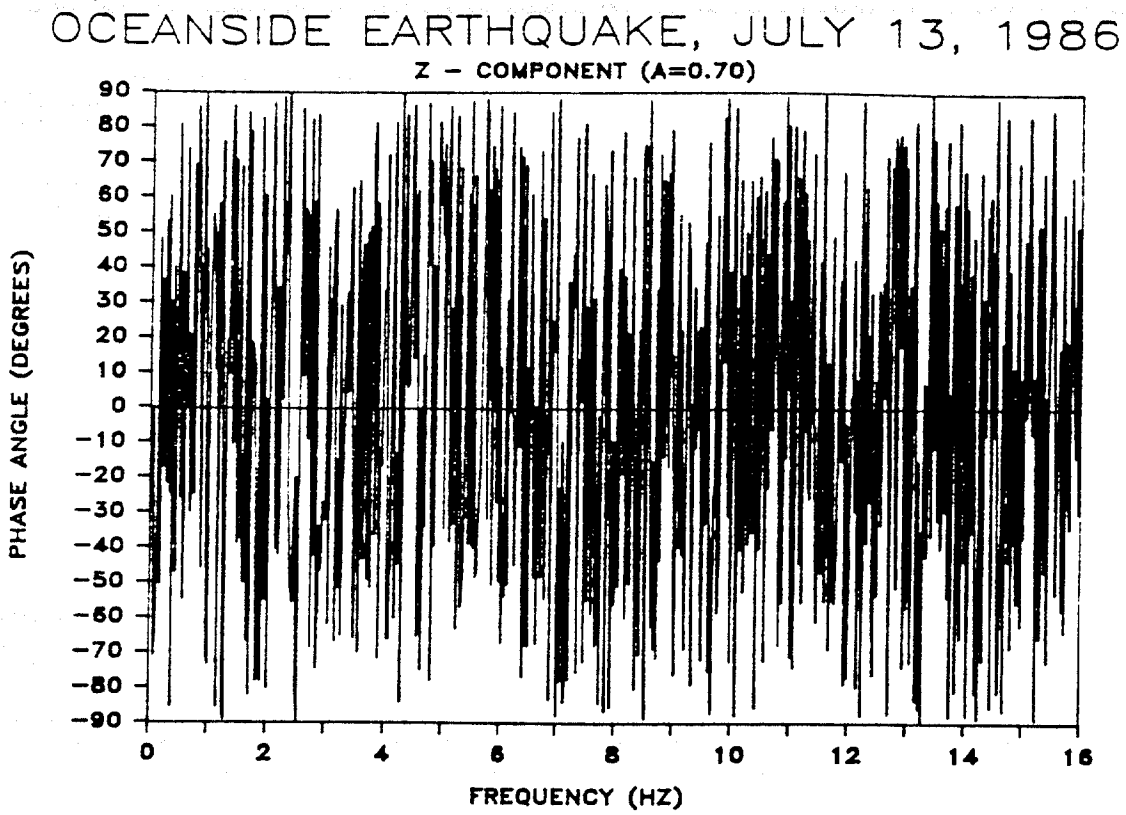

Fig. 5.5. Phase Angles of Filtered Z-component Record

excitation. This approach can be rationalized for those applications where engineering judgment is most conveniently anchored to the methodology of the response spectrum approach. From a physical point of view, however, when it is required to estimate actual strong motion accelerations for given or assumed characteristics (parameters) describing the strong shaking, the approach based on scaling accelerograms in terms of Fourier amplitude spectra is more direct and better defined. Fourier amplitude spectra directly defining spectral parameters as functions of the Modified Mercalli Intensity (MMI), distance from epicenter, period (T), soil conditions, and direction of components (vertical and horizontal) of the strong motion have been derived by Trifunac (41). The data base for Trifunac's analysis resulted from recording 57 earthquakes with Magnitudes between 3.0 and 7.7, and consisted of 186 records. Trifunac's proposed model is as follows:

$$\mathrm{Log}_{10}[FS(T),p] = a(T)p + b(T)I_{MM} + c(T) + d(T)s + e(T)v\ , \qquad (5.2)$$

where

$FS(T),_p$ = Estimate of the Fourier spectrum amplitude at the period of vibration, T, which is larger than the p fraction (confidence level) of all the data so far recorded under the same conditions,

a(T), ..., e(T) = Regression coefficients (given in Fig. 5.6.),

I_{MM} = Level of intensity at a given site in terms of the Modified Mercalli Intensity,

s = Approximate site soil conditions (s = 0 for alluvial soil sites, s = 2 for rock sites, and s = 1 for intermediate sites), and

v = 0 for horizontal (X,Y) components and 1 for vertical (Z) component.

Vertical motion Fourier amplitude spectra computed from Eq. 5.2 for p = 0.50 and different levels of MMI are shown in Fig. 5.7.

Based on the same 186 earthquake records, Trifunac (Ref) performed an analysis of the rate of decay of MMI with epicentral distance and correlated this decay with earthquake magnitude. Such correlations are depicted in Fig. 5.8. For this study, for an epicentral distance of 74 km and a Magnitude 8.0 earthquake the corresponding value of MMI is, approximately, 8.5. Interpolated values of the Fourier amplitude spectrum for MMI of 8.5

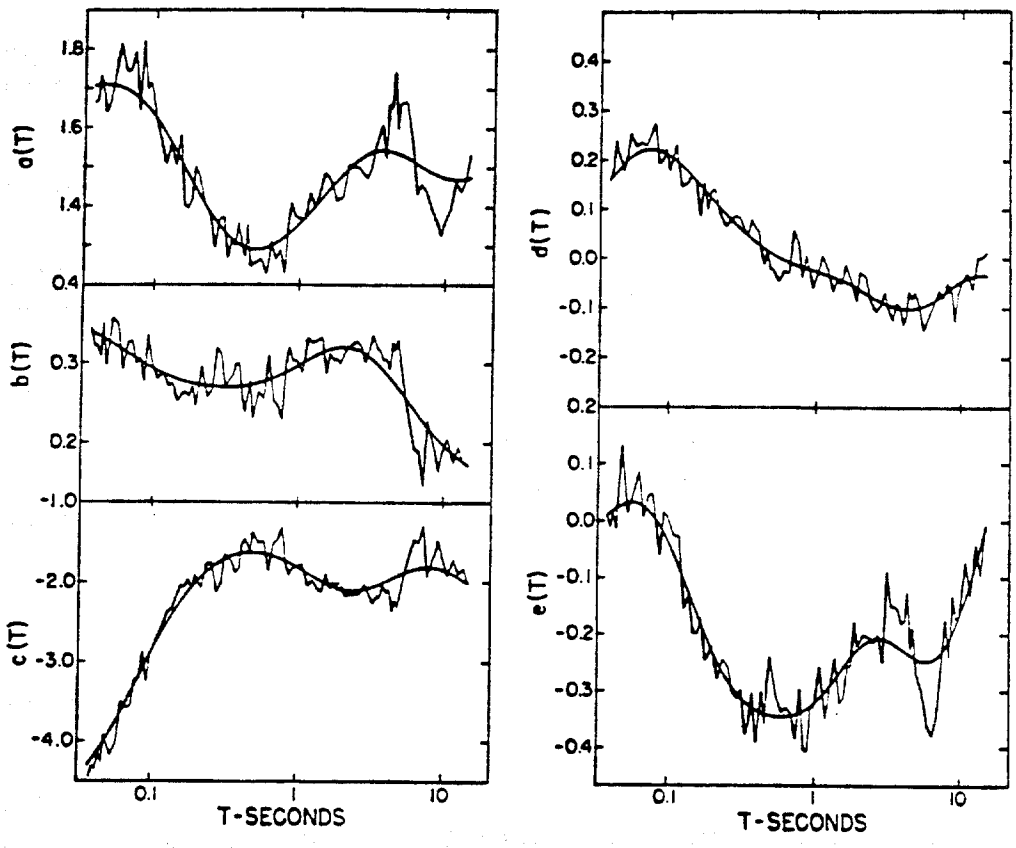

Fig. 5.6. Functions a(T), b(T), c(T), d(T), and e(T) for use in Eq. 5.2 (After (41))

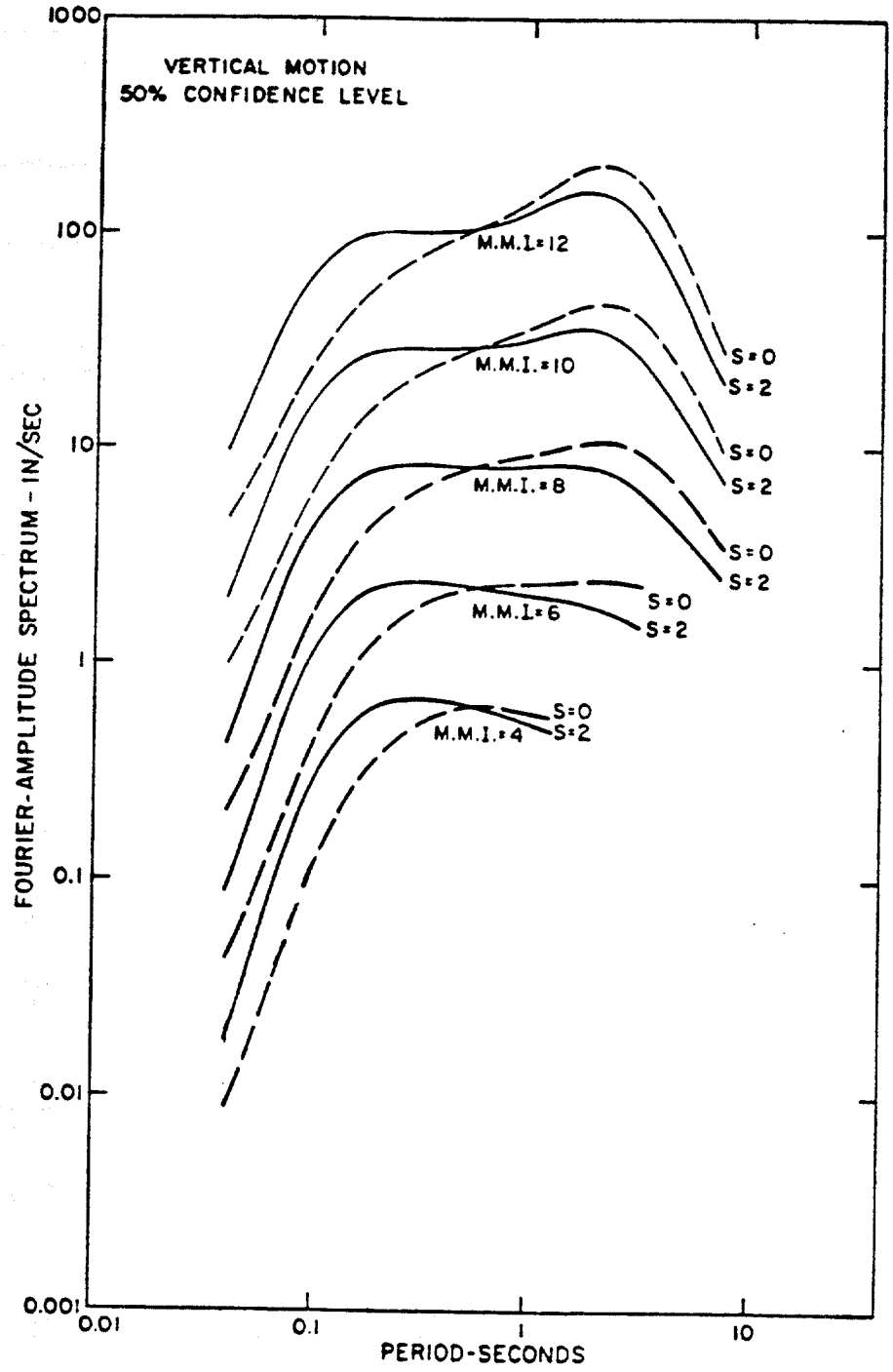

Fig. 5.7. Vertical (v = 1) Fourier Amplitude Spectra for MMI = IV-XII, for s = 0 and s = 2, and for p = 0.50 (After (41))

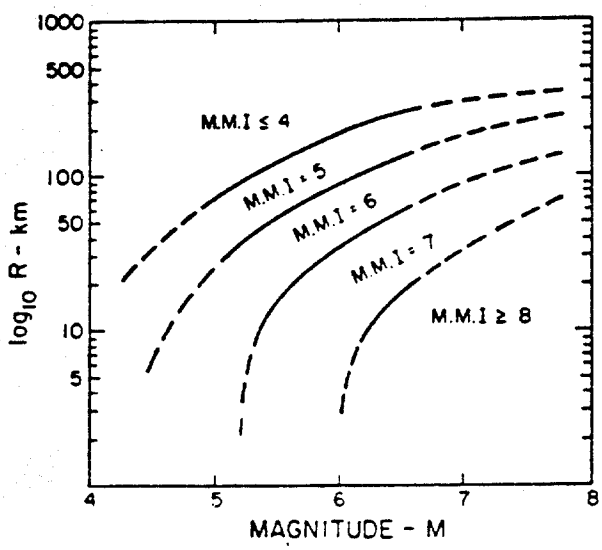

Fig. 5.8. Rate of Decay of MMI with Distance, R, and Magnitude, M (After (41))

can be obtained from Fig. 5.7, for later use in scaling. S = 0 for sites such as the SEMS site.

The third step in the scaling procedure consisted of scaling upward the spectrum of the original seismic record to match the target spectrum. This can be accomplished by multiplying the real and imaginary parts of the Fourier amplitude spectrum, at a particular frequency, by the same constant (phase relationship is not altered) to match the target spectrum. The value of the multiplying constant changes from frequency to frequency. It was judged that frequencies lower than 0.1 Hz and higher than 10 Hz would not be scaled up since their contribution to the strong motion is minimum. The original spectrum (after being filtered), the target spectrum (from Fig. 5.7, for MMI = 8.5), and the computed spectrum after scaling are shown in Fig. 5.9.

The fourth, and last, step is to deconvolve the computed (scaled) spectrum back into the time domain while maintaining the same phase relationships (angles) that existed in the unscaled filtered record. For that purpose, the Inverse Fast Fourier Transform (39) was implemented to generate the time history of the new scaled accelerogram (Fig. 5.10) which was used in the testing program (peak accelerations of the order of 70 milli-g's). As shown in Fig. 5.11 the displacement versus time record of the new scaled accelerogram was also obtained by double integration of the acceleration time history.

Comparisons of peak accelerations (horizontal and vertical components) of the Oceanside earthquake (scaled to a Magnitude 8.0) and the recent October 17, 1989 Loma Prieta earthquake (Magnitude 7.1), formelly named Santa Cruz Mountain earthquake, are given in Table 5.1 (42). Locations of the recording sites: Foster city, Hayward-Muir School and the San Francisco International Airport with respect to the causative fault are shown in Fig. 5.12. The average distance to the approximate center of the aftershock zone is about 78 km. No soil profiles are available at this time.

Differences in the observed and scaled magnitudes might possibly be attributed to the scaling procedure based on Trifunac's attenuation curves, which, in turn, are based on the Modified Mercalli Intensity (which is not a precise engineering measure of severity of ground shaking), and the use of the 50% confidence level in the computation of the target (Fourier amplitude) spectrum. However, the Loma Prieta event appeared to be unusual in that it produced high accelerations but with relatively few cycles of strong motion for an event of such magnitude. Assuming the peak acceleration values of the October 1989 Loma

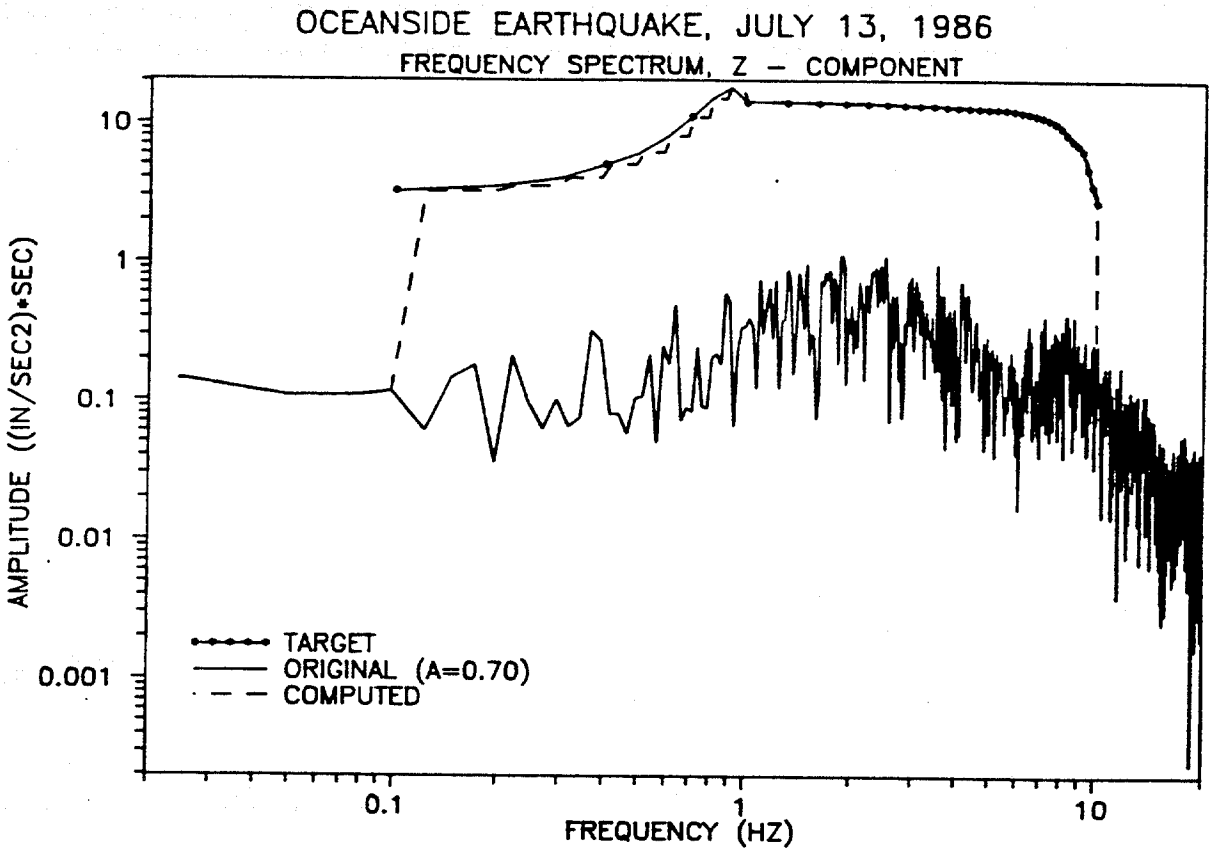

Fig. 5.9. Original (Filtered A = 0.7), Target and Computed (Scaled) Spectra

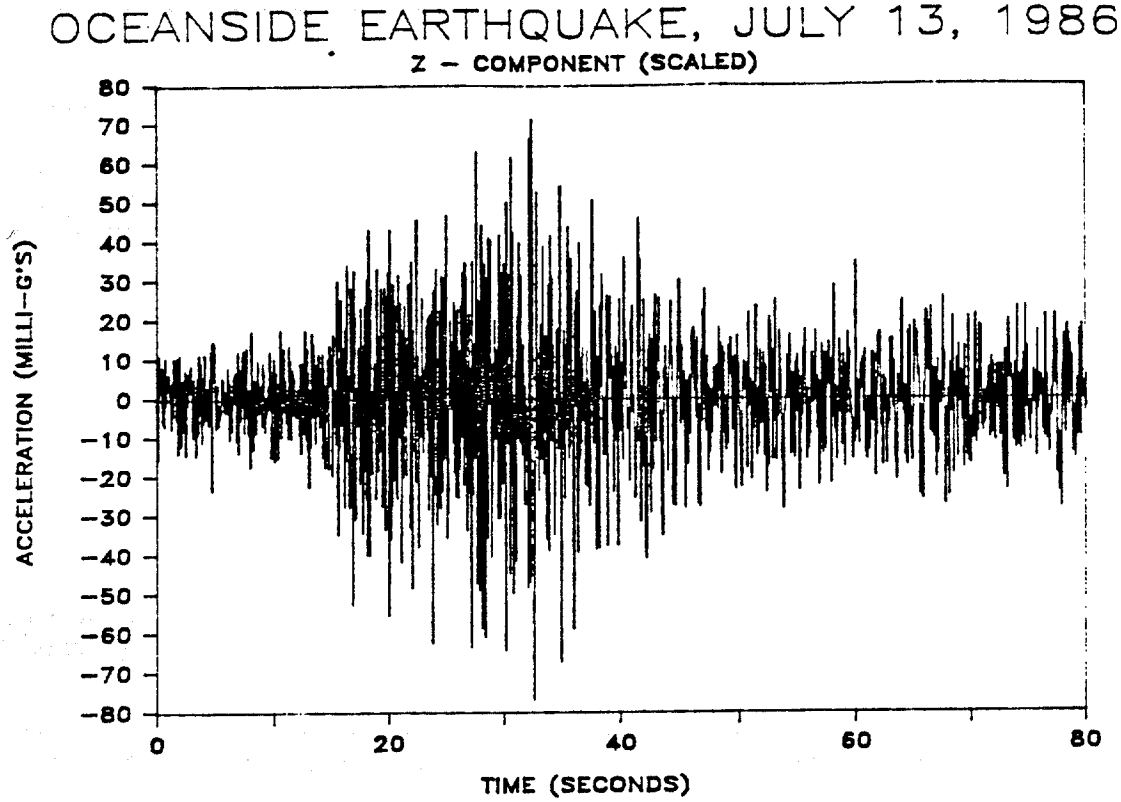

Fig. 5.10. Scaled Vertical, or Z, Component of Oceanside Earthquake

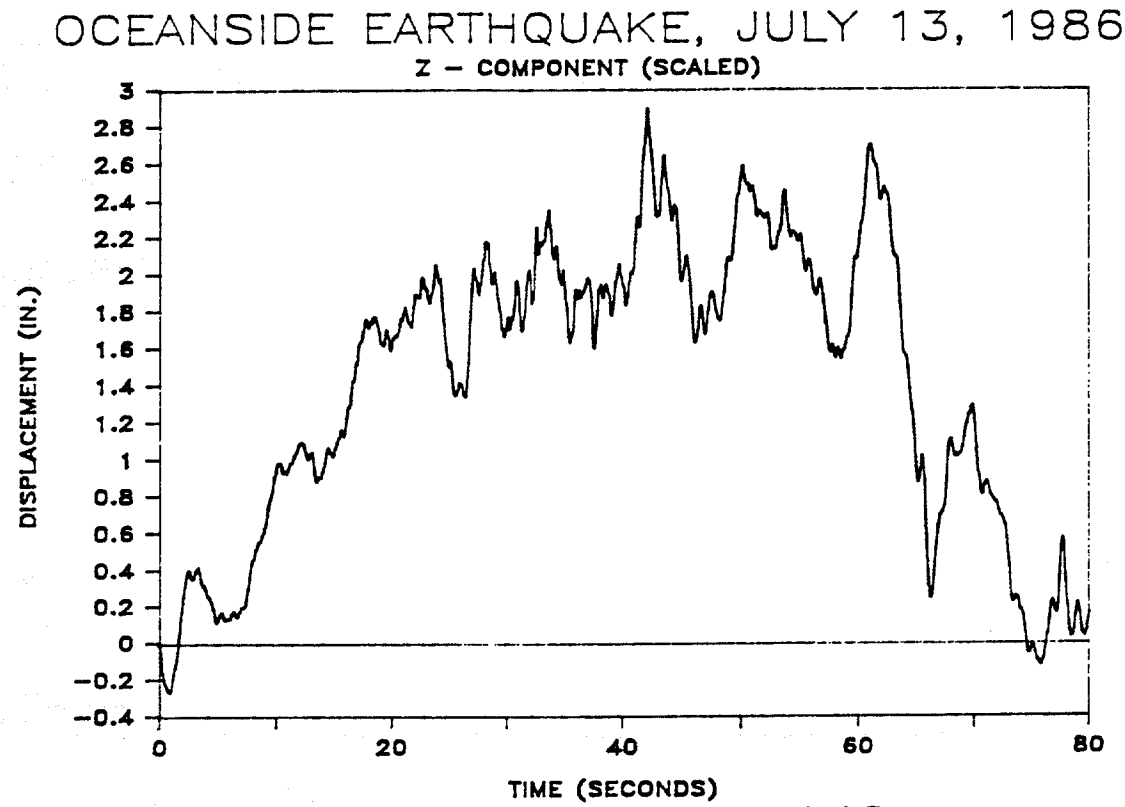

Fig. 5.11. Displacement Time History of Scaled Vertical Component of Oceanside Earthquake

Table 5.1. Comparisons Between Recent Loma Prieta Earthquake and Scaled Oceanside Earthquake.

Loma Prieta Earthquake (Magnitude 7.1), October 17, 1989 (42)

Recording Site Location	Approximate Epicentral Distance (km)	Horizontal Component 0°	Horizontal Component 90°	Vertical Component
Foster City	70	0.26g	0.29g	0.11g
Hayward-Muir School	77	0.18g	0.14g	0.10g
San Francisco International Airport	87	0.24g	0.33g	0.05g
Average:	78	0.24g		0.086g
Oceanside Earthquake (Scaled to a Magnitude 8.0)	74	0.25g		0.079g

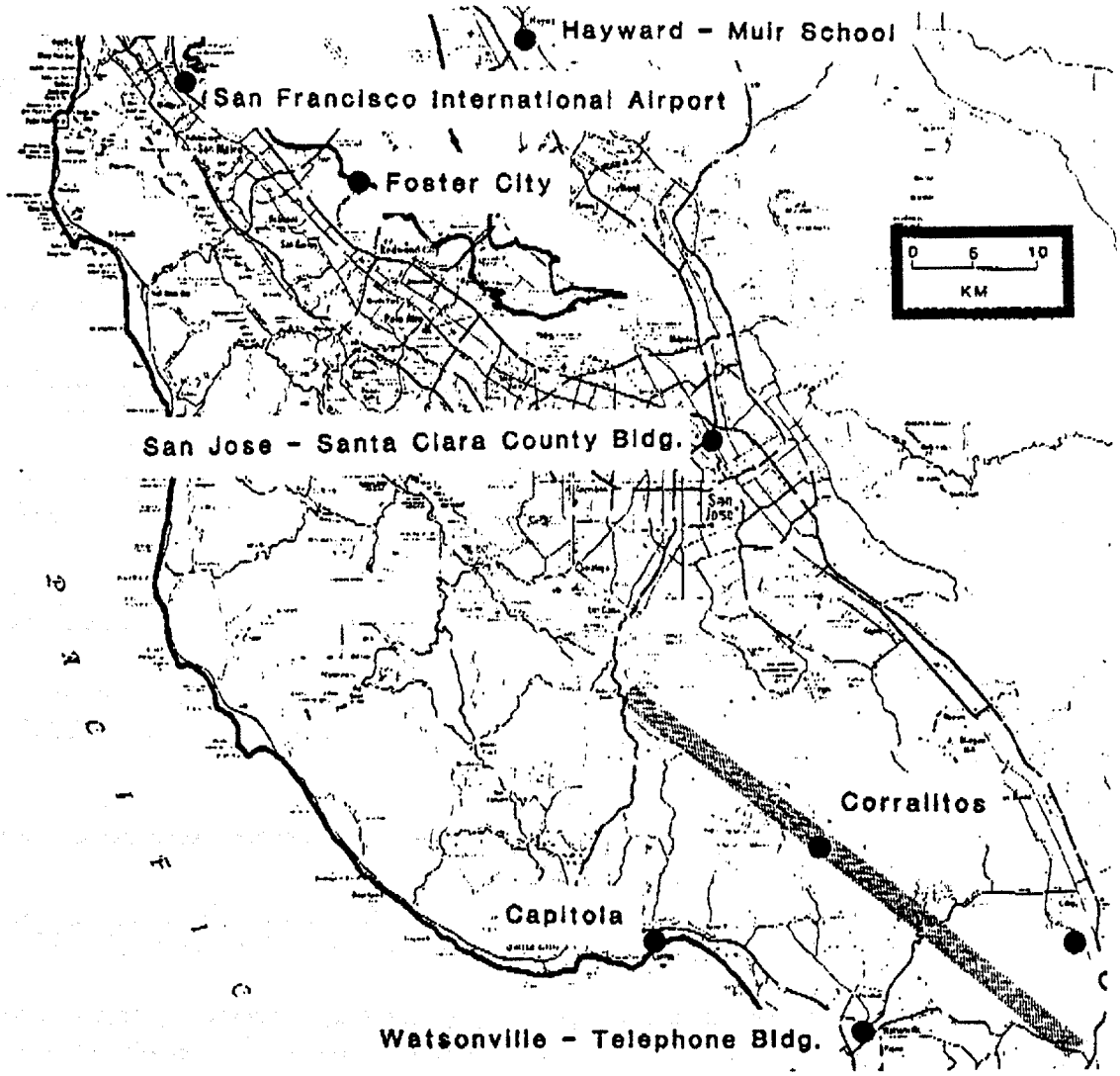

Fig. 5.12. Recording Site Locations During October 17, 1989 Loma Prieta Earthquake (After (42))

Prieta event were typical of a Magnitude 7.1 earthquake, then the scaled values of acceleration of the 1986 Oceanside earthquake rather represent, approximately, a Magnitude 7.0 instead of a Magnitude 8.0. A Magnitude 7.0 earthquake is commonly used for designing of oil-production platforms, offshore central and southern California.

Model to Prototype Similitude

Seismic testing on centrifuged models, pioneered by Schofield at Cambridge University, has been suscesfully applied to model dynamic soil-structure interaction problems. In the centrifuge, the same unit stress that exists in full-scale structure can be reproduced at corresponding points in a small-scale model by creating an artificial gravity field, Ng, where g is the acceleration due to earth's gravity and 1/N is the linear scale of the model. The ability to create prototype stresses in the model is extremely important in soil-structure interaction analysis, since the soil properties are dependent on the effective stresses. Since all stresses at each point in a centrifuge model can be made the same as the corresponding point in the prototype, each element of soil can be expected to undergo the same response history as corresponding elements in the prototype.

A summary of the scaling relationships for geotechnical centrifuge model tests with earthquake shaking is given in Table 5.2 (43)

Table 5.2. Scaling Relationships in Centrifuge Modelling

Parameter	Ratio of Model to Prototype
Length	1/N
Velocity	1
Acceleration	N
Force	$1/N^2$
Stress	1
Energy	$1/N^3$
Frequency	N
Time	1/N
Permeability	N

A pressure chamber is analogous to a centrifuge, except that the effective stresses are uniform throughout the test sample. Based on the scaling relationships given in Table 5.2 for the centrifuge, an analysis (second-level scaling) has been performed to evaluate the prototype conditions that were modeled in the test chamber. The parameters considered were: (1) length, (2) pore water pressure dissipation (permeability), and (3) velocity (maintaining constant velocity between model and prototype). A step-by-step derivation of such an analysis is given in Appendix C. It was concluded that by scaling length, rate of pore water pressure dissipation (static analogy), and maintaining constant velocity in model and prototype, the following test chamber parameters were selected as follows:

(a) Isotropic confining pressure (chamber), or σ', = 5 psi,
(b) Micro-fine sand, with a coefficient of permeability (k) of 1.21×10^{-3} cm/sec,
(c) Pile length (model), or Lm, = 16 inches,
(d) Pile diameter (model), or dm, = 1.0 inch,
(e) Time scale (model), or tm, = 1/7 time scale (prototype), or tp, and,
(f) Acceleration (model), or am, = 7 times acceleration (prototype), or ap,

to affect similitude for a pile 27 inches in diameter, 40 feet long, in submerged SJR sand (with a coefficient of permeability of 1.3×10^{-1} cm/sec, and effective grain size, d_{10}, of 1.6 mm) at a site, approximately 75 km from the epicenter of a Magnitude 8.0 earthquake. The conclusion for 40-foot long pile should be conservative for pile lengths greater than 40 feet, since liquefaction or seismic induced cyclic mobility rarely occurs below 40 feet in the free field.

Induced Pressures in the Water Mass due to Vertical Seismic Excitation

A simplified analysis has been performed to evaluate the magnitude of water pressure induced by the simulated vertical excitation of the water mass. The conditions to be analyzed corresponds to an offshore location with an assumed water depth of 1000 feet, as shown in Fig. 5.13. Derivations and numerical computations of this analysis are presented in Appendix D.

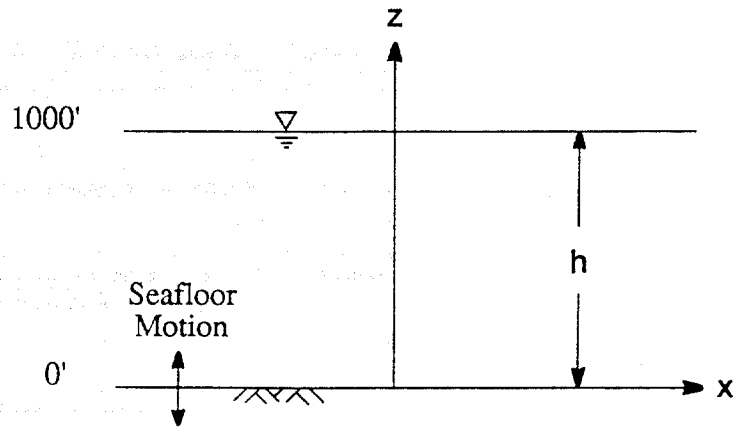

Fig. 5.13 . Assumed Conditions for Analysis of Induced Pressures in Water Mass Subjected to Vertical Seismic Motion.

Fig. 5.14 shows the record window of predominant strong shaking, in which two predominant frequencies can be observed, one high-frequency (1 Hz) low-displacement (0.05 in.) signal and one low-frequency (0.12 Hz) high-displacement (0.73 in.) signal. The magnitude of excess water pressure induced at the soil surface by the vertical motion is slightly greater than the applied effective stress in the test chamber (Appendix D). If this pressure produces pore pressure waves in the prototype soil, some shallow liquefaction could occur and pile capacity would be reduced. However, for purposes of evaluation of uplift capacity, it may be possible to assume that this phenomenon is uncoupled from the pile-soil-structure interaction being studied here. The test chamber capabilities for this study do not simulate the assumed conditions for this analysis.

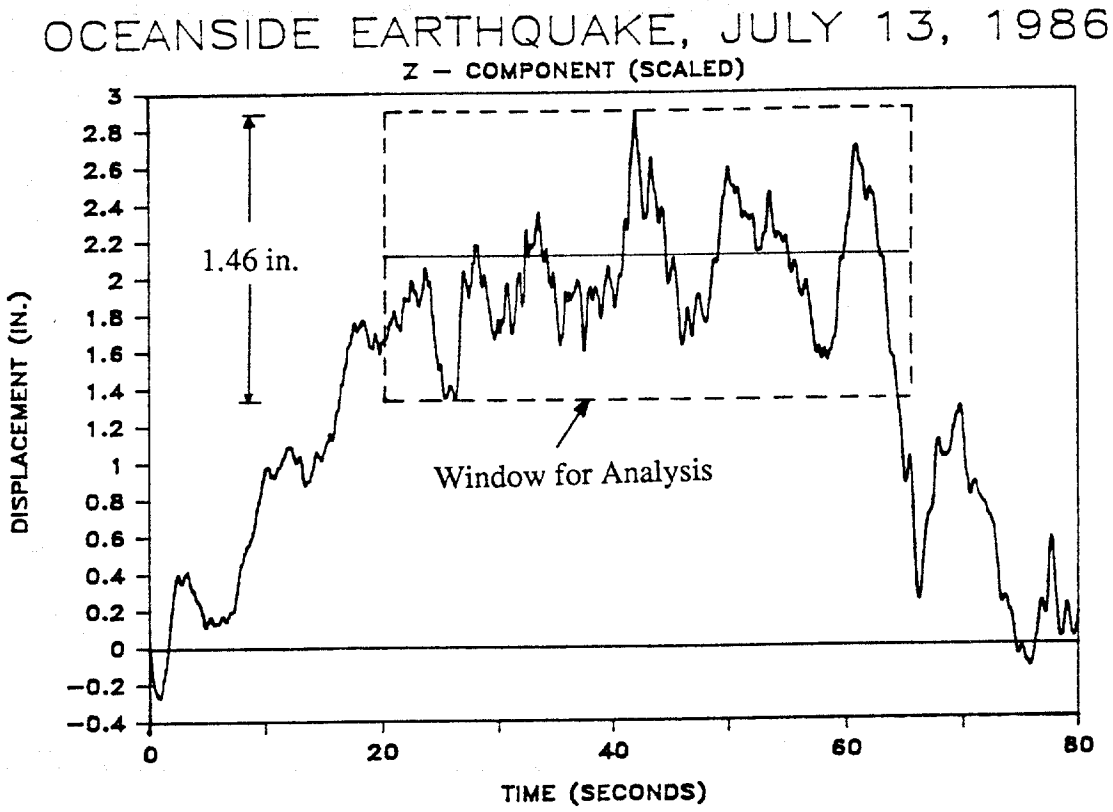

Fig. 5.14. Window Record for Induced Pore Water Pressure Analysis During a Simulated Vertical Seismic Event

CHAPTER VI

Analysis of Test Results

This chapter describes the analysis of relevant test data in order to develop a better understanding of the vertical dynamic response of axially loaded piles with tension bias under the vertical component of earthquake loading. The following aspects were investigated: (a) pore water pressure build-up during the impact driving of the pile (an indirect indication of the susceptibility of the test sand to pore water pressure generation during dynamic loading), (b) relationship between the penetration rate (blows/in) and uplift static capacity, (c) comparisons between the measured and target spectra, (d) ultimate uplift static capacities, (e) static load transfer characteristics, (g) pile and soil response during the simulated seismic event, (f) post-shaking static capacities after the seismic event, and (h) dynamic load transfer characteristics.

A summary of the test program results is given in Table 6.1. A total of 23 tests were performed. The first ten tests (A1-F) were static load tests that represented, for further comparisons, the baseline for the remaining thirteen dynamic tests (G-N2).

Induced Pore Water Pressure During Impact Driving

Measurements of induced pore water pressures generated by the impact driving of the pile were performed by means of the miniature pore water pressure transducers embedded in the soil mass (Fig. 4.2). Calibrated outputs for the transducer placed one inch from the pile wall for two typical tests, Test A3 (SJR sand) and Test F (Micro-fine sand), are displayed graphically in Fig. 6.1. Some comments can be made regarding Fig. 6.1. First, the induced pore water pressure for the micro-fine sand (Test F) is doubled when compared with the induced pore water pressure values for the SJR sand (Test A3). Smaller particle sizes and, therefore, a reduced coefficient of permeability of the micro-fine sand may have impeded the flow of pore water, inducing higher pore water pressures. Second, the highest positive values of induced pore water pressures were measured when the pile toe was nearest the instrument level. Once the pile toe passed this point, negative pore water pressures were developed in the field around the instrument. Driving effects were negligible when the pile toe was located 2.5 diameters and 4 diameters below the

Table 6.1. Summary of Test Program Results

Test No.	Type of Test: Static (Base-Line)/ Dynamic	Type of Static Loading: CD / CL	Condition: D_r (%) / σ_c (psi) / Qbias (lb) (% of Inferred Static Capacity)	Static Capacity for Dynamic Test Inferred from Blow Count (lb)	Pullout Failure Observed ?	Static Capacity or Post-Shaking Static Capacity (lb)[a] (% of Inferred Static Cap.)
A1	Static	CD	55 / 5 / 0		-	270
A2	Static	CD	55 / 5 / 0		-	250
A3	Static	CL	55 / 5 / 0		-	220
B1	Static	CD	70 / 5 / 0		-	390
B2	Static	CL	70 / 5 / 0		-	241
C	Static	CD	78 / 5 / 0		-	560
D	Static	CD	85 / 5 / 0		-	550
E1	Static	CD	55 / 2.5 / 0		-	100
E2	Static	CL	55 / 2.5 / 0		-	120
F	Static[b]	CL	55 / 5 / 0		-	179
G	Dynamic	CD	55/5/60 (23)	257 (8.3 b/in)	No	260 (101)
H1	Dynamic	CL	55/5/123(48)	257 (8.3 b/in)	No	229 (89)
H2	Dynamic	CL	55/5/80(59)	138 (5.0 b/in)	No	127 (92)
I1	Dynamic	CL	55/5/156(89)	176 (6.0 b/in)	Yes	-
I2	Dynamic	CL	55/5/243(90)	268 (8.6 b/in)	Yes	-
J	Dynamic	CL	70/5/228(74)	310 (10 b/in)	No	318 (103)
K	Dynamic	CL	70/5/335(92)	366 (12 b/in)	Yes	-
L1	Dynamic	CD	55/2.5/184 (62)	301 (9.7 b/in)	No	264 (88)
L2	Dynamic	CL	55/2.5/87(88)	99 (4.0 b/in)	Yes	-
M1	Dynamic[b,d,e]	CL	55/5/100(57)	176 (6.0 b/in)	No	168 (95)
M2	Dynamic[b,d,e]	CL	55/5/160 (90)	176 (6.0 b/in)	No	195 (110)
N1	Dynamic[d]	CL	55/5/111(52)	212 (7.0 b/in)	No	193 (91)
N2	Dynamic[d]	CL	55/5/214(95)	224 (7.3 b/in)	No	239 (106)

a Static failure (baseline or post-shaking loading tests) defined at load that produced initial interface slip, whether CD or CL Test.

b Conducted with micro-fine sand[c]. Other tests conducted with standard test sand.

c Sand with a coefficient of permeability approximately 0.12 times that of SJR Sand (standard test sand) to scale drainage distance.

d Time scaled by a factor of 0.14 in the acceleration record to scale drainage distance and other length factors.

e Accelerations scaled by a factor of 7 in the acceleration record.

Notes:

1. Inferred static capacities for dynamic tests were obtained from the average blow count in the last 3 in. (3 diameters) of driving of the piles subjected to the dynamic test by comparing to relationship of measured static capacity to corresponding blow count (Tests A1 - F).

2. Biased loads (Q_{bias}) were the pure static tension loads imposed on the piles before initiation of shaking. Due to the spring and mass biased loading system, some cyclic load was superimposed on this static bias during shaking, the single amplitude value of which was approximately 10 per cent of the static bias load. Consult measured time histories of loading for more details.

3. CD refers to a controlled displacement test. CL refers to a controlled load test.

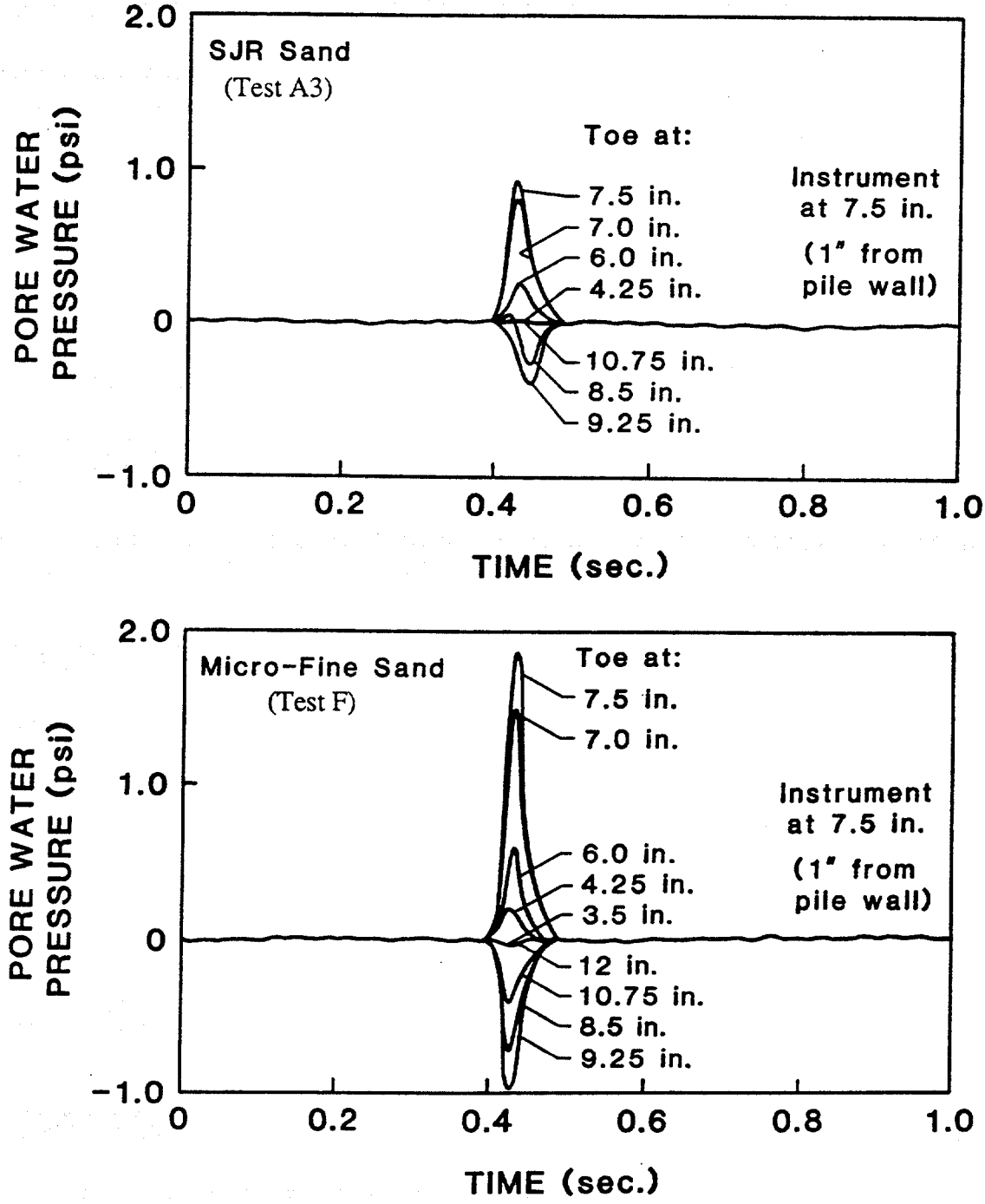

Fig. 6.1. Induced Pore Water Pressure due to Impact Driving, Test A3 and Test F, (σ_c' = 5 psi)

instrument level for SJR sand and micro-fine sand, respectively. Measurements with the far-field instrument were negligible, and therefore, are not shown here.

Relation Between Penetration Resistance and Uplift Static Capacities

Penetration resistance records (average blow count in the last 3 diameters of driving) versus the ultimate capacity for all static tests are shown in Fig. 6.2. The data have been fitted by a second-order polynomial equation which was used to infer the percentile of the static capacity corresponding to the applied bias load. For tests with similar confining pressures (σ_c' = 5 psi), an increasing trend of the static capacity with penetration resistance was observed, in which low and high values of penetration resistance corresponded to low and high values of relative density, respectively.

Comparison of Measured and Target Spectra

The actual acceleration spectrum measured by means of a low-g accelerometer mounted underneath the chamber bottom plate in Test H2 is shown in Fig. 6.3. The resulting (measured) spectrum indicated a reasonable match between the target (scaled) spectrum and the applied motion below 3.5 Hz, but some loss of energy above 3.5 Hz, possibly due to the filtering caused by the limitation of the servo-hydraulic system of the Instron testing machine.

Static Uplift Capacities

Graphical results of all static pull-out tests are shown in Figs. 6.4 - 6.8 in the following groupings:

(a) Tests at an effective chamber pressure of 5 psi and relative density of 55% (Fig. 6.4).

(b) Tests at an effective chamber pressure of 5 psi and relative density of 70% (Fig. 6.5).

(c) Test at an effective chamber pressure of 5 psi and relative density of 78% (Fig. 6.6).

(d) Test at an effective chamber pressure of 5 psi and relative density of 85% (Fig. 6.7).

(e) Tests at an effective chamber pressure of 2.5 psi and relative density of 55% (Fig. 6.8).

$$y = -76.516 + 47.484x - 0.877x^2$$

[y = load; x = b/in.]

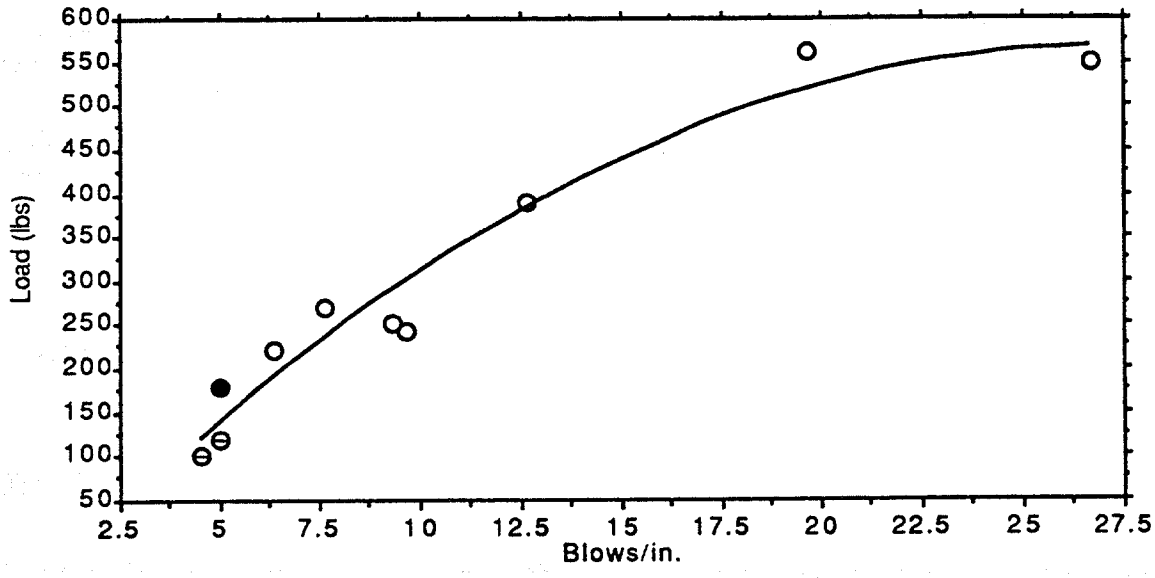

0 SJR sand, σ_c'= 5 psi; ● Micro-fine Sand, σ_c'= 5 psi; θ SJR sand, σ_c'= 2.5 psi;

Fig. 6.2. Penetration Resistance (Blows/in.) versus Static Capacity (lbs) for all Static Tests.

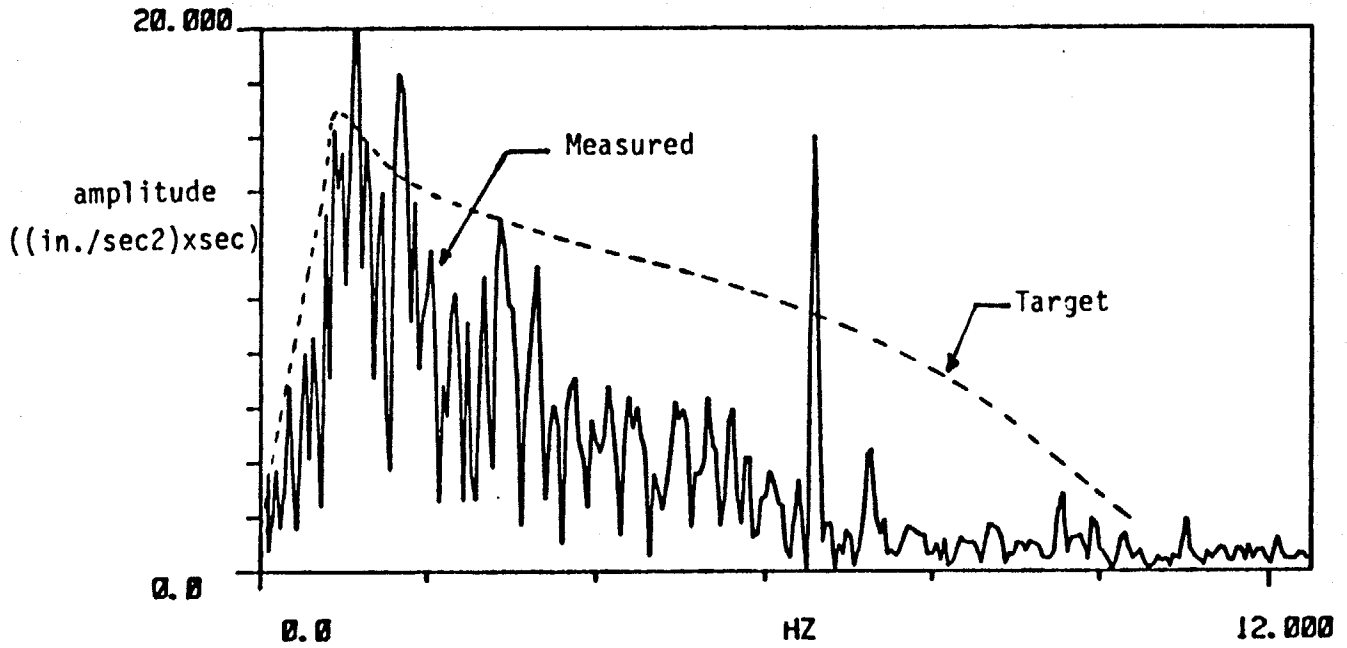

Fig. 6.3. Measured Spectrum versus Target Spectrum, Test H2.

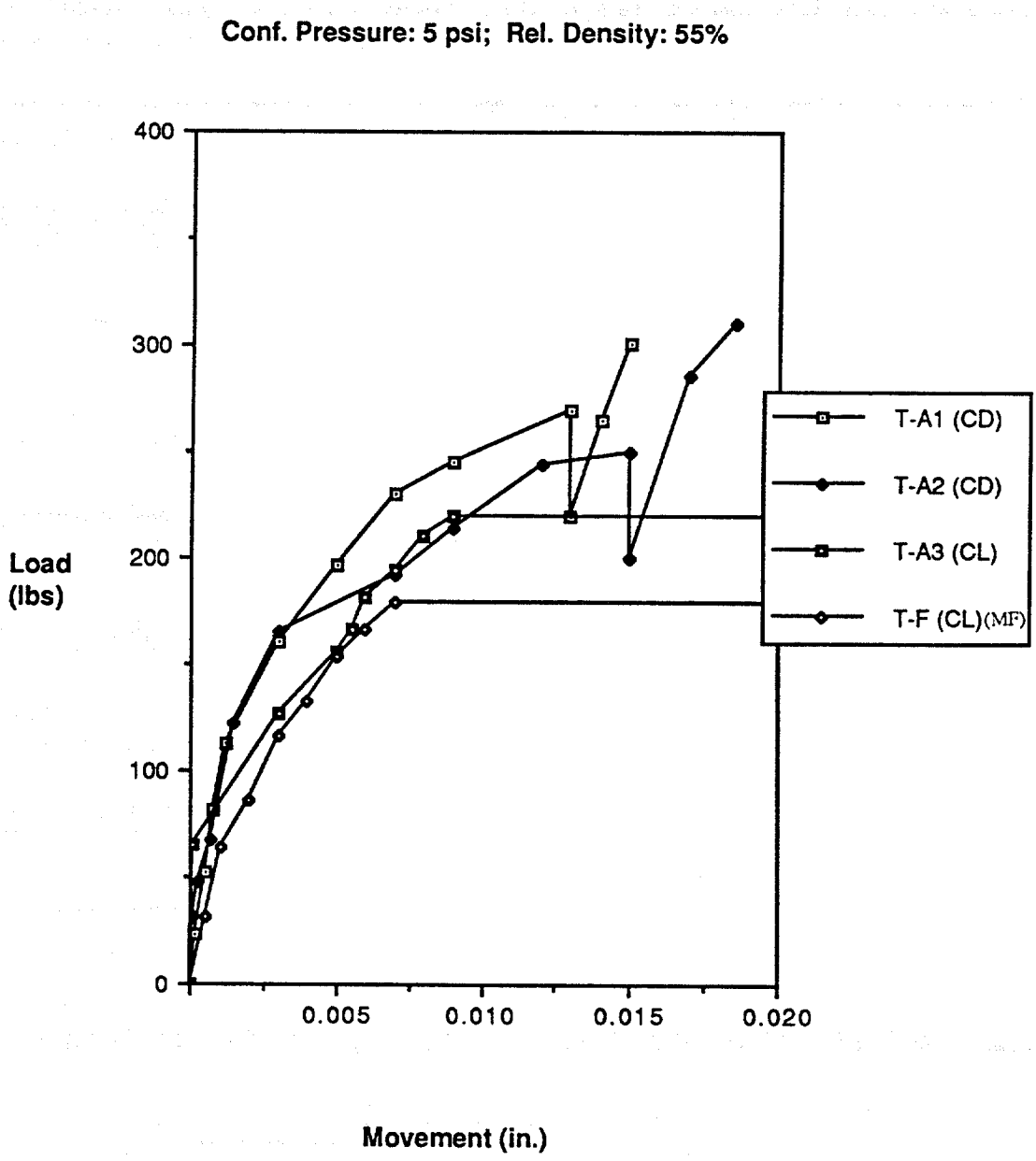

Fig. 6.4. Load-Movement Curves, Tests A1, A2, A3, F.

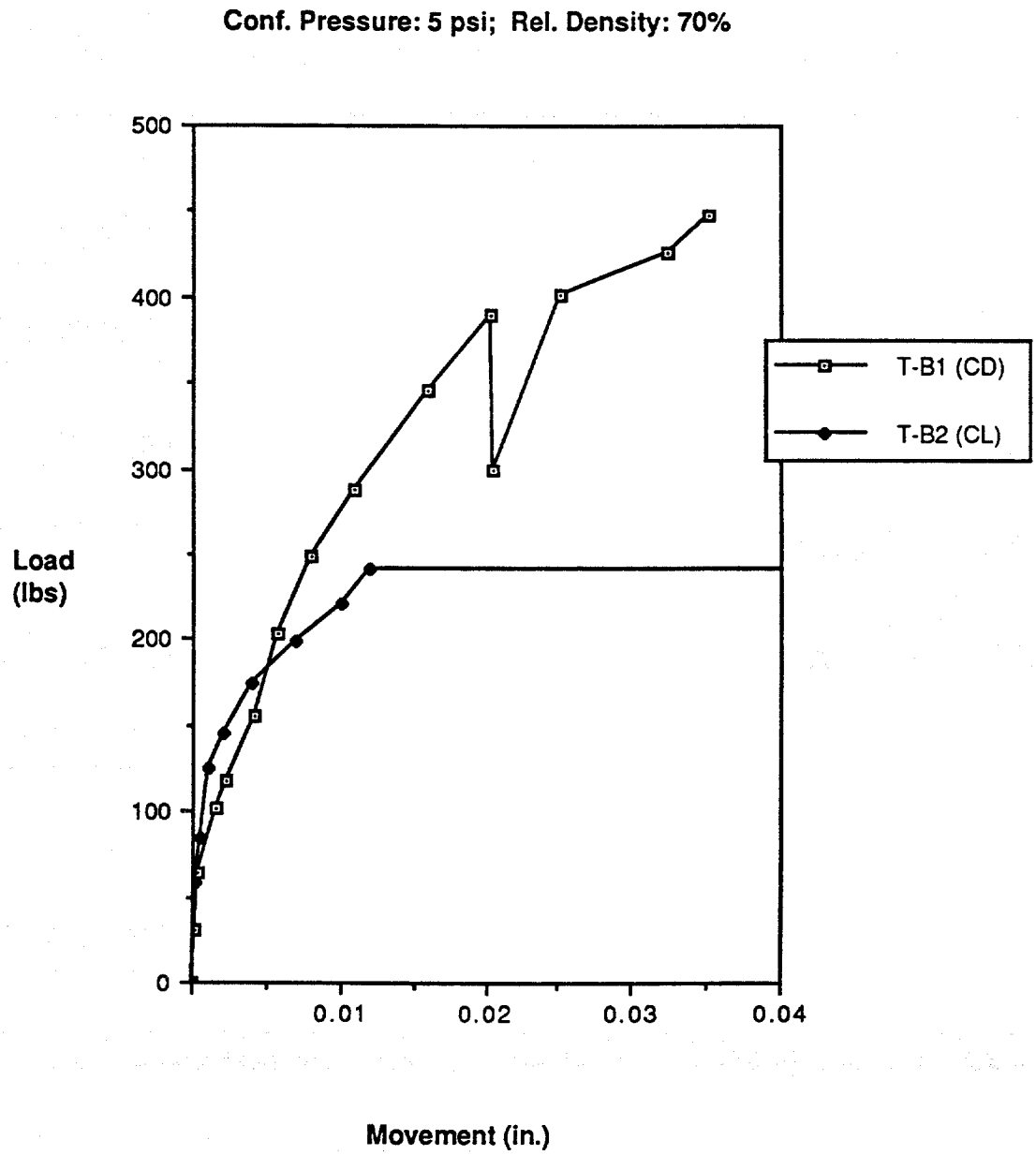

Fig. 6.5. Load-Movement Curves, Tests B1, B2.

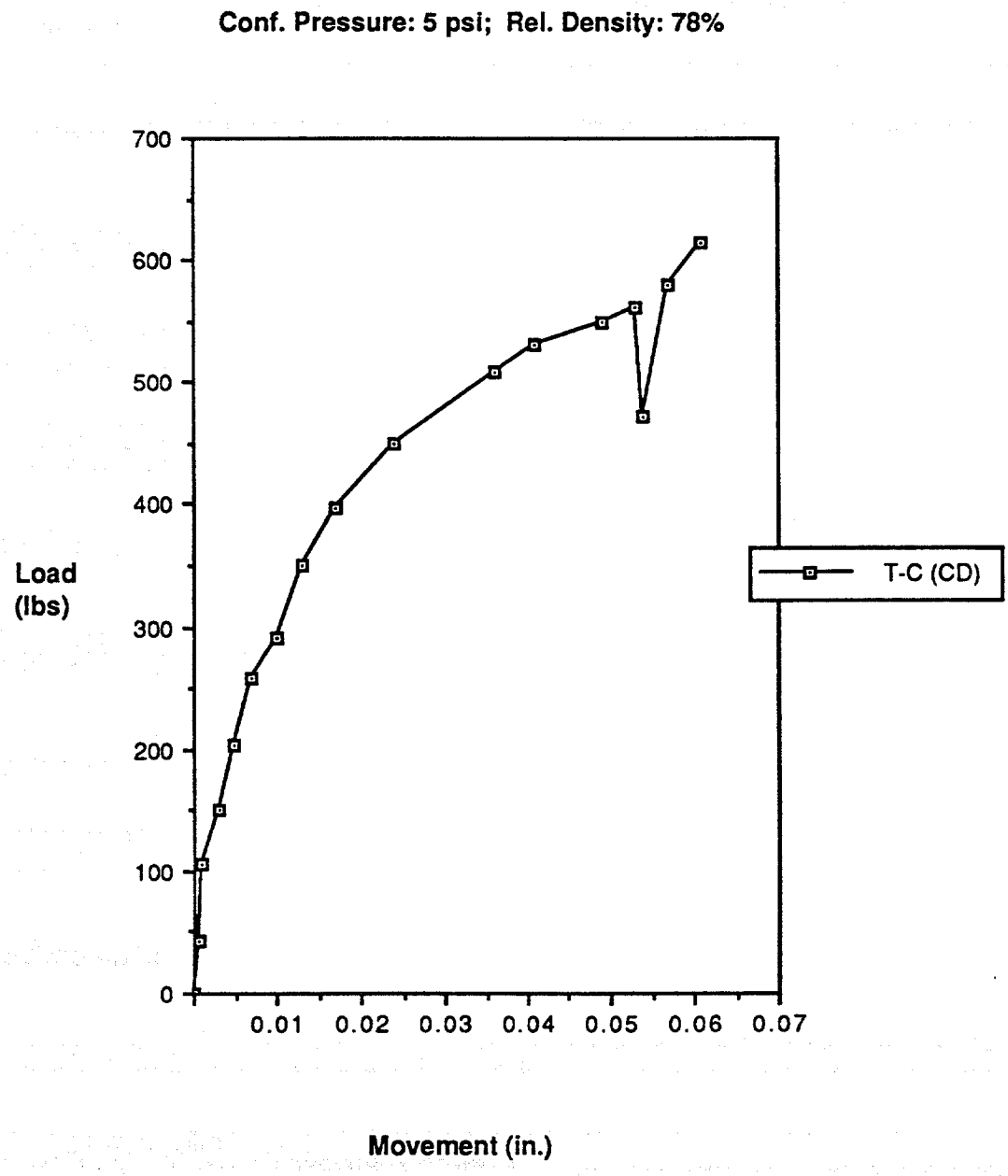

Fig. 6.6. Load-Movement Curve, Test C.

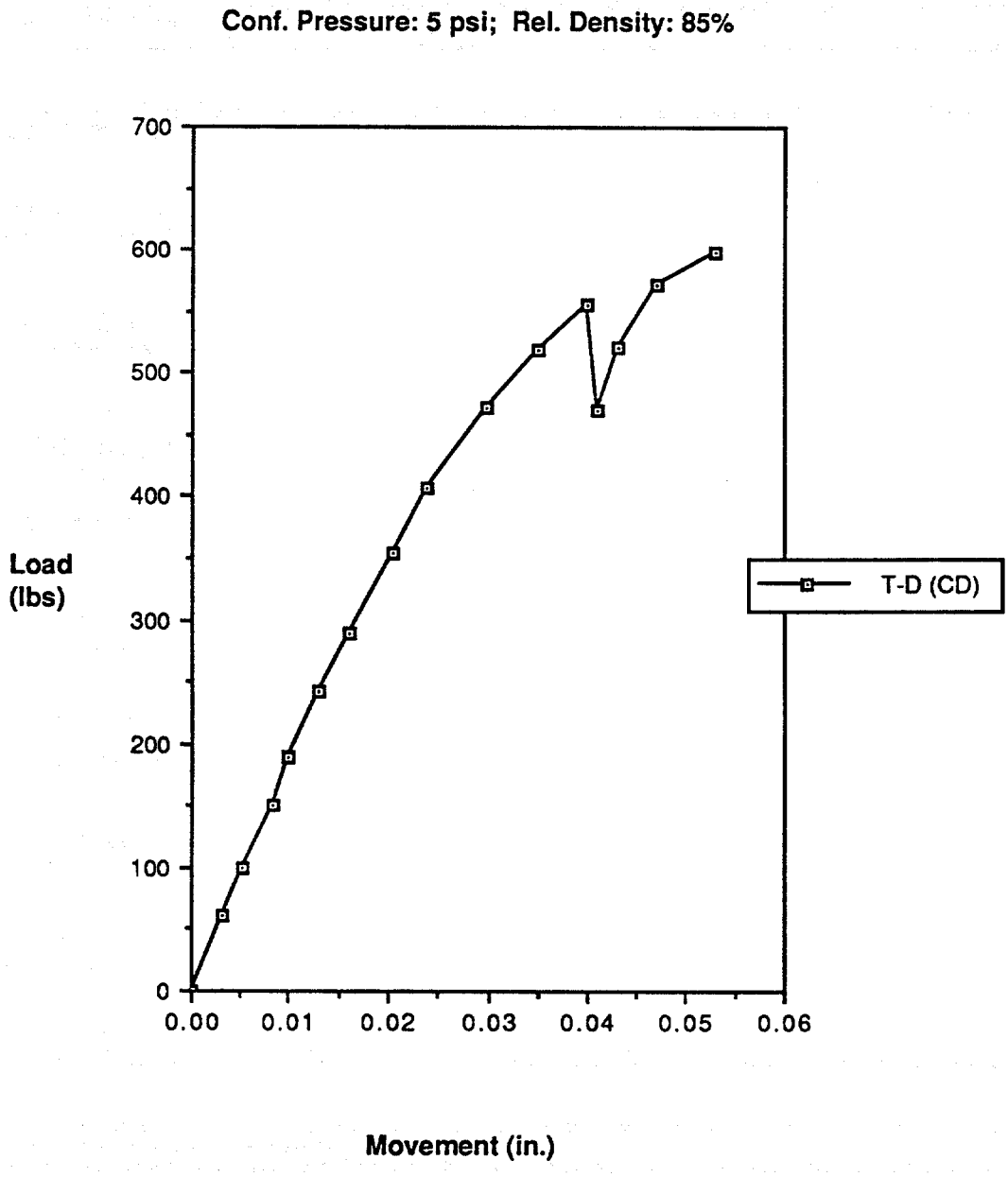

Fig. 6.7. Load-Movement Curve, Test D.

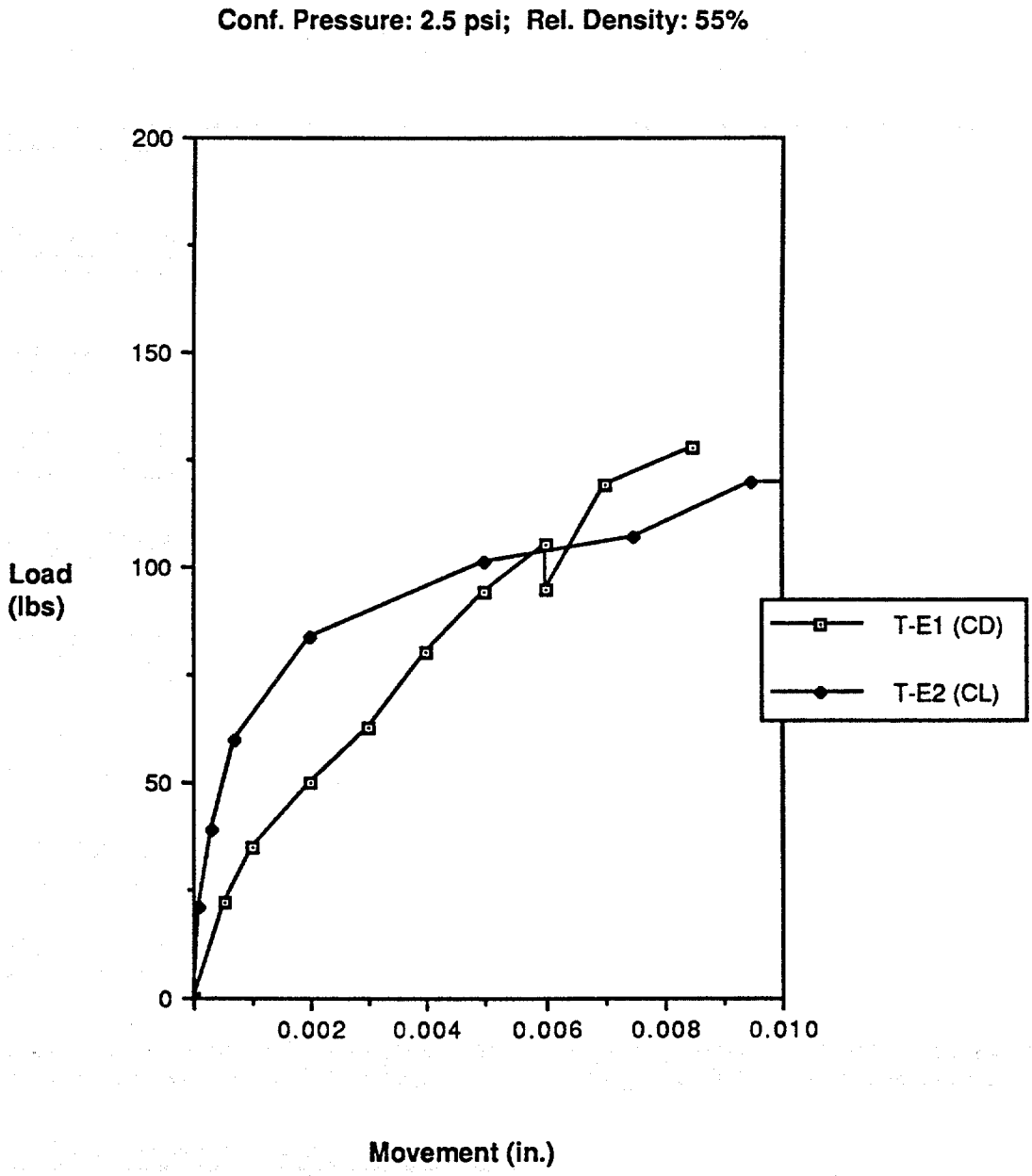

Fig. 6.8. Load-Movement Curve, Tests E1, E2.

Several observations can be made from the load-movement results:

(a) The uplift load-movement response exhibited similar trends.

(b) Controlled-Deformation (CD) tests produced higher capacities than those performed under Controlled-Load (CL) conditions. Failure for CD tests was considered to be when the first slip occurred, while for CL tests, failure occurred when the pile was suddenly pulled out from the test chamber.

(c) The effect of grain size is evident at an effective chamber pressure of 5 psi, as the fine grain sand (SJR sand) produced higher capacities than micro-fine sand (Fig. 6.4).

(d) The effect of the relative density on the static capacity is more pronounced at low relative densities than at high relative densities.

Static Unit Load Transfer Characteristics

Experimentally derived relationships of static unit shaft shearing resistance (f) to local pile movement (w) for all static tests (A1-F) are presented graphically in this section. Such information is useful in visually interpreting the development of load transfer at the pile-soil interface, particularly in terms of the relative effects of the test parameters. Unit load transfer relationships can be used to synthesize the static axial behavior of piles of dimensions different from those employed in this study, providing the effective stresses in the system are equivalent to those in the chamber.

In order to develop the relationships of f to w, it was necessary first to determine the load distribution along the pile. This was accomplished for every static test by using the calibrated output of the three strain gages placed at pile-head, mid-section and near-toe locations, respectively. Figs. E1-E10 in Appendix E show the load distribution for static tests A1-F. In all tests except for Test C the inferred load at the toe was zero or very small at failure. In Test C, a controlled displacement (CD) test in dense sand ($D_r = 78\%$), either some suction developed against the toe or extremely high side load transfer developed between the toe and lower level of strain gages. Considering the slow rate of movement in the CD tests (0.0033 in./sec), the latter explanation appears more plausible. In such plots negative values of load indicate tension, while positive values indicate compression. The weight of the pile is not explicitly included in the results since its effect was zeroed during the initial readings. Therefore, the strain gage readings represent the effect of external forces acting on the pile during the static load tests. It is emphasized that the measured load are based on zero readings taken before the pile was driven, and the unit load transfer

curves that were developed from these load distributions contain the effects of any residual stresses that were developed during the pile installation.

The f-w relations were developed for two sections: top half (0 - 7 in.) and bottom half (7 - 13 in.). Unit shaft load transfer, f, was computed from the following expression:

$$f = \frac{\Delta Q}{\pi dz} \tag{6.1}$$

where

ΔQ = Load difference in the pile,
d = Pile diameter, and
z = Top half or bottom half length difference.

The value of w is the pile-head displacement for the corresponding applied load, measured by means of the LVDT mounted to the pile head. This process was repeated for each load to develop sets of points defining the f-w relations. The unit shear transfer and the movements from these relations were then normalized by the effective horizontal chamber pressure, σ'_h, and the pile diameter, d, respectively. Figs. 6.9 - 6.13 show the normalized f-w relationships for each of the static tests grouped according to the confining pressure and relative density, for both top and bottom sections.

Several observations from Figs. 6.9 - 6.13 can be made:

(a) Greater maximum values of unit shaft resistance occurred in the lower half of the pile (depths greater than 7 diameters).

(b) Average ultimate f values divided by the mean effective chamber pressure for all load tests from Figs. 6.9 - 6.13 were

Top Half of the Pile	0.59
Bottom Half of the Pile	1.74

These data suggest that a surface effect existed during uplift loading, whereby the free, pressurized surface of the sand within the chamber permitted development of shear planes

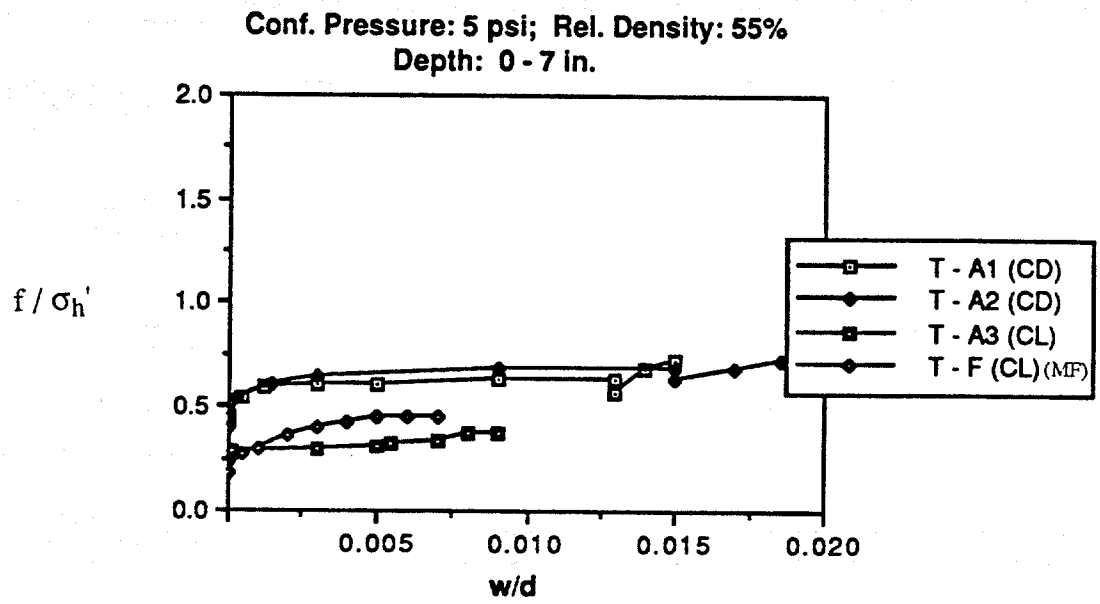

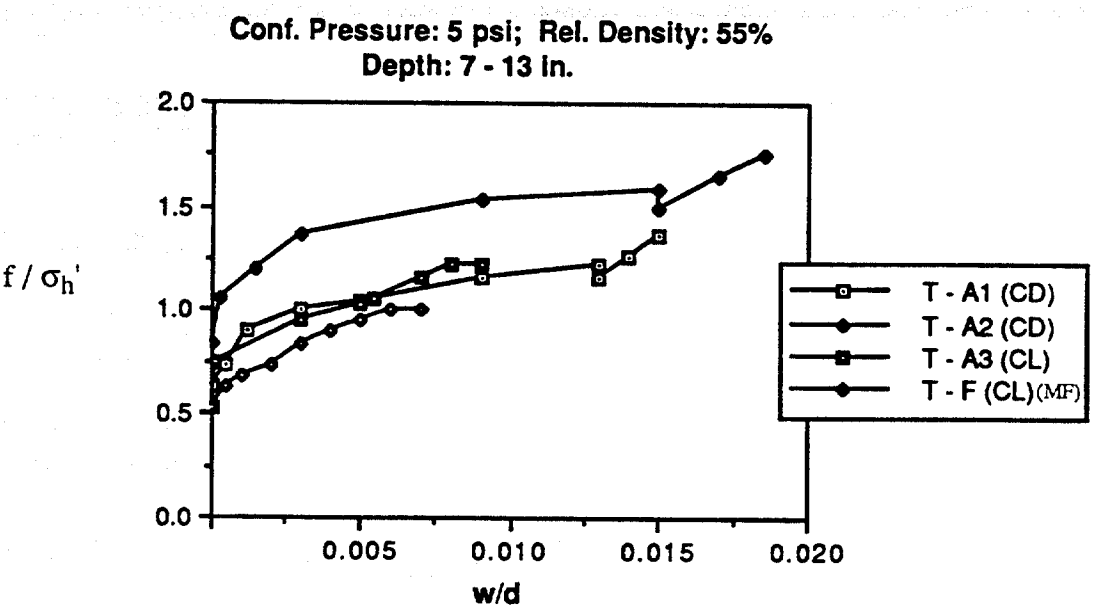

Fig. 6.9. f-w Relationships, Tests A1, A2, A3, F.

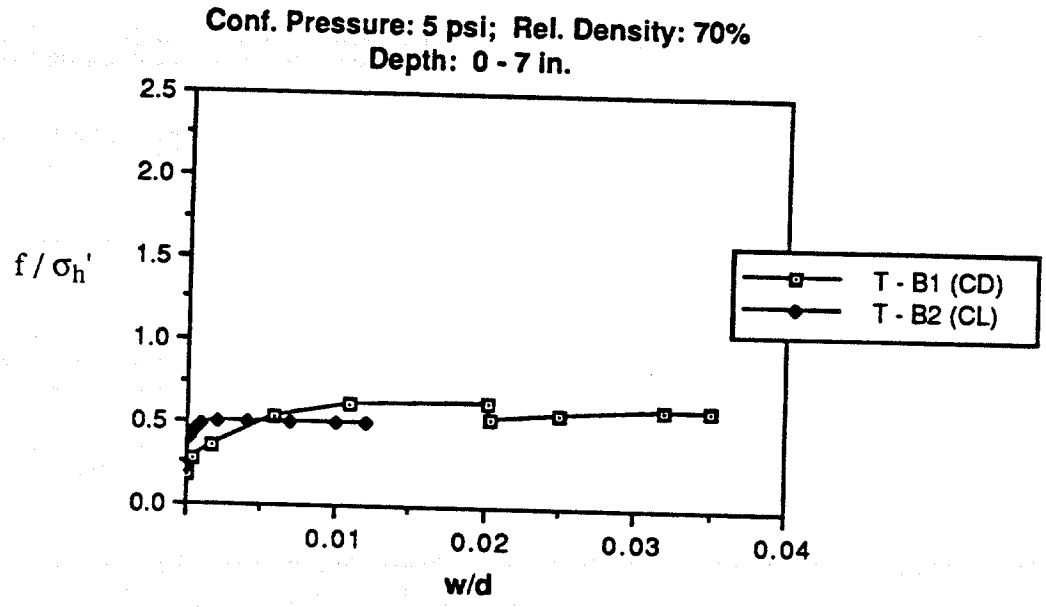

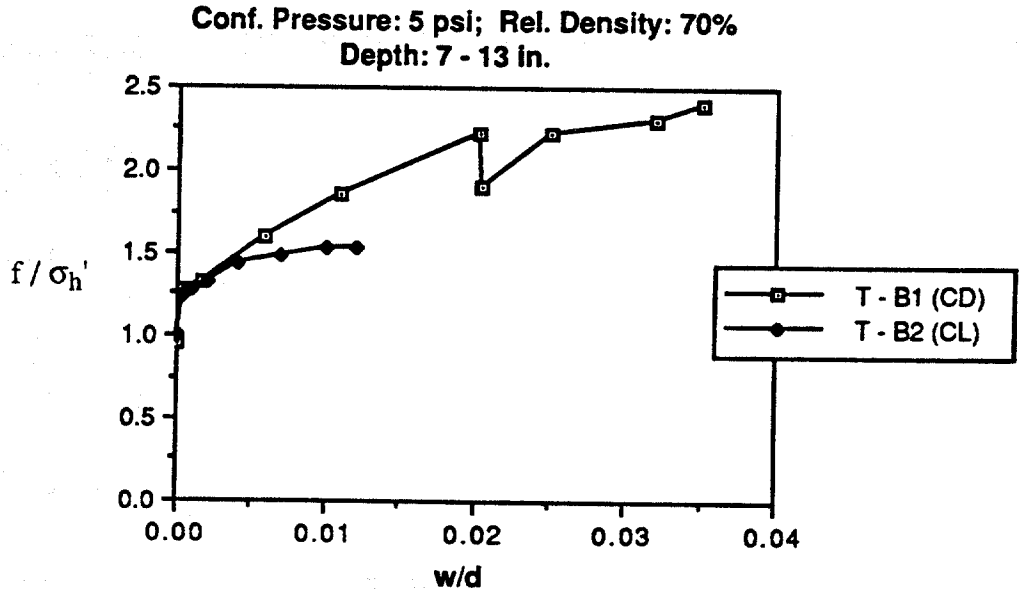

Fig. 6.10. f-w Relationships, Tests B1, B2.

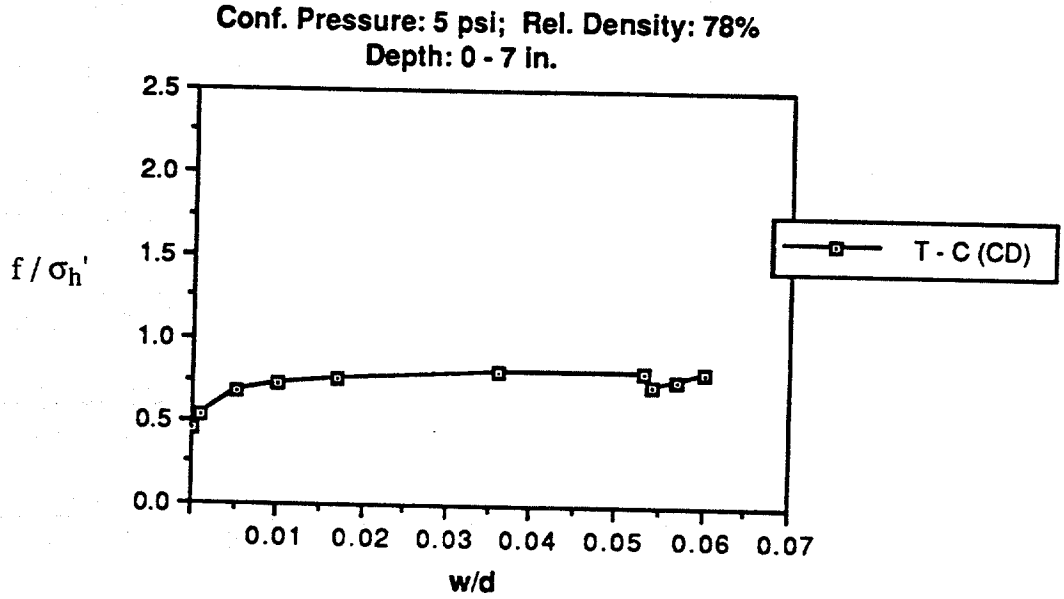

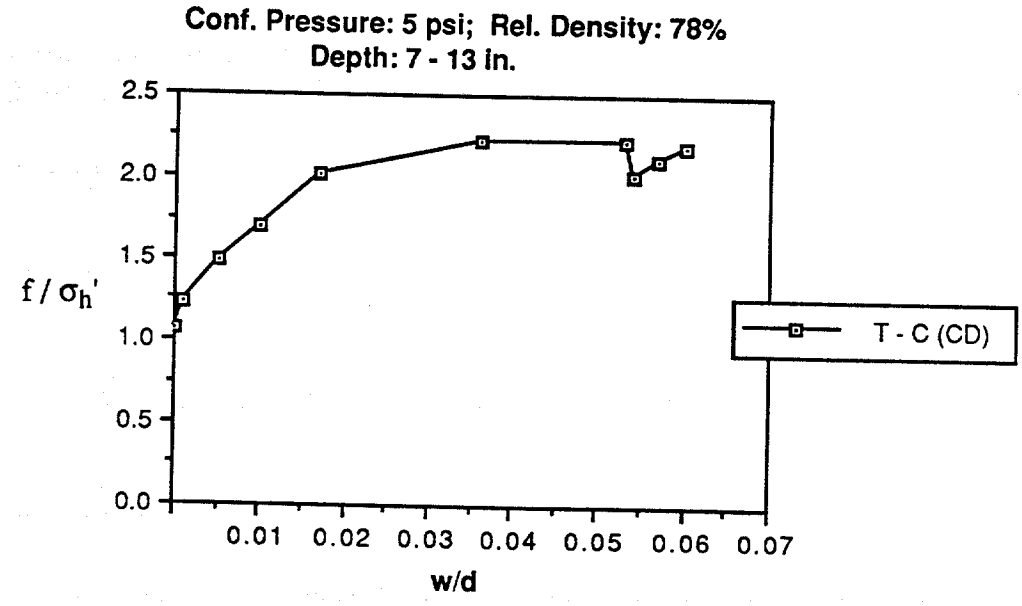

Fig. 6.11. f-w Relationships, Test C.

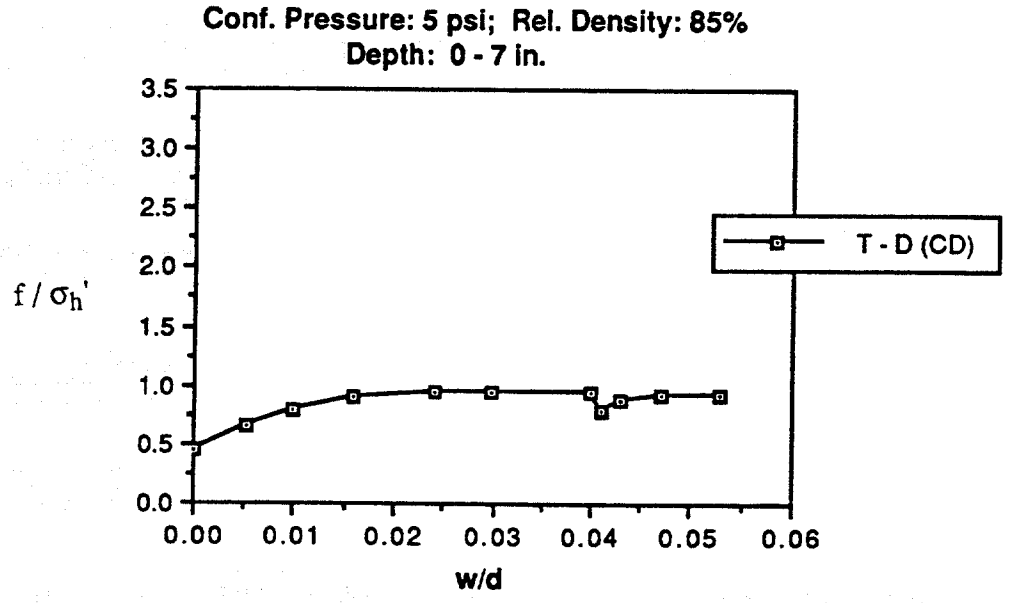

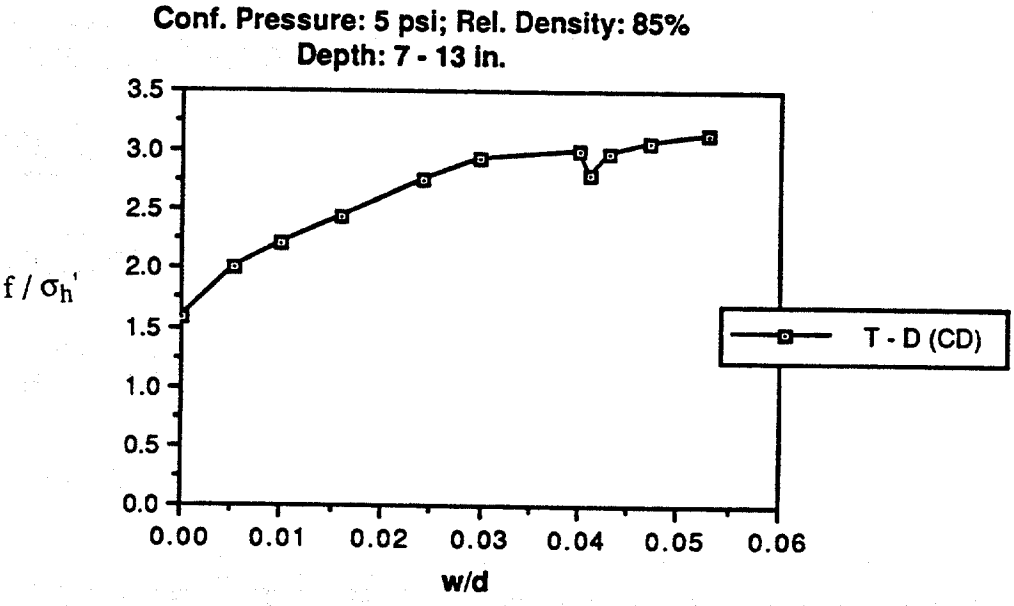

Fig. 6.12. f-w Relationships, Test D.

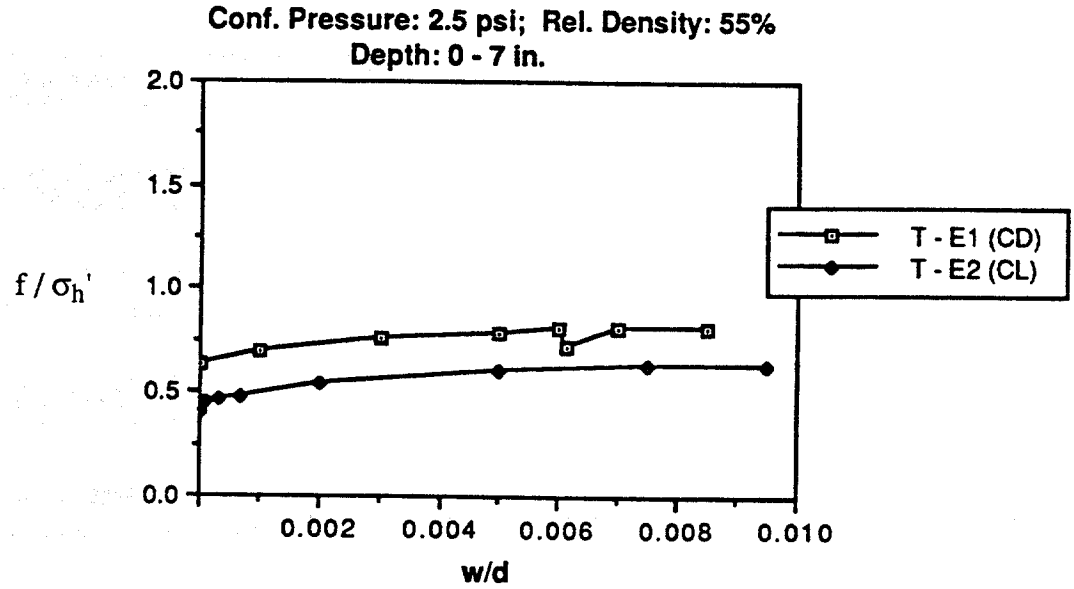

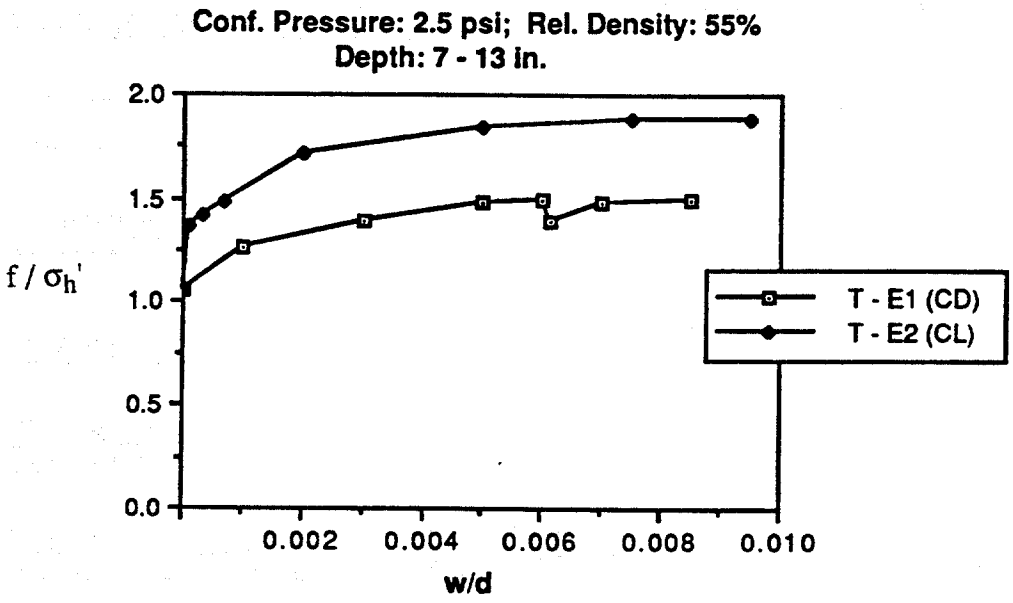

Fig. 6.13. f-w Relationships, Tests E1, E2.

at an angle to the interface, which possessed a lower shear strength than the interface plane, and which, therefore, permitted failure to occur at a lower interface shearing stress.

(c) The ultimate value of f was, on the average, for all tests on SJR sand, 102% of the lateral effective chamber pressure for $D_r = 55\%$. Since the angle of the interface shear was, approximately, 27° (Fig. 4.5), it can be demonstrated that the insertion of the pile into the chamber produced an increase in the horizontal effective stress in the chamber at the pile-soil interface. Assuming that $f_{max} = \sigma'_h \tan \delta$, where σ'_h = horizontal effective stress at the pile-soil interface, and δ = angle of interface shear (27°), the average horizontal effective stress at the pile-soil interface can be computed to be 1.02 / tan 27° = 2.0 times the simulated horizontal in-situ (lateral effective chamber) pressure for $D_r = 55\%$. The pile, therefore, must have served to increased the effective stress in the soil immediately surrounding the pile, as is predicted by expanding cavity models (45), which may served to resist liquefaction (e.g., as produced by excited water column).

(d) On average, the ultimate values of f were developed at local displacements of 1% of the pile diameter.

(e) Much of the unit side load transfer (typically 40 - 60%) was already developed in the form of residual stresses before the pile was subjected to uplift loading.

Pile and Soil Response During the Simulated Seismic Event

Time History measurements of (1) load on the pile at the strain gage locations, (2) generation of pore water pressures (near field and far field), and (3) pile head movement during the simulated seismic event were taken for all dynamic tests (G-N2). Data for representative tests, H1, I2 and K, are shown in Figs. 6.14 - 6.24. Data from other dynamic tests are presented in Appendix F. Test H1 represents the condition in which the pile capacity was not influenced by the vertical excitation of the seismic event. Test I2 represents the case where the pile was failed (pulled out) during the seismic event, mainly due to the bias load-spring-pile dynamic interaction. Test K can be considered as a near-failure condition, characterized by sustained pile capacity during the seismic event but with associated pile movement. Particular descriptions of Tests H1, I2 and K are as follows.

(a) **Test H1:**

(1) Time history of load measurements in the pile during the seismic event at three locations, the pile head, at a depth of 7 in., and 1.0 in. above the pile toe, are shown in Fig. 6.14.

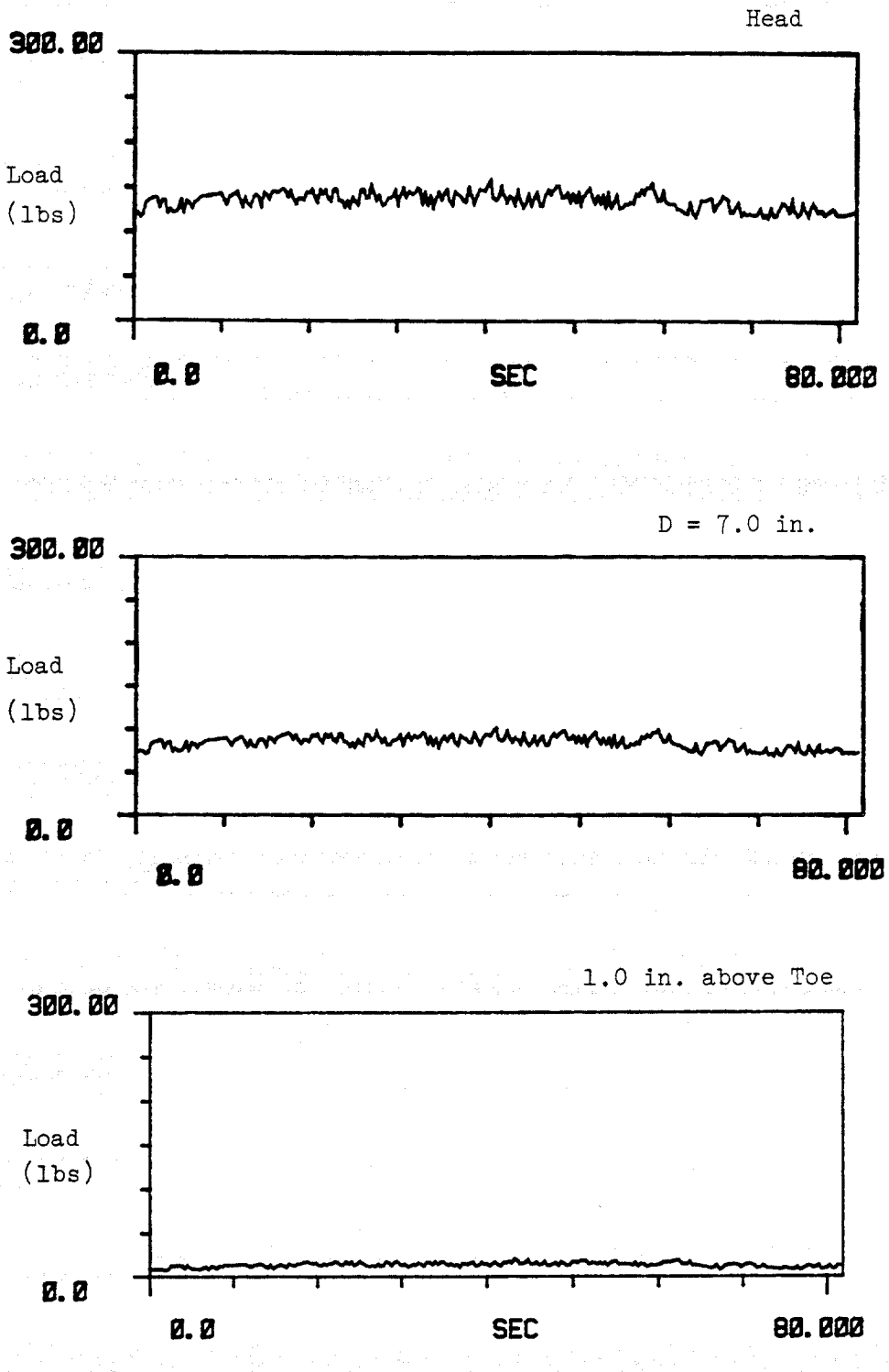

Fig. 6.14. Time History Measurements of Dynamic Load on Pile, Test H1.

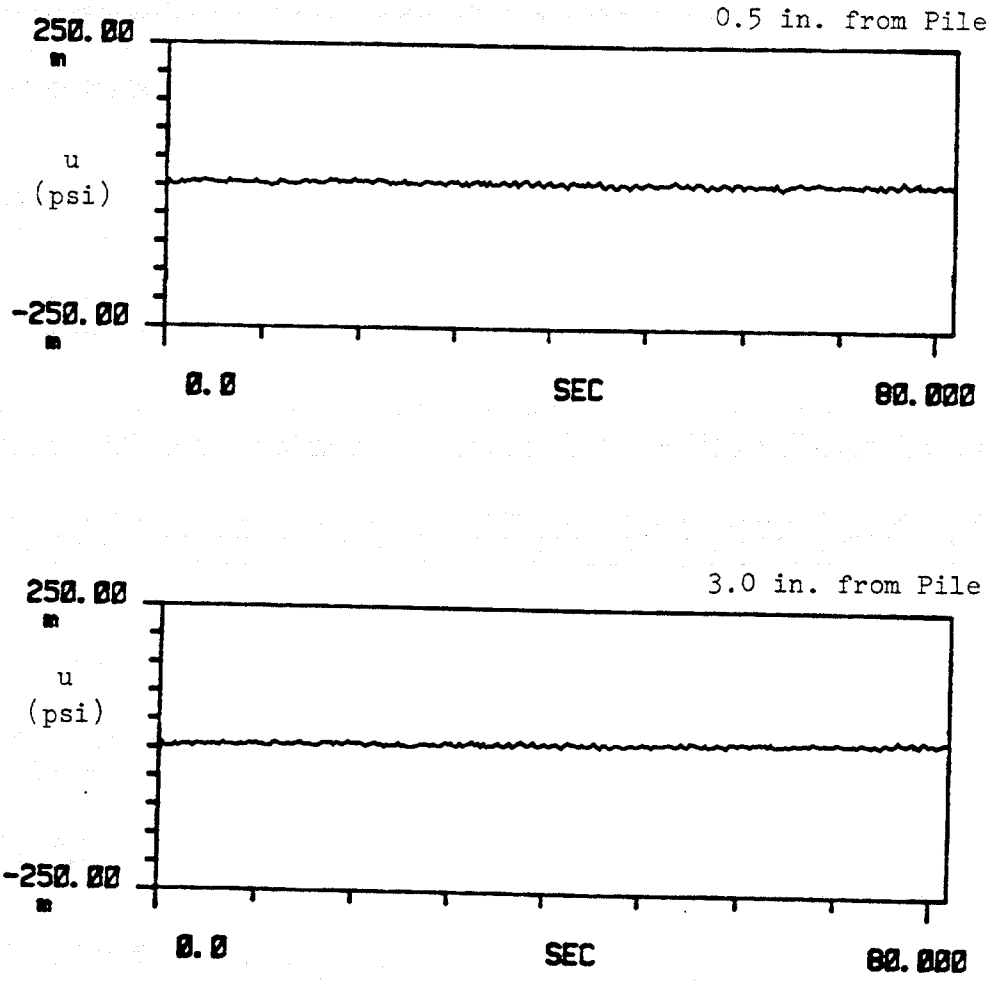

Fig. 6.15. Time History Measurements of Near and Far Field Pore Water Pressures, Test H1, [m = milli].

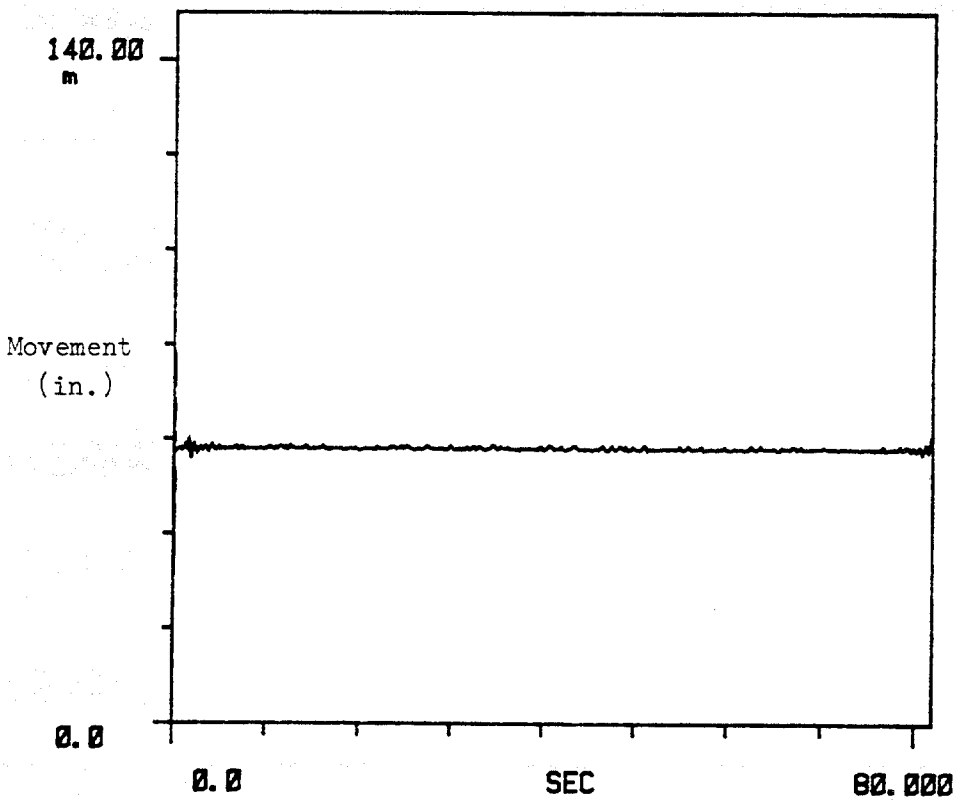

Fig. 6.16. Time History Measurements of Pile Head Movement, Test H1, [m = milli].

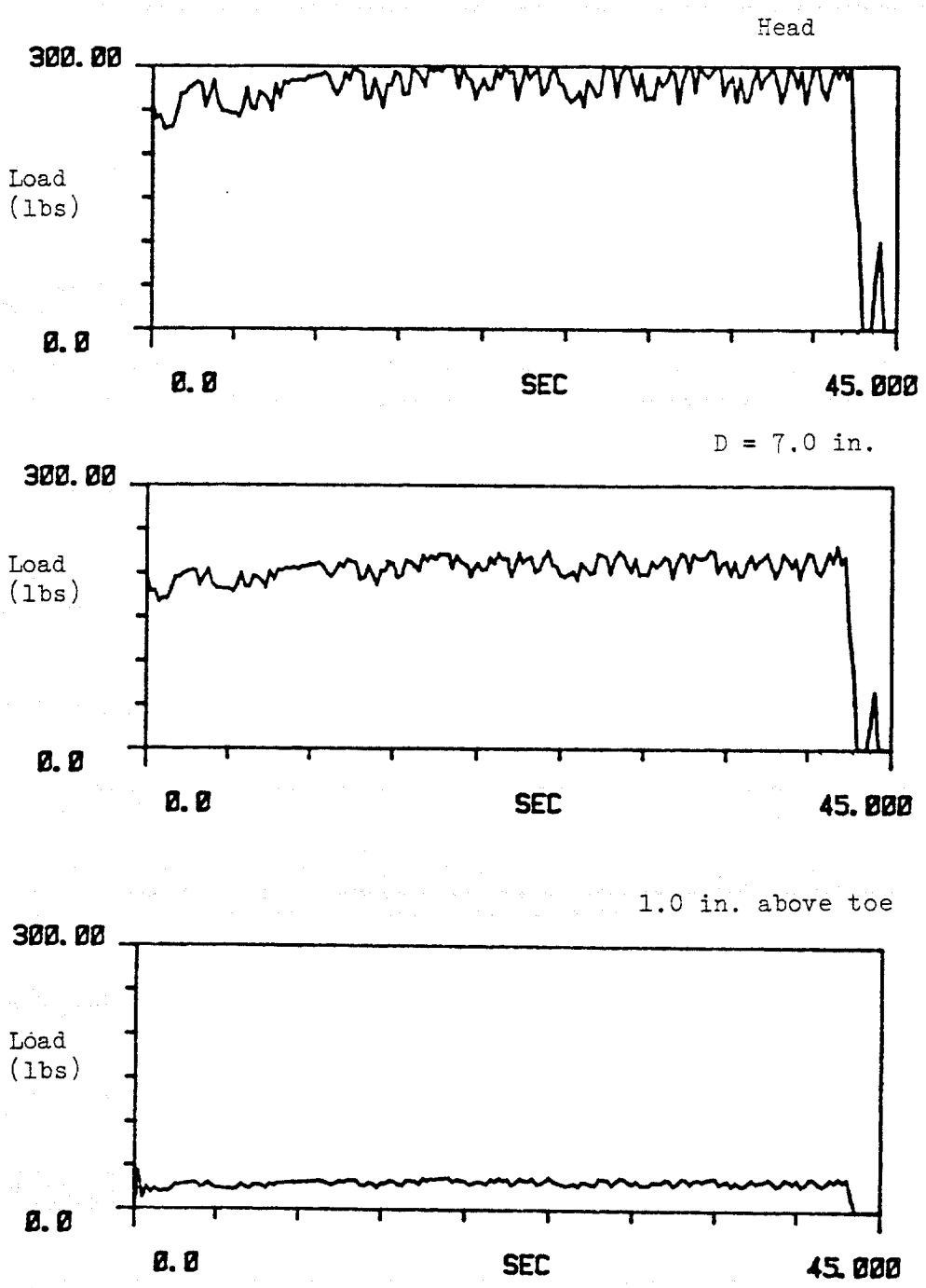

Fig. 6.17. Time History Measurements of Dynamic Load on Pile, Test I2.

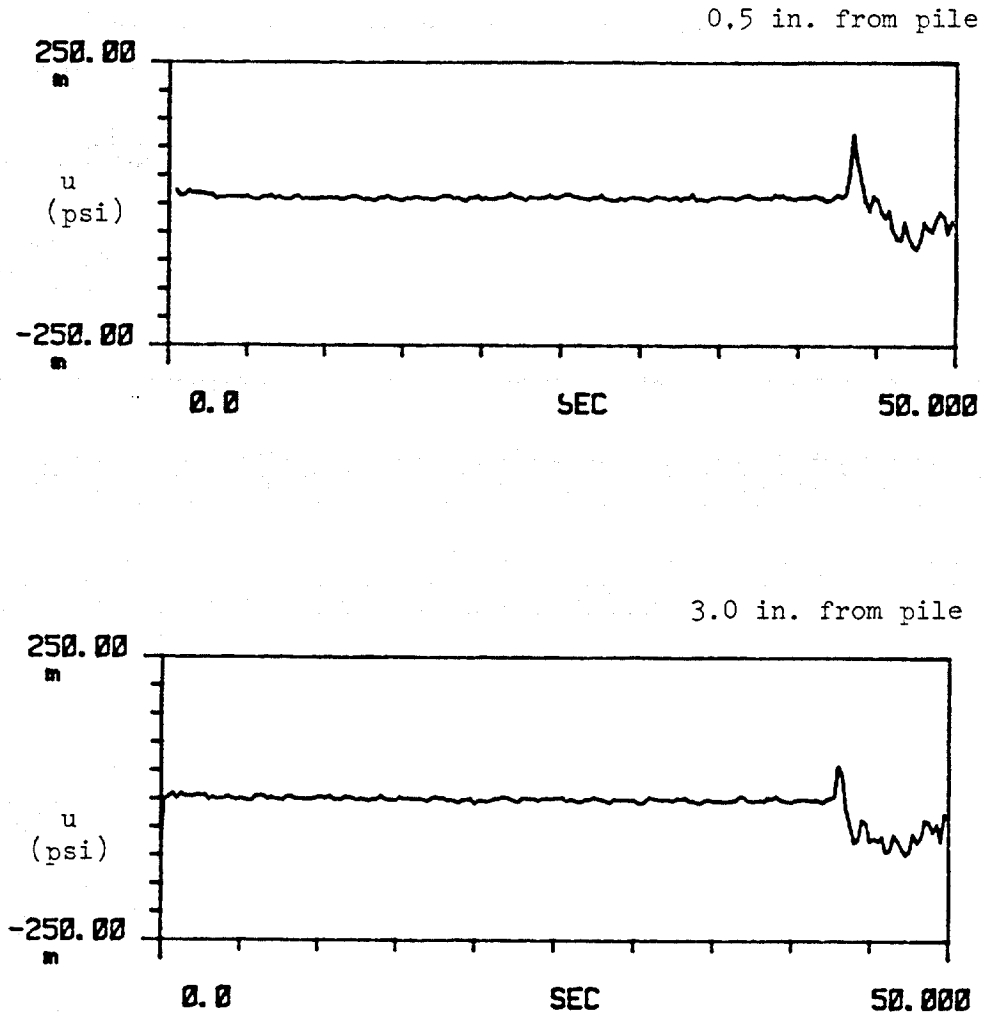

Fig. 6.18. Time History Measurements of Near and Far Field Pore Water Pressures, Test I2, [m = milli].

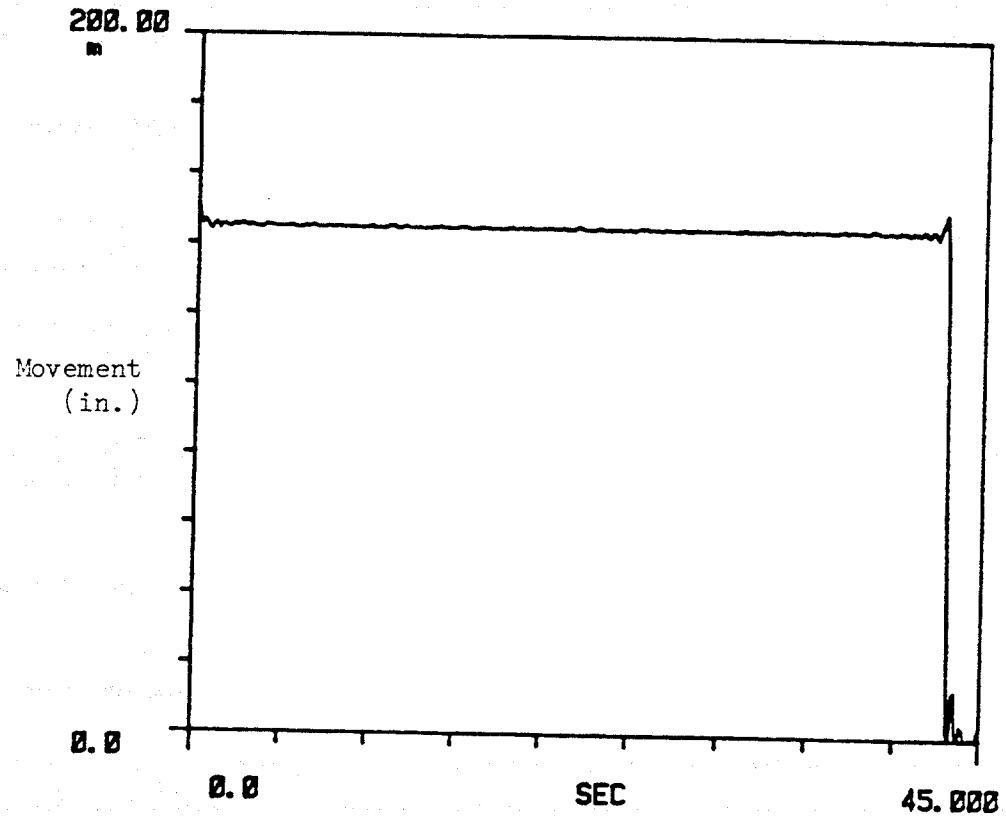

Fig. 6.19. Time History Measurements of Pile Head Movement, Test I2, [m = milli].

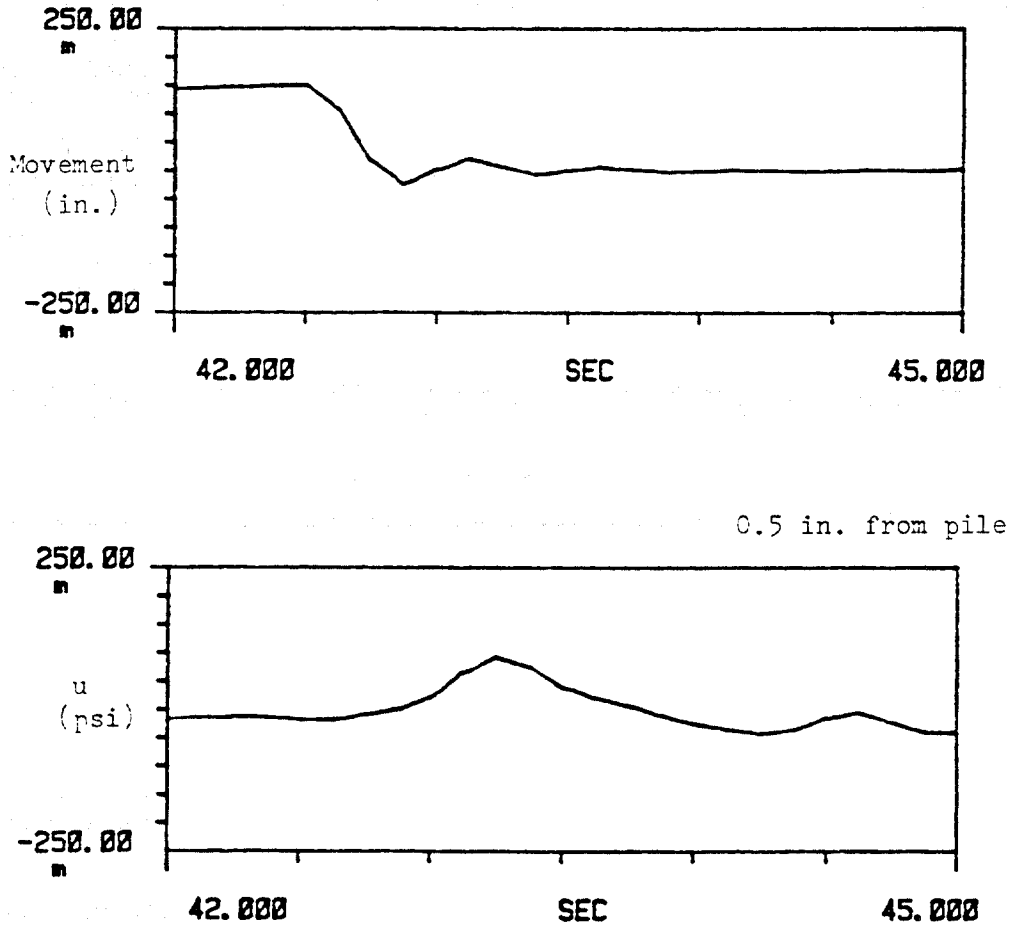

Fig. 6.20. Time History Measurements of Pile Head Movement and Near Field Pore Water Pressure, Test I2, [m = milli].

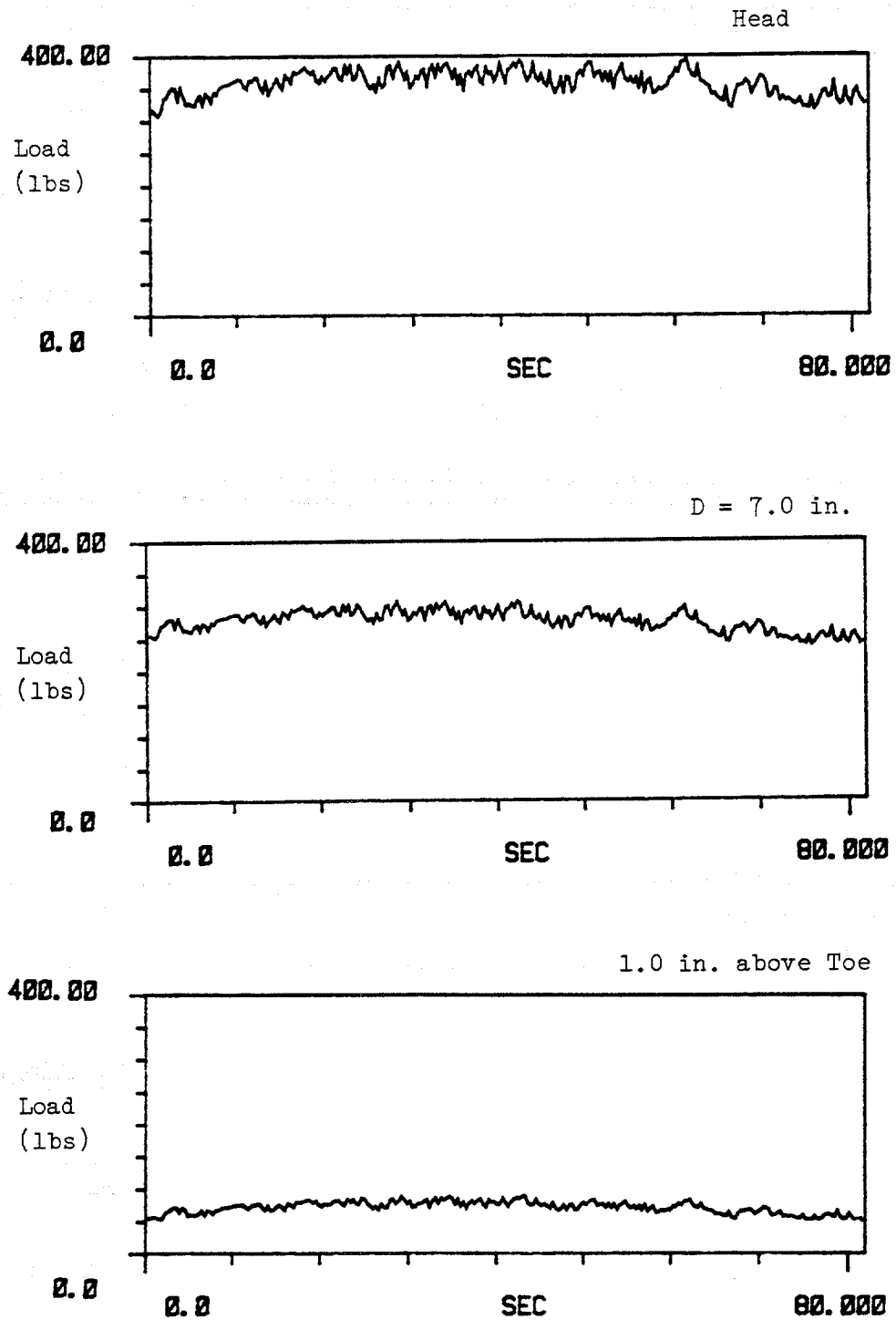

Fig. 6.21. Time History Measurements of Dynamic Load on Pile, Test K.

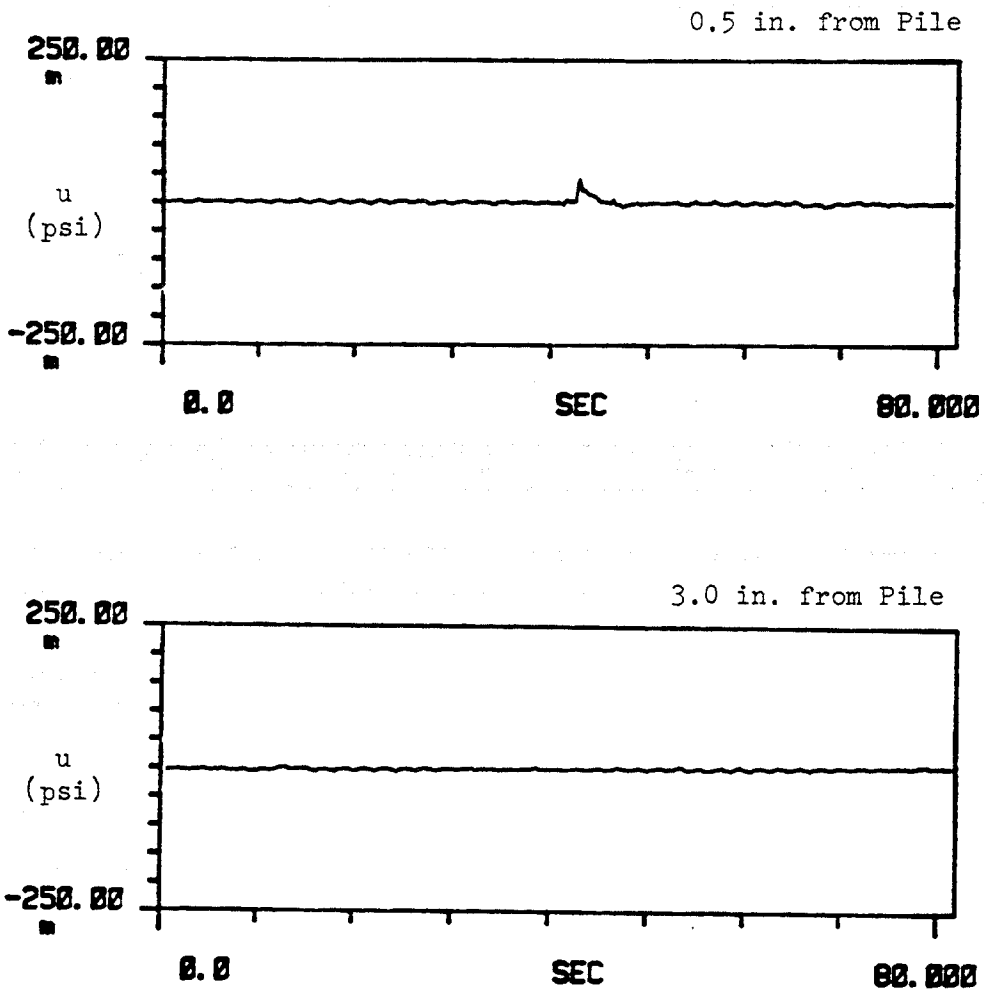

Fig. 6.22. Time History Measurements of Near and Far Field Pore Water Pressures, Test K, [m = milli].

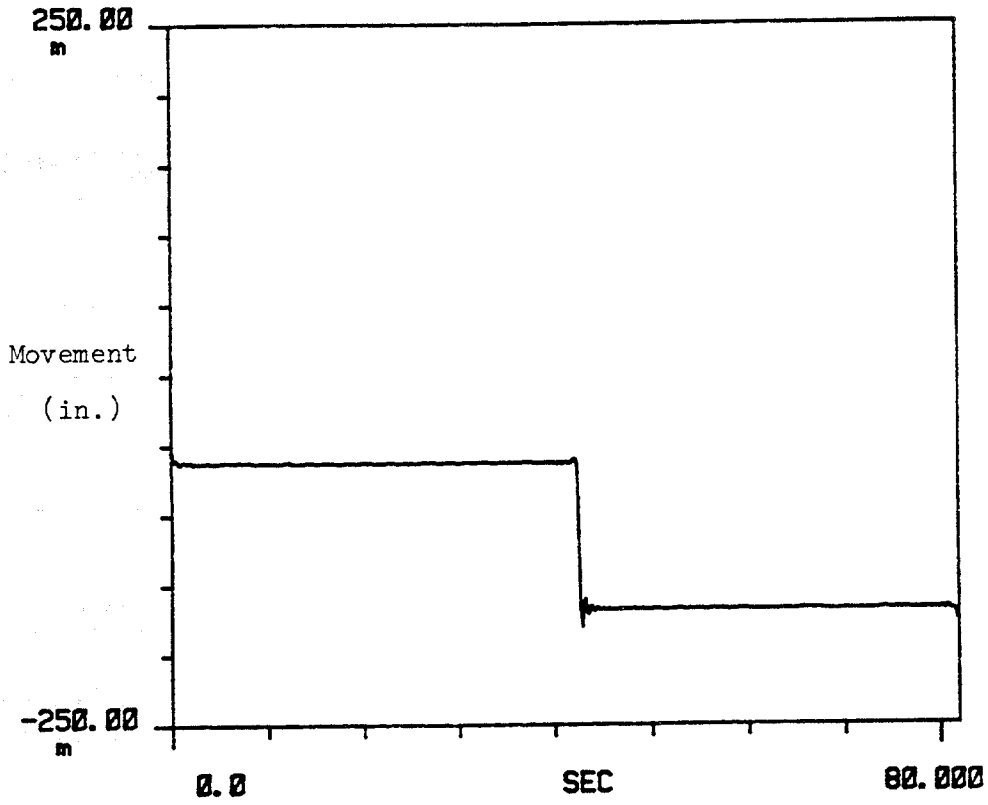

Fig. 6.23. Time History Measurements of Pile Head Movement, Test K, [m = milli].

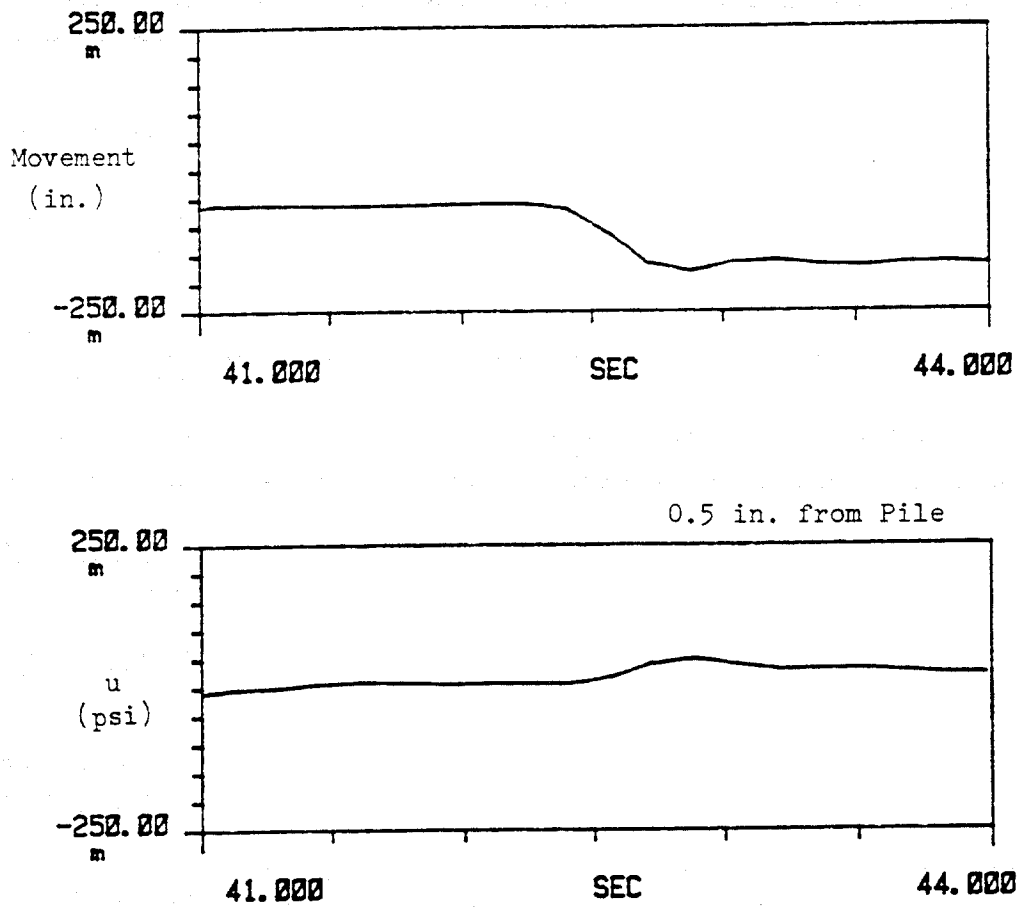

Fig. 6.24. Time History Measurements of Pile Head Movement and Near Field Pore Water Pressure, Test K, [m = milli].

(2) Time history of pore water pressure measurements during the seismic event in two locations, 0.5 in. from the pile wall (near field) and 3.0 in. from pile wall (far field), are shown in Fig. 6.15.

(3) Time history of measurement of pile head movement is shown in Fig. 6.16.

It can be seen that no buildup of pore water pressure took place during the seismic that might have produced loss of pile capacity for the applied bias load.

(b) **Test I2:**

(1) Time history measurements of load at the pile head, pile's mid section and near-toe location during the vertical seismic motion are depicted in Fig. 6.17.

(2) Time history pore water pressure generation for near and far fields are shown in Fig. 6.18.

(3) Pile head movement - time record is shown in Fig. 6.19.

(4) Time window records (between 42 and 45 seconds of simulated event) of near-field pore water pressure and pile head movement are shown in Fig. 6.20, for comparison purposes.

Some comments can be made regarding Test I2. First, failure took place 42.5 seconds after the start of the simulated seismic event, corresponding to the first severe ground displacement peak (Fig. 5.11). Second, the induced pore water pressure was triggered by the pile while being pulled out (existence of a time lag between the initial pile movement and the raise point of pore water pressure in Fig. 6.20). The generation of pore water pressures and/or soil liquefaction due to the vertical seismic motion did not occur. Third, failure appears to have occurred when the bias load (90% of inferred static capacity) plus the dynamic head load produced by the interaction of the vibrating pile and the sprig-mass system became approximately equal to the static capacity of the pile. This behavior was typical in tests in which failure occurred.

(c) **Test K:**

Time history measurements of (1) load on the pile at three different levels, (2) pore water pressures in the soil mass, and (3) pile head movement are given in Figs. 6.21 - 6.23. Time window records of pile-head movement and near-field induced pore water pressure are shown in Fig. 6.24. Similar trends to those in Test I2 were obtained, except that the pile did not lose its capacity during the seismic motion. Slight battering of the pile and, therefore, additional passive pressures acting on the pile, may have prevented the pile from being pulled out, even though some initial movement and pore water pressure were monitored. The pile was considered to have failed for purposes of this study.

Post-Shaking Static Capacities after Simulated Seismic Event

Load-movement curves plotted in the same sequence as occurred during testing (i.e., first, application of bias load, then shaking test, and last, application of post-shaking load to failure, if applicable) are shown for representative tests in Figs. 6.25 - 6.28. These curves have been grouped based upon the blow count, a parameter that indirectly relates the confining pressure and relative density to the pile's static capacity. The load-movement curves are shown in the following groupings:

(a) Tests on SJR sand averaging 6.33 b/in. (Fig. 6.25),
(b) Tests on micro-fine sand averaging 6.0 b/in. (Fig. 6.26),
(c) Tests on SJR sand averaging 4.5 b/in. (Fig. 6.27),
(d) Tests on both sands averaging 6.0 b/in. (Fig. 6.28).

Several observations can be made from the load-movement curves:

(a) Post-shaking static capacities (from dynamic tests) were, in general, near the ultimate static capacities (static tests), indicating no loss of soil capacity during the simulated seismic event.

(b) A greater interaction in the bias load-spring-pile system can be observed on Fig. 6.25 for test using the original time record (predominant frequencies: 1.0 - 2.0 Hz) than the test using scaled time record (predominant frequencies: 8 - 10 Hz).

(c) For similar conditions (type of sand, confining pressure, relative density, blow count), static and post-shaking static capacities in micro-fine sand were slightly lower than those in SJR sand. This observation may be explained by the lower value of interface friction angle of the micro-fine sand (Figs. 4.5 and 4.7)

(d) Stiffer behavior of the SJR sand is evident in Fig. 6.28. Similar behavior was shown in Fig. 6.4.

Dynamic Load Transfer Characteristics

Time histories of dynamic unit load transfer (normalized by the effective horizontal chamber pressure, σ_h') for Test H1 (non-failure situation) and Test I2 (failure situation) are shown in Fig. 6.29 for the upper ("top") and lower ("bottom") halves of the pile. Few definitive time-dependent trends can be observed, mainly due to the random nature of the excitation source (seismic event). In Test I2, a drastic reduction in the load transfer is

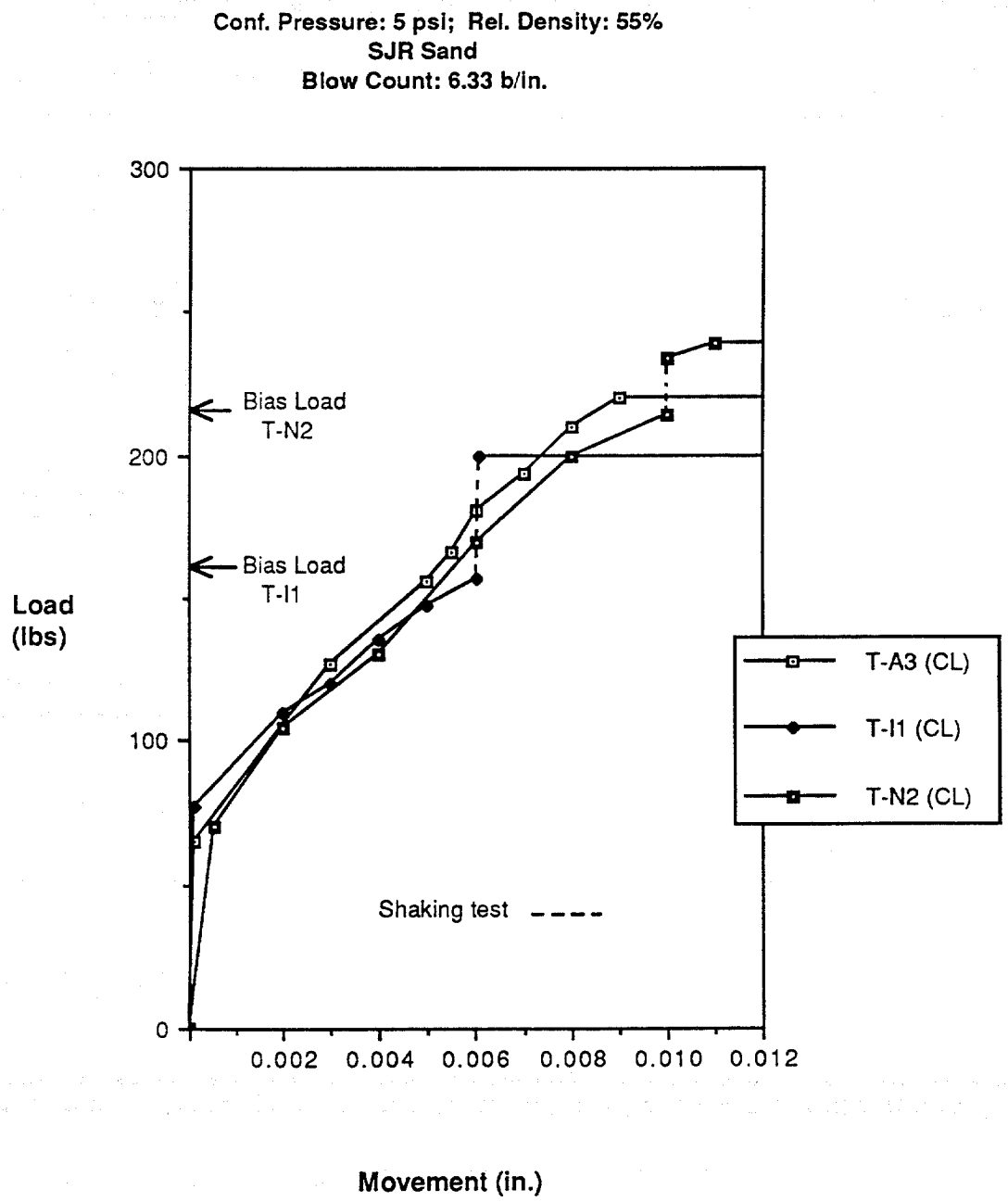

Fig. 6.25. Load-Movement Curves, Tests A3, I1, N2.

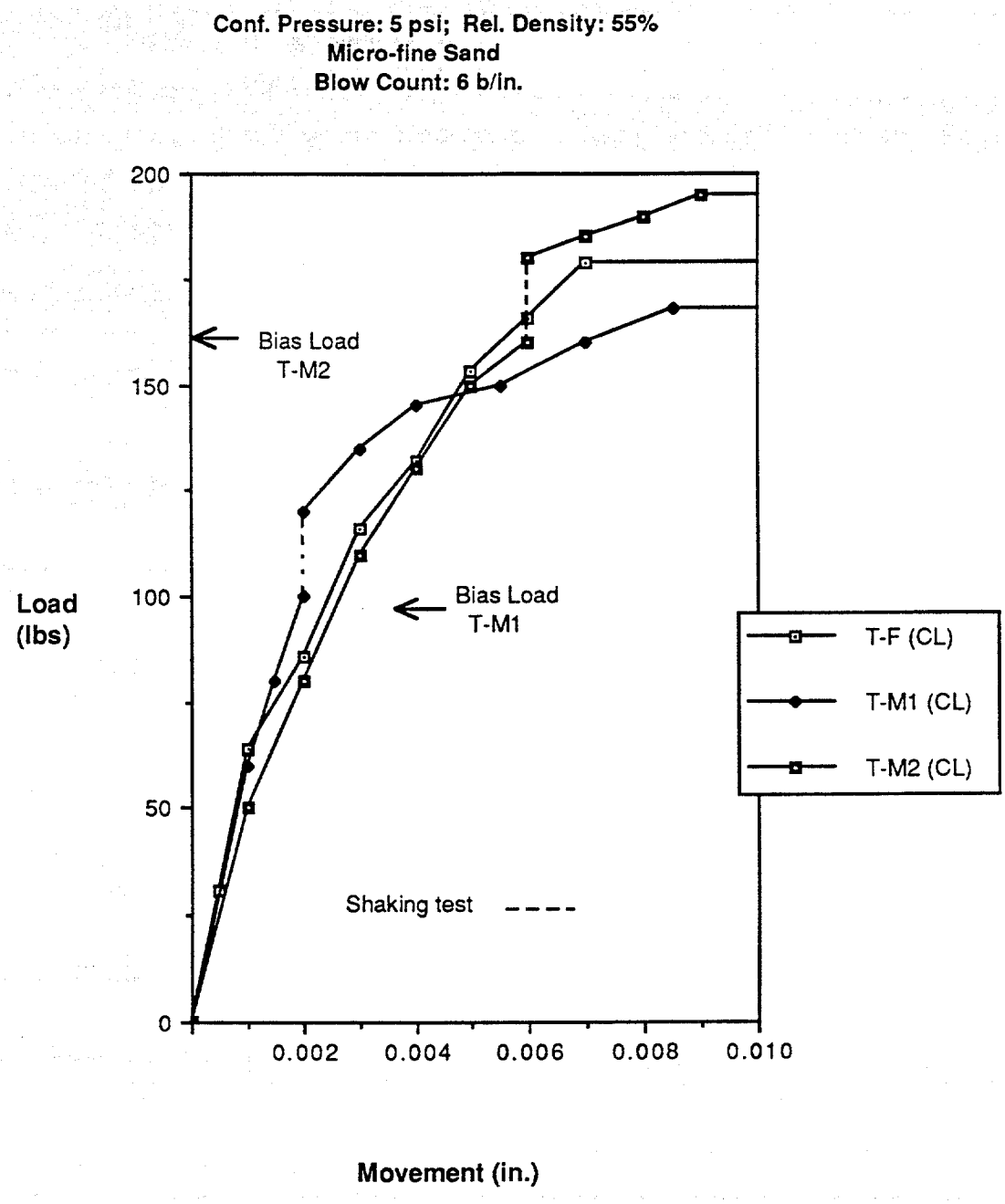

Fig. 6.26. Load-Movement Curves, Tests F, M1, M2.

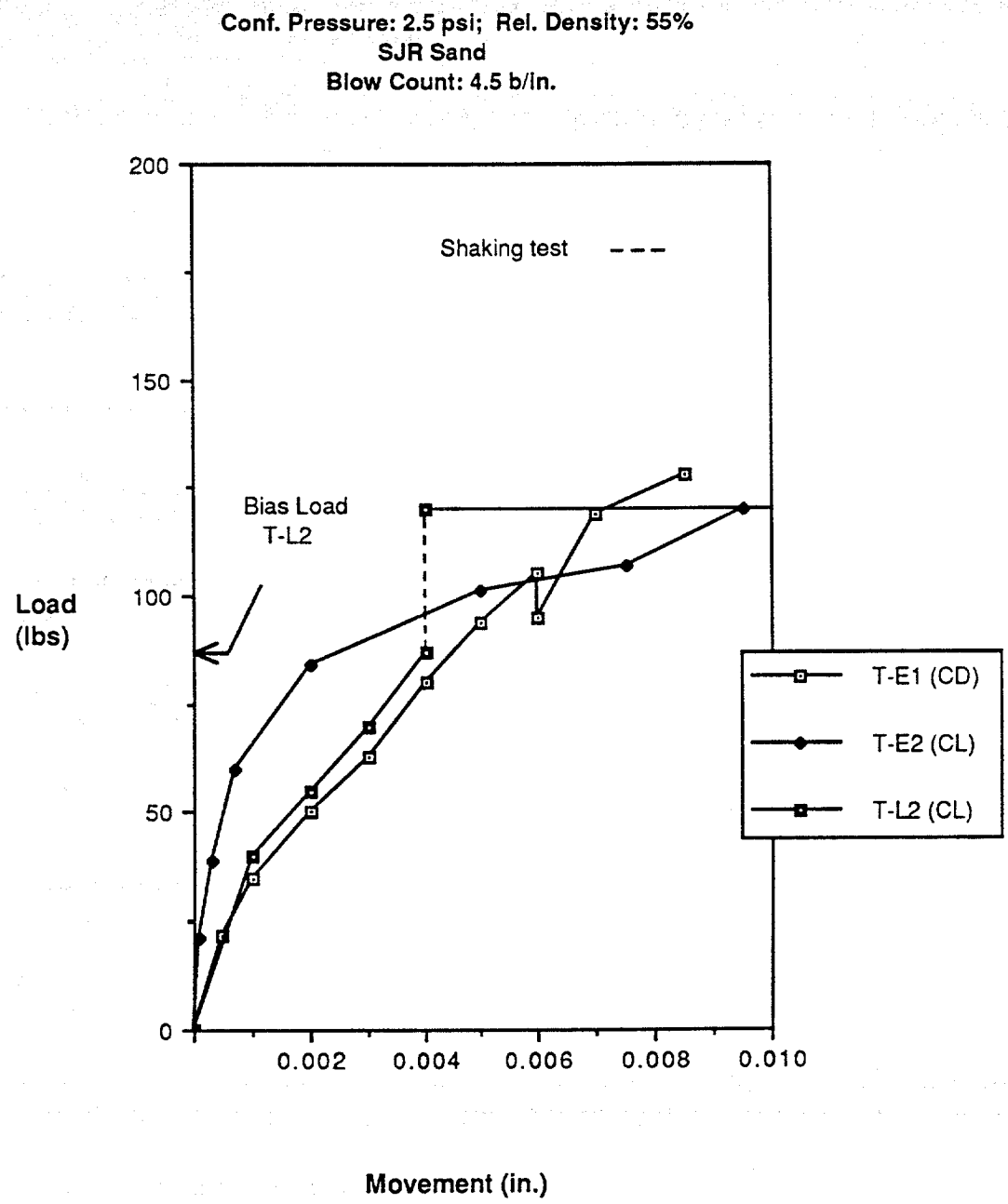

Fig. 6.27. Load-Movement Curves, Tests E1, E2, L2.

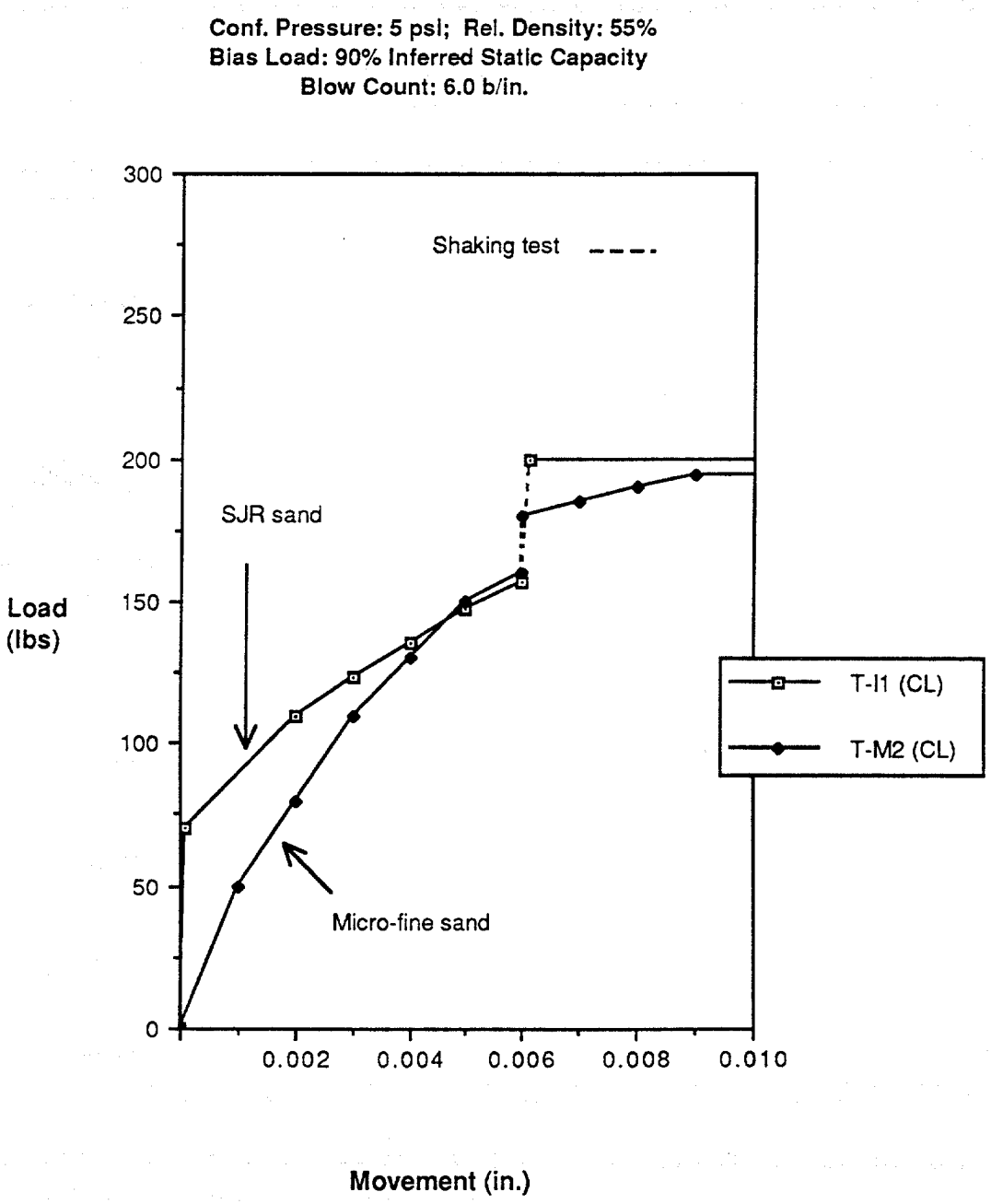

Fig. 6.28. Load-Movement Curves, Tests I1, M2.

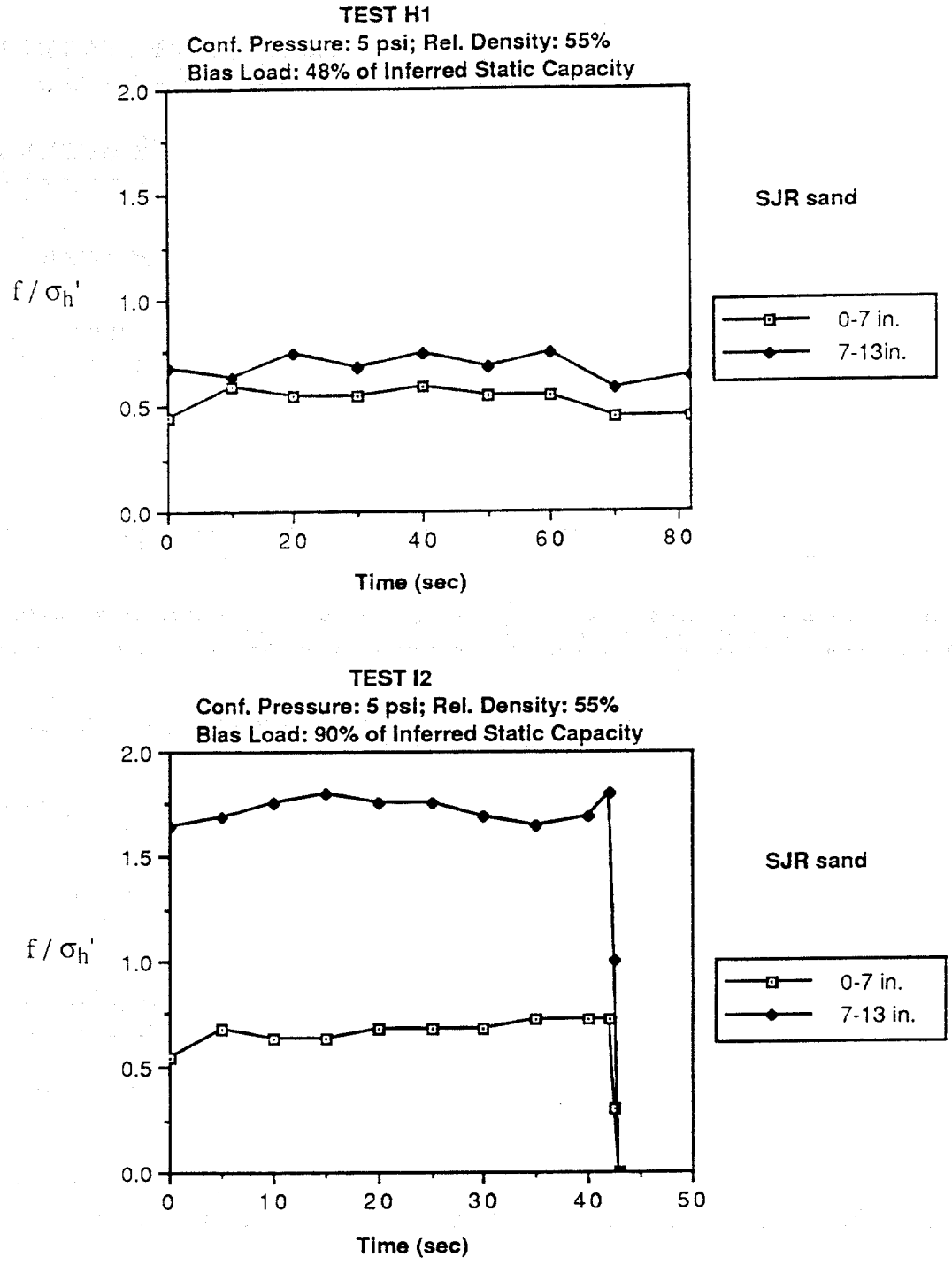

Fig. 6.29. Top and Bottom Time Histories of Normalized Unit Load Transfer, Tests H1 and H2.

observed while the pile is being pulled out by the dynamic interaction of the bias load-spring-pile system excited by the seismic event.

In both tests the normalized load transfer values are similar in the top portion of the pile. In Test H1, in which the bias load corresponds to a possible design condition (factor of safety = 2), the unit load transfer is nearly constant along the pile and with time. In Test I2, in which the bias load is very near the static capacity, the additional load transfer is concentrated in the bottom half of the pile. Failure appeared to be preceded by a slight increase in unit load transfer in the bottom section with no corresponding increase near the surface.

Estimated Strains in Soil Mass Induced by the Simulated Vertical Seismic Motion

An approximated maximum shearing strain in the soil mass, induced by the vertical component of the simulated seismic motion, has been computed based upon the principles of the basic axial wave propagation in a uniform bar. For simplicity, the soil and test chamber were modeled as a column of soil which is excited at one end by a known displacement function and is free at the other end. Complete derivations and computations are given in Appendix G. The magnitude of maximum shearing strain, obtained from two sinusoidal displacement-time functions (estimated from Fig. 5.14) were computed and then added together to obtain an approximated maximum shearing strain in the soil mass. The computed value of shearing strain was in the order of $10^{-4}\%$, a value normally insufficient to induce liquefaction in the free field. This analysis confirms the tests results, since no indication of liquefaction or pore-pressure-induced load transfer reduction were actually observed in the tests.

CHAPTER VII

Conclusions and Recommendations

A laboratory experimental study of tension piles subjected to simulated seismic loading has been conducted in order to asses the magnitude of biased tension load that could be placed upon model piles driven into saturated fine sand. The system was excited in a manner to simulate the vertical component of a seafloor earthquake at a deep soil site. The rationale that dictated the investigation of vertical motion was that the interaction of the vertically excited soil and the pile would induce shearing stresses at the interface of the soil and pile, which along with the stress waves in the soil itself, would produce excess pore water pressures, and perhaps reduction in effective stress at the pile wall due to the grain reorientation in the sand, that would reduce the uplift capacity of the pile and cause the pile to pull out under a biased tension load lower than the static axial capacity.

The phenomenon was studied by selecting a particular seismic event in which acceleration time histories had been measured in the soil at a deep soil site offshore. The event chosen for study was the Oceanside event of July 13, 1986, a Magnitude 5.8 earthquake whose epicenter was 74 km southeast of the instrumentation site. Experience and intuition suggested that peak vertical acceleration of the order of only 3 - 4 milli-g's would not produce any loss of pile capacity. Therefore, the record of the vertical component was scaled upward from Magnitude 5.8 to Magnitude 8.0, resulting in peak vertical accelerations in the range of 70 milli-g's. The scaled acceleration time history was then converted to displacement time history that was used to control the vertical motion of the test chamber into which the model pile was driven.

An Instron testing machine was used to apply the programmed seismic motion to the soil contained in a test chamber, which was 21 in. in height and 20 in. in diameter. The test pile, which was impact driven into pressurized, submerged, fine sand in the chamber, was a steel closed-ended cylinder, 1 in. in diameter and 16 in. long. The pile was instrumented internally with three levels of strain gages to sense axial load distribution. Two applied chamber pressures, 2.5 and 5.0 psi, simulated a range of effective soil stress conditions corresponding to pile penetrations of 20 and 40 ft, respectively. Movement at

the pile head was monitored by a single LVDT. A flexible cable was attached to the head of the pile through which biased tension load was applied by mean of a dead-weight-and-spring-system to simulate the presence of a simple superstructure. The simulated seismic record was applied through the base of the chamber, while the biased tension load was applied simultaneously and continuously by the flexible cable to the head of the pile that protruded from the top of the test chamber. Two miniature pore water pressure transducers were also buried within the chamber to sense the build up of pore water pressure near the wall of the pile and several inches from the pile wall.

A fine, uniform siliceous sand, or San Jacinto River (SJR) sand, was used in most tests to represent the prototype sand. In order to scale the effect of drainage distance (length) and its effects on pore pressure generation and dissipation, both the simulated seismic record (acceleration and/or time axes) and soil permeability were scaled in some tests. A mixture of a very fine sand and finely ground glass beads, termed micro-fine sand, was used as the model sand for the latter purpose. Sand was placed in the test chamber by raining through air at relative densities of 55%, 70%, 78% and 85%.

A number of static controlled load (CL) tests and controlled deformation (CD) tests were conducted to confirm repeatability of uplift capacity, sensitivity of uplift capacity to relative density, confining pressure and failure criteria. A relation between penetration resistance and uplift static capacity was derived to infer the percentile of the static capacity corresponding to the applied bias load in dynamic tests. Dynamic tests were performed under conditions similar to those that existed in static tests by applying the magnitude-scaled or magnitude-and-frequency-scaled displacement time histories for the selected seismic event to the soil while the pile was held under biased uplift load.

Conclusions

The following conclusions have been drawn from this study:

(1) For the earthquake studied, the capacity of the soil to sustain applied uplift loads from a driven displacement pile was not affected by the action of the vertical component of the simulated seismic event. [Computed shearing strains in the soil generated by the vertical motion of the simulated event were insufficient to induce liquefaction in the soil mass.] However, the pile motion produced feedback in the simple mass-spring structure to which

it was attached, which periodically increased the load on the pile during the simulated event.

(2) The pile failed during the simulated event only when the sum of the static biased load and the dynamic load fed back from the mass-spring structure exceeded approximately the static capacity of the pile as determined from controlled force loading. For the parameters studied such failure occurred when the biased static load was approximately 90% of the static uplift capacity.

(3) Scaling of the frequency in the earthquake record and permeability in the soil to provided similitude for a prototype in a sand with the hydraulic conductivity of SJR sand and a pile of 27 inches in diameter did not change the conclusions stated in (1) and (2), above.

(4) By inference from the load transfer data, lateral confining stresses applied by the test chamber were approximately double at the pile-soil interface, mainly due to the insertion of the pile in the soil mass and pile driving effects. If liquefaction or cyclic mobility would have developed, the magnitude of the induced pore water pressures needed to be, at least, twice the applied confining pressure (simulated ambient effective stress in the soil).

(5) Most of the applied load was transferred in the bottom half of the pile. A surface effect apparently existed during uplift loading.

(6) The method of static testing (CD or CL) had a significant influence on the ultimate static capacity of the pile. Controlled-deformation (CD) tests produced higher capacities than those performed under controlled-load (CL) conditions. The CL condition determined to be the appropriate testing condition from which to assess static capacity.

(7) Excess water pressure produced at the soil surface by the induced vertical motion of a mass of water overlying the seafloor was shown to be potentially important in producing shallow liquefaction in the soil deposit, as computed instantaneous pressures for a typical site produced by the scaled earthquake exceeded the effective stresses in the chamber. The interaction of the seafloor and overlying water was not investigated experimentally in this study. However, since the simulated vertical seismic motion did not degrade the soil in the absence of a deep column of water, the phenomenon of seafloor-water interaction can be decoupled from the problem under study here for practical purposes.

Recommendations

The following recommendations are made for future study:

(1) Further research should be oriented to investigate the behavior of piles under a biased uplift load subjected to the horizontal components of the seismic event, and the coupling effects produced by the vertical and horizontal motions should also be investigated.

(2) A study should conducted that is focused on the effects on liquefaction in a soil deposit surrounding a pile induced by the vertical motion of a deep water mass during a seismic event .

REFERENCES

1. Novak, M., and Aboul-Ella, F., "A Computer Program for Calculation of Stiffness and Damping in Layered Media," SACDA, University of Western Ontario, London, Ontario, June, 1979.

2. Roesset, J. M., "Stiffness and Damping Coefficients of Foundations," Dynamic Response of Pile Foundations: Analytical Aspects, Ed. by M. W. O'Neill and R. Dobry, ASCE, October, 1980, pp. 1-30.

3. Dobry, R., and Gazetas, G., "Dynamic Stiffness and Damping of Foundations by Simple methods," Ed. by G. Gazetas and E. Selig, ASCE, October, 1985, pp. 75-109.

4. Nogami, T. and Konagai, K., "Time Domain Axial Response of Dynamically Loaded Single Piles ," Journal of Engineering Mechanics, ASCE, Vol. 112, No. EM11, Nov. 1986, pp. 1241-1252.

5. Foo, S. H. C., Matlock, H., and Meyer, P.L., "Analysis of Driving of Foundation Piles.," Proceedings, Ninth Offshore Technology Conference, Houston, Tx, Vol. II, 1977, pp. 281-290.

6. Blaney, G.W., Muster, G.L.,II, and O'Neill, M.W., "Vertical Vibration Test of a Full-Scale Pile Group," Geotechnical Special Publication No. 11, Ed. by T. Nogami, ASCE, April, 1987, pp. 149-165.

7. Muster, G. L., II, and O'Neill, M.W., "Dynamically Loaded Pile in Overconsolidated Clay," Geotechnical Testing Journal , ASTM, Vol. 9, No. 6, December, 1986, pp. 189-197.

8. Scott, R. F., Tsai, C. F., Steussey, D., and Ting, J. M., "Full-Scale Dynamic Lateral Pile Load Test," Proceedings, Fourteenth Offshore Technology Conference, Houston, Tx, Vol. I, 1982, pp. 435-450.

9. Finn, W.D.L., and Gohl, W.B.,"Centrifuge Model Studies of Piles Under Simulated Earthquake Lateral Loading," Geotechnical Special Publication No. 11, Ed. by T. Nogami, ASCE, April, 1987, pp. 21-38.

10. Poulos, H.G., "Cyclic Degradation of Pile Performance in Calcareous Soils," Analysis and Design of Pile Foundations, Ed. by J.R. Meyer, ASCE, October, 1984, pp. 99-118.

11. Poulos, H.G,"Influence of Cyclic Loading on Axial Pile Response," Proceedings, Second International Conference on Numerical Methods in Offshore Piling, ICE and The University of Texas, Austin, Texas, April, 1982, pp. 419-440.

12. Holmquist, D.V. and Matlock, H., " Resistance-Displacement Relationships for Axially-Loaded Piles in Soft Clay," Proceedings, Eighth Offshore Technology Conference, Vol. 1, Houston, Texas, 1976, pp. 553-570.

13. Karlsrud, K., Nadim, F., and Haugen, T.,"Piles in Clay Under Cyclic Axial Loading: Field Tests and Computational Modelling," Proceedings, Third International Conference on Numerical Methods in Offshore Piling, Institut Francais du Petrole and Laboratorie Central des Ponts et Chausses, Nantes, France, May, 1986, pp. 165-190.

14. Bea, R. G., "Dynamic Response of Piles in Offshore Platforms," Dynamic Response of Pile Foundations: Analytical Aspects, Ed. by M. W. O'Neill and R. Dobry, ASCE, October, 1980, pp. 80-103.

15. Briaud, J.L., and Terry, T. A., "Rate Effect for Vertical and Lateral Pile Response," Proceedings, Third International Conference on Numerical Methods in Offshore Piling, Institut Francais du Petrole and Laboratorie Central des Ponts et Chausses, Nantes, France, May, 1986, pp. 387-405.

16. McAnoy, R.P.L., Cashman, A. C., and Purvis, D.,"Cyclic Tensile Testing of a Pile in Glacial Till," Proceedings, Second International Conference on Numerical Methods in Offshore Piling, ICE and The University of Texas, Austin, Texas, April, 1982, pp. 257-291.

17. Chang, S.F., and Hanna, T. H.,"Repeated Loading on Single Piles in Sand," Journal of the Geotechnical Engineering Division, ASCE, 1980, Vol 106, No. GT2, pp. 171-188.

18. Poulos, H.G., "Some Aspects of Skin Friction of Piles in Clay under Cyclic Loading, " Geotechnical Engineering, Vol. 12, No. 1, 1981, pp. 1-17.

19. Seed, H.B., "Evaluation of Soil Liquefaction Effects on Level Ground During Earthquakes," Liquefaction Problems in Geotechnical Engineering, ASCE National Convention, September, 1976, pp. 1-104.

20. Castro, G., and Poulos, J., "Factors Affecting Liquefaction and Cyclic Mobility," Liquefaction Problems in Geotechnical Engineering, ASCE National Convention, September, 1976, pp. 105-138.

21. Finn, W.D.L.,"Soil Liquefaction: Recent Developments in Practice," Proceedings, Second International Conference on Soil Dynamics and Earthquake Engineering, ASCE, June, 1985, pp. 1-43.

22. Seed, H.B., and Wilson, S.D., "The Turnagain Heights Landslide in Anchorage, Alaska, " Journal of the Soil Mechanics and Foundation Division, ASCE, Vol. 93 No. SM4, July, 1967, pp. 325-353.

23. Seed, H.B. and Idriss, I.M., "Analysis of Soil Liquefaction: Niigita Earthquake, "Journal of the Soil Mechanics and Foundation Division, ASCE, Vol. 93, No. SM3, May, 1967, pp. 83-108.

24. Castro, G., "Liquefaction of Sands," Harvard Soil Mechanics Series, No. 81, Harvard University, Cambridge, Mass., January, 1969.

25. Seed, H.B. and Peacock, W.H.,"Applicability of Laboratory Test Procedures for Measuring Soil Liquefaction Characteristics under Cyclic Loading," Earthquake Engineering Research Center, Report No. EERC 70-8, November, 1970.

26. Casagrande, A., "Liquefaction and Cyclic Deformation of Sands, A critical Review," Proceedings, Fifth Panamerican Conference on Soil Mechanics and Foundation Engineering, Buenos Aires, Argentina, Nov., 1975, Harvard Soil Mechanics Series No. 88.

27. Lee, K.L., and Seed, H.B.,"Cyclic Stress Conditions Causing Liquefaction of Sand," Journal of the Soil Mechanics and Foundation Division, ASCE, Vol. 93, SM1, Jan., 1967, pp. 47-70.

28. De Alba, P., "Group Effects on Piles in a Liquefying Sand Deposit," Geotechnical Practice in Offshore Engineering, ASCE, Ed. by S.G. Wright, April, 1983, pp. 300-314.

29. Bradshaw, H., Barton, R.R., and McKenzie, R.H., "The Hutton TLP Foundation Design," Proceedings, Sixteen Offshore Technology Conference, Vol. 3, Houston, Texas, 1984, pp. 263-273.

30. Takashi, T., Shimizu, K., and Wakahara, T., " Seismic Observations and Analysis of Grouped Piles," Geotechnical Special Publication No. 11, Ed. By T. Nogami, ASCE, April, 1987, pp. 1-20.

31. Seed, H.B., and Idriss, I.M., " Influence of Soil Conditions on Ground Motions During Earthquakes," Journal of the Soil Mechanics and Foundation Division, ASCE, Vol. 95, No. SM1, January, 1969, pp. 99-137.

32. Schnabel, P.B., Lysmer, J., and Seed, H.B.,"SHAKE - A Computer Program for Earthquake Response Analysis of Horizontally Layered Sites," Report No. EERC 72-12, Earthquake Engineering Research Center, 1972.

33. Seed, H.B., and Idriss, I. M., "Simplified Procedure for Evaluating Soil Liquefaction Potential," Journal of the Soil Mechanics and Foundations Division, ASCE, Vol. 97, No. SM9, September, 1971, pp. 1249-1273.

34. Martin, P.P., and Seed, H.B., "APOLLO, A Computer Program for the Analysis of Pore Pressure Generation and Dissipation in Horizontal Sand Layers During Cyclic or Earthquake Loading," Report No. EERC 78-21, Earthquake Engineering Research Center, 1978.

35. Vanzini, R., Rossetto, P., Ferro, G., and Manfredini, G.M., "Non-Linear Seismic Response Analysis of an Offshore Platform on Liquefiable Soil," Proceedings,Vol. 3, 20th Offshore Technology Conference, Houston, Texas, May, 1988, pp. 159-169.

36. Annual Book of ASTM Standards, American Society for Testing and Materials, Soil and Rock/Building Stones, Vol. 04.08, 1988, pp. 554-572.

37. Sleefe, G.E., and Engi, D., "Seafloor Response for Two Southern California Earthquakes," Proceedings, 1987 SEM Spring Conference on Experimental Mechanics, Houston, Texas, pp. 747-753.

38. Seed, H.B., Idriss, I.M., and Kiefer, F.W., "Characteristics of Rock Motions During Earthquakes," Journal of Soil Mechanics and Foundation Division, ASCE, Vol. 95, No. SM5, Sept., 1969, pp. 1199-1218.

39. Cooley, J.W., and Tukey, J.W., "An Algorithm for Machine Calculation of Complex Fourier Series," Mathematical Computation, Vol. 19, 1965, pp. 297-301.

40. Chakrabarti, S., Shaw, D., Stephenson, D.E., and Wijaya-Kumar, B.V.K, "Digital Signal Processing of Geotechnical Data," Journal of Engineering Mechanics Division, ASCE, Vol. 112, January, 1986, pp. 70-84.

41. Trifunac, M.D., "Preliminary Empirical Model for Scaling Fourier Amplitude Spectra of Strong Acceleration in Terms of Modified Mercalli Intensity and Recording Site Conditions," Earthquake Engineering and Structural Dynamics, Vol. 7, 1979, pp. 63-74.

42. Quick Report on CSMIP Strong-Motion Records from the October 17, 1989 Earthquake in Santa Cruz Mountain (Loma Prieta Earthquake), California Strong Motion Instrumentation Program, October 19, 1989

43. Fuglsang, L.D., and Ovesen, N.K., "The application of the Theory of Modelling to Centrifuge Studies," Centrifuge in Soil Mechanics, Editors W.H. Craig, R.G. James and A.N. Schofield, A. A. Balkema Publishers, Rotterdam, 1988, p. 131.

44. Williams, A.N., and Mau, S.T., "Earthquake Response of Submerged Circular Arch," Journal of Waterways, Ports, Coastal, and Ocean Engineering, ASCE, Vol. 114, No. 4, July, 1988, p.410.

45. Vesic, A.S., "Expansion of Cavities in Infinite Soil Mass," Journal of Soil Mechanics and Foundation Division, ASCE, Vol. 98, No. SM3, March, 1972, pp. 265-290.

APPENDIX A

General Soil Log at SEMS Unit Site

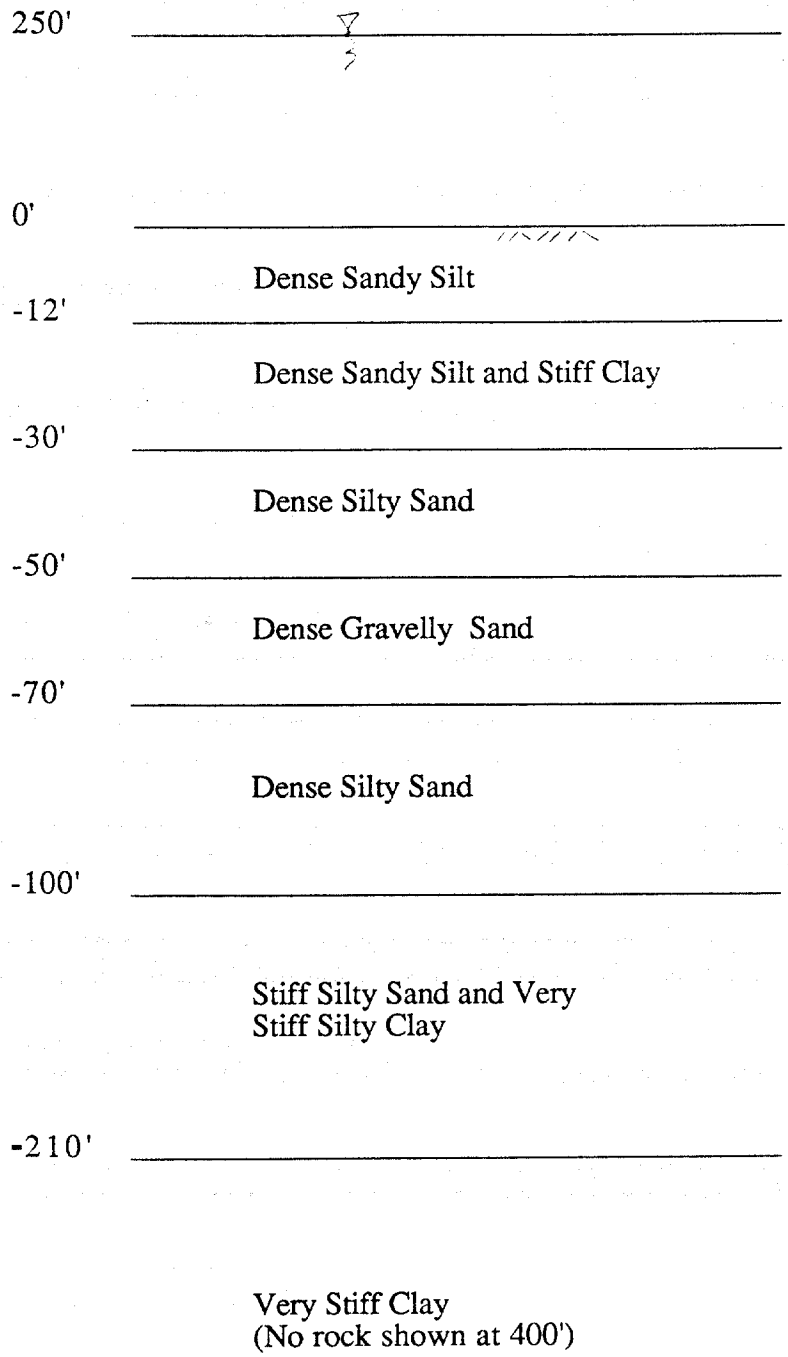

Appendix B

Calibration Equations

Fig. B.1. Strain Gage Calibration Equations

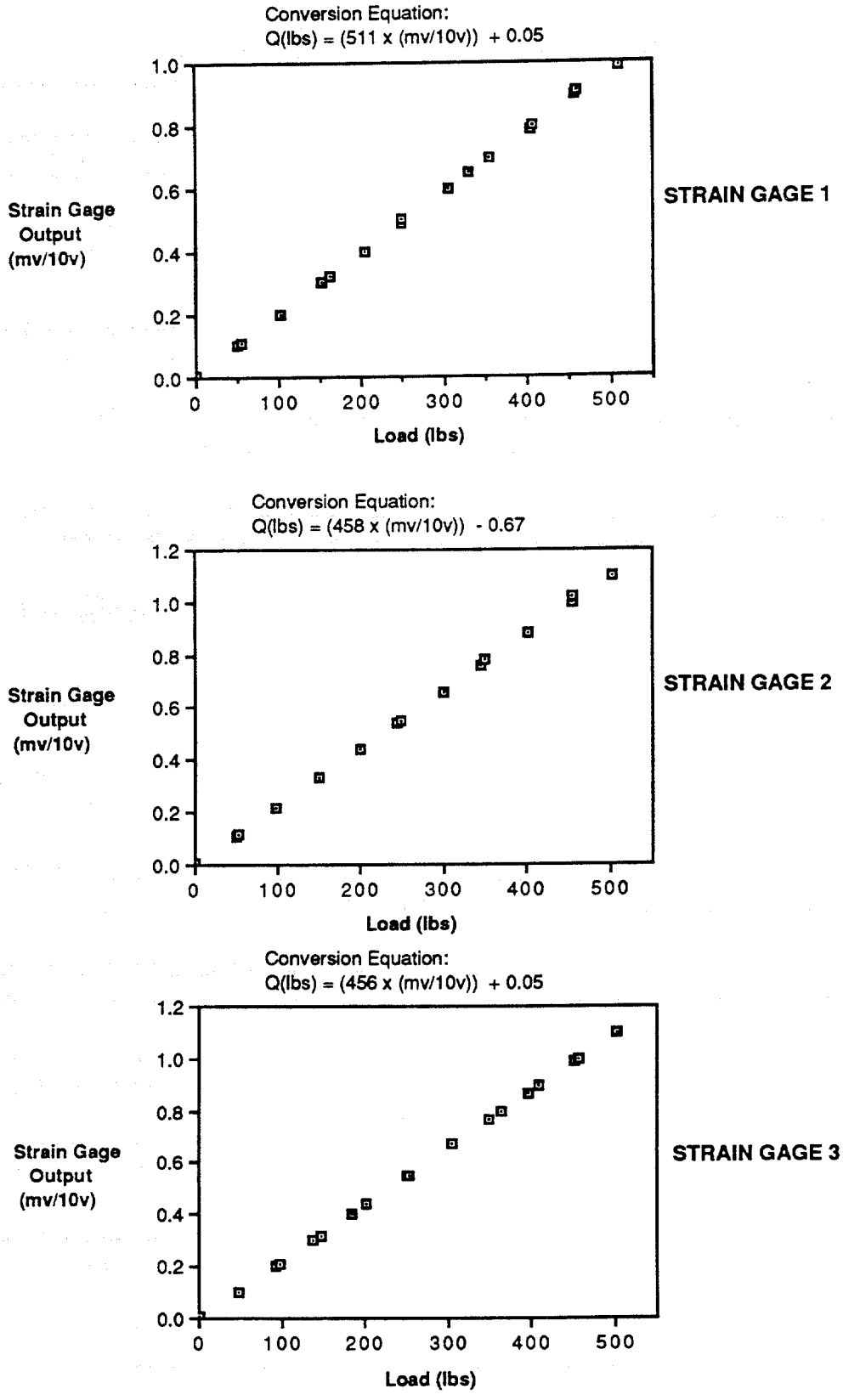

Table B.1. Pore Water Pressure Transducer (PDCR 81) Calibration Equation

Transducer Serial No.	Calibration Equation
4254	p (psi) = 0.1484 x (mv/10v)
3336	p (psi) = 0.131 x (mv/10v)

Table B.2. Test Chamber Calibration

Applied Pressure at Contol Panel (psi)	Measured Pressure at Pressure Cell (psi)	
	Sensotec 124296	Sensotec 124297
0	0.1	0.05
6	5.0	6.0
10	9.0	10.0
15	13.8	14.8
20	18.5	19.5
25	22.5	24.0
30	28.0	29.0

APPENDIX C

Model to Prototype Similitude

A. Scaling Length:

$$(\sigma_o'_{av} / \gamma' L_{50})_{model} = (\sigma_o'_{av} / \gamma' L_{50})_{prototype} \quad \text{(soil completely submerged)} \quad \text{(C.1)}$$

where

$\sigma_o'_{av}$ = Mean effective stress along length of pile,

γ' = Bouyant unit weight of soil,

L_{50} = One-half length of pile (distance from soil surface to center of embedded portion of pile).

Let

a. L_{50p} = 20 feet (modelling a 40-foot-long pile or top 40 feet of a longer pile, approximately),

b. γ'_p = 55 pcf, and

c. OCR_p = 1.5 (average to depth of 40 feet; i.e., at z = 20 feet for uniform soil) from which

$$K_{op} = (1 - \sin \phi') \, OCR^{\sin \phi'}. \quad \text{(C.2)}$$

Considering SJR sand as the prototype sand, $\phi' = 39^o$ at Dr = 55% (letting $Dr_m = Dr_p$), then

$$K_{op} = (0.371)(1.290) = 0.48, \quad \text{and}$$

$$(\sigma_o'_{av})_p = 20(\gamma')((1+ 2K_{op})/ 3) = 719 \text{ psf} = 5.0 \text{ psi}.$$

Now, if $(\sigma_o'_{av})_m = (\sigma_o'_{av})_p$, then from Eq. C.1.,

$$(\gamma' L_{50})_{model} = (\gamma' L_{50})_{prototype} = 55 \, (20) = 1100 \text{ psf}.$$

In the test chamber $L_{50m} = 0.67$ feet (8 in.), so that the apparent effective unit weight of the soil chamber is:

$$\gamma'_m = 1100 / 0.67 = 1642 \text{ pcf.}$$

The actual unit weight (bouyant) is $\gamma'_a = 60$ pcf (approximately).

This means that the equivalent g-value (g value for similar test conditions had test been conducted in a centrifuge) is

$$g = 1642 / 60 = 27.4$$

Thus, according to centrifuge scaling rules, pile diameter is scaled by a factor of 27.4, in terms of effective stress similitude (27.4-in diameter, 40-feet long).

B. Scaling Pore Water Pressure Dissipation (Static Analogy)

From consolidation theory

$$(kt / H^2)_{model} = (kt / H^2)_{prototype} , \qquad (C.3)$$

where

H = drainage distance.

According to length scaling rules

$$H_{model} = (1 / N) H_{prototype} \qquad (C.4)$$

where

N = the length-scaling factor for pore water dissipation,

thus, according to Eqs. C.3 and C.4,

$$(kt)_{model} = (1/N^2) (kt)_{prototype.}$$

Let

$t_{model} = 1/7\ t_{prototype}$ (for the earthquake modelled, this value represents the best capabilities of the Instron machine), and

letter SJR sand represent the prototype sand and using micro-fine sand as model sand,

$k_{prototype} = 1.0 \times 10^{-2}$ cm/sec,

$k_{model} = 1.21 \times 10^{-3}$ cm/sec,

so that

$1.21 \times 10^{-3}\ (1/7)\ t_{prototype} = (\ 1/N^2\ )(1.0 \times 10^{-2})\ t_{prototype}$, or

$N^2 = (1.0 \times 10^{-2} / 1.73 \times 10^{-4}) = 57.8$, or

$N = 7.60 < 27.4$ (length scale factor).

If, on the other hand, $k_{prototype}$ is increased such that

$k_{prototype} = 1.3 \times 10^{-1}$ cm/sec, then

$N^2 = (1.3 \times 10^{-1} / 1.73 \times 10^{-4}) = 750$, or

$N = 27.4$

Micro-fine sand is the finest material available that will act like sand in its frictional properties, so that

$(\ kt\ )_{model} = 1.73 \times 10^{-4}\ t_{prototype}$

is a practical lower limit for the testing system. Since $(d_{10})_{model}$ (micro-fine sand) = 0.060 mm, then $(d_{10})_{prototype} = 27.4\ (0.060) = 1.61$ mm (medium sand).

APPENDIX D

Induced Pressure due to Vertical Water Mass Excitation

The total pressure at any particular point in the water mass for the system depicted in Fig. 5.13, and subjected to a vertical seafloor excitation, can be evaluated by adding the effects of the hydrodynamic pressure field (induced water pressure) generated by the water mass vertical motion, to the existing hydrostatic pressure field. Therefore, the total pressure can be expressed as follows:

$$p = \rho\frac{\partial\phi}{\partial t} + \rho g z \ , \tag{D.1}$$

where

p = Total fluid pressure at distance z from seafloor,
ρ = Fluid density,
ϕ = Fluid velocity potential,
z = Distance above seafloor, and
g = Acceleration due to gravity.

The fluid velocity potential function is given by:

$$\phi\,(z,t) = \Phi\,(z)\, e^{i\Omega t} \ , \tag{D.2}$$

in which

Φ = Fluid velocity potential amplitude,
Ω = Displacement excitation frequency,
t = time,
e = exponential, and
$i = \sqrt{-1}$.

Thus

$$\frac{\partial\phi}{\partial t} = i\Omega\Phi e^{i\Omega t} \ . \tag{D.3}$$

The simulated displacement excitation function (w) can be expressed as follows:

$$w = We^{i\Omega t} \ . \tag{D.4}$$

Thus

$$\frac{\partial w}{\partial t} = i\Omega We^{i\Omega t} \tag{D.5}$$

where

W = Displacement amplitude.

The evaluation of the second term in Eq. D.1 is immediate. For the first term, the governing equation for the fluid is as follows:

$$\frac{\partial^2 \Phi(z)}{\partial z^2} + k^2 \Phi(z) = 0 \ , \tag{D.6}$$

where

$$k = \Omega / c \ , \tag{D.7}$$

in which

Ω = Displacement excitation frequency,
c = Acoustic speed in water = 1430 m/sec.

The boundary conditions on $\Phi(z)$ are as follows:

$$\frac{\partial \Phi}{\partial z} = \frac{\partial w}{\partial t} = i\Omega We^{i\Omega t} \ , \quad \text{on } z = 0, \text{ and} \tag{D.8}$$

$$\Phi = 0, \ z = h \ \text{(free surface condition with no waves).} \tag{D.9}$$

A suitable form for Φ has been given by Williams and Mau (43) as:

$$\Phi(z) = \frac{i\Omega W}{k} \frac{\sin k(z-h)}{\cos kh} \ , \quad z \angle h \ . \tag{D.10}$$

Thus, Eq. D.3 becomes

$$\frac{\partial \phi}{\partial t} = \frac{\Omega^2 W}{k} \frac{\sin k(z-h)}{\cos kh} e^{i\Omega t} \quad . \tag{D.11}$$

For $z = 0$,

$$\frac{\partial \phi}{\partial t} = \frac{\Omega^2 W}{k} \tan (kh)\, e^{i\Omega t} \quad . \tag{D.12}$$

Let

$c = 1430$ m/sec $= 4691.8$ ft/sec,
$h = 1000$ feet,
$\rho = \gamma / g = 1.93$ lb-sec^2 / ft^4 .

For

(a) Low-frequency high-amplitude signal (Fig. 5.14):

$\Omega = 0.12$ Hz $= 0.766$ rad/sec,
$k = 0.766 / 4691.8 = 0.000163$ rad/ft,
$W = 0.73$ in. $= 0.0608$ ft,

thus, $\rho\, (\partial\phi/\partial t)_{max}$ is computed as 69.49 psf (0.48 psi).

(b) High-frequency low-amplitude signal (Fig. 5.14):

$\Omega = 1$ Hz $= 6.28$ rad/sec,
$k = 6.28 / 4691.8 = 0.00133$ rad/ft,
$W = 0.05$ in. $= 0.0041$ ft,

thus, $\rho\, (\partial\phi/\partial t)_{max}$ is computed as 955 psf (6.63 psi).

The total excess soil surface pressure generated by the two signals of the vertical component of motion is, therefore, 7. 11 psi.

Appendix E

Load-Depth Relationships

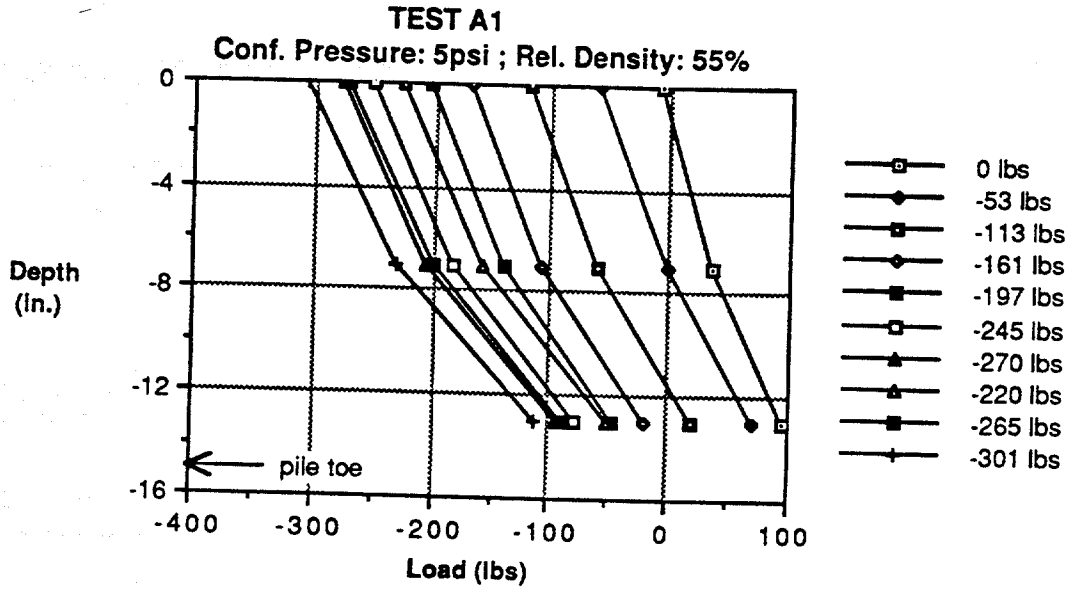

Fig. E.1. Load-Depth Relationships, Test A1.

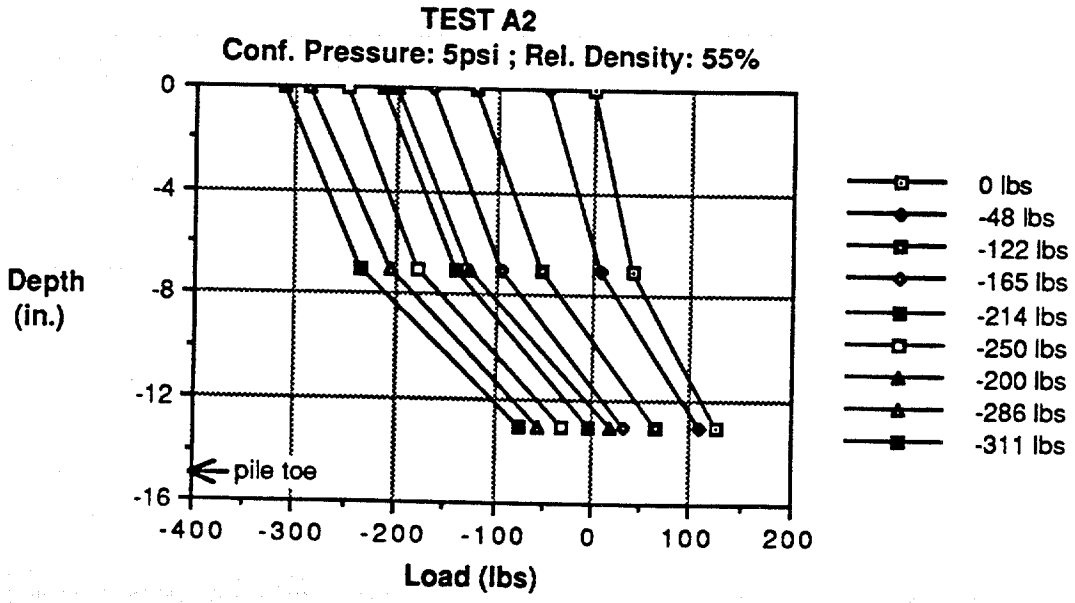

Fig. E.2. Load-Depth Relationships, Test A2.

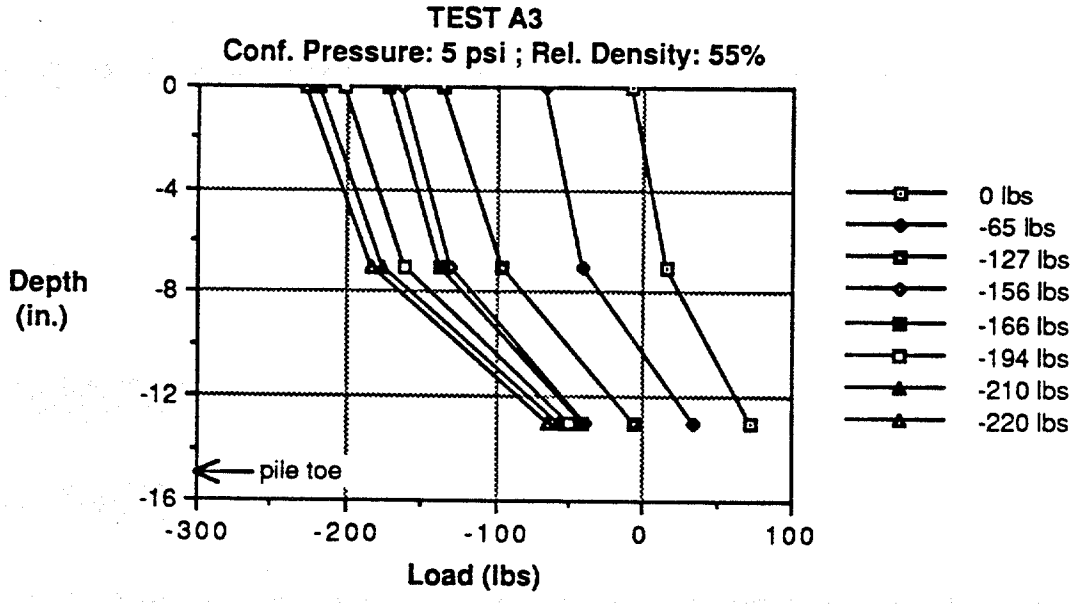

Fig. E.3. Load-Depth Relationships, Test A3.

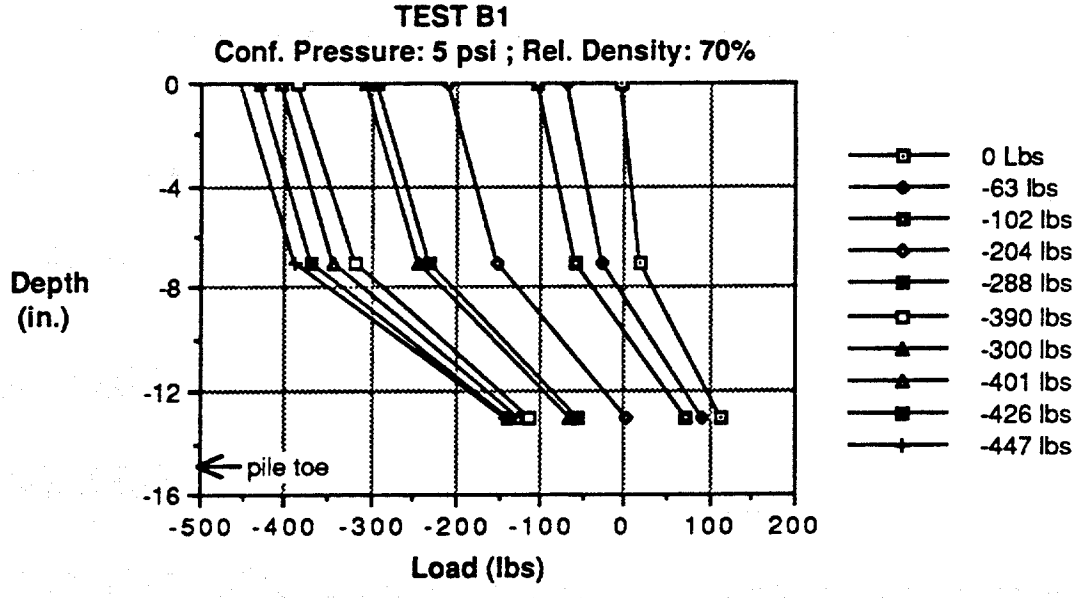

Fig. E.4. Load-Depth Relationships, Test B1.

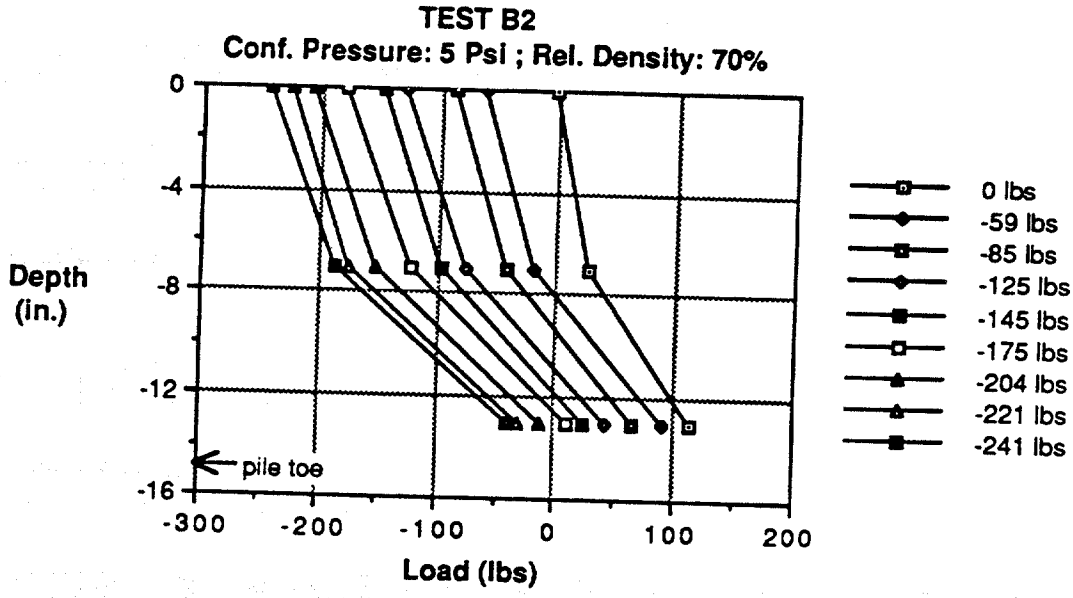

Fig. E.5. Load-Depth Relationships, Test B2.

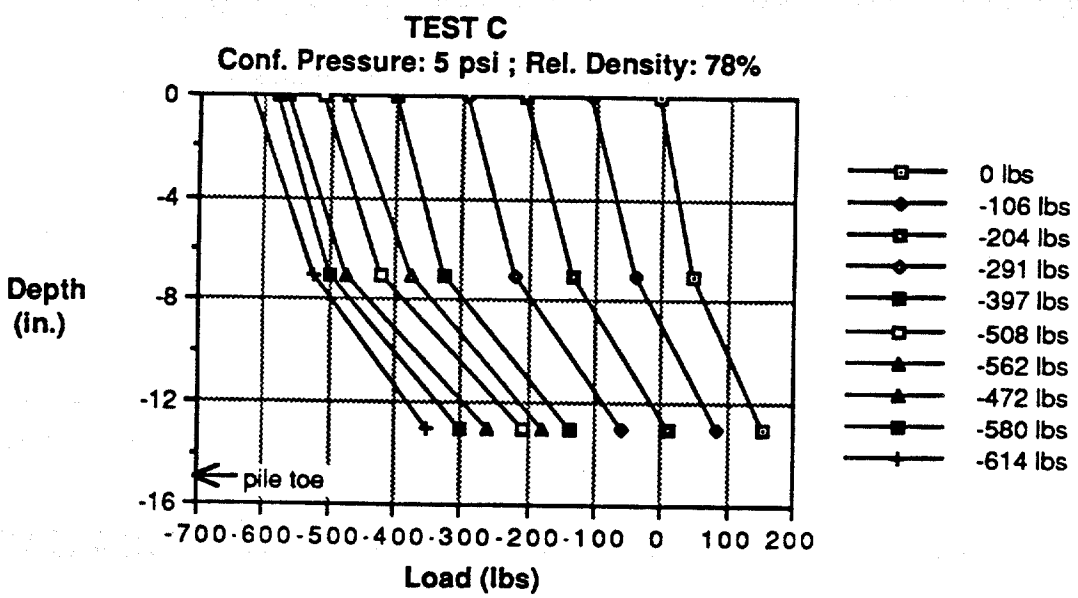

Fig. E.6. Load-Depth Relationships, Test C.

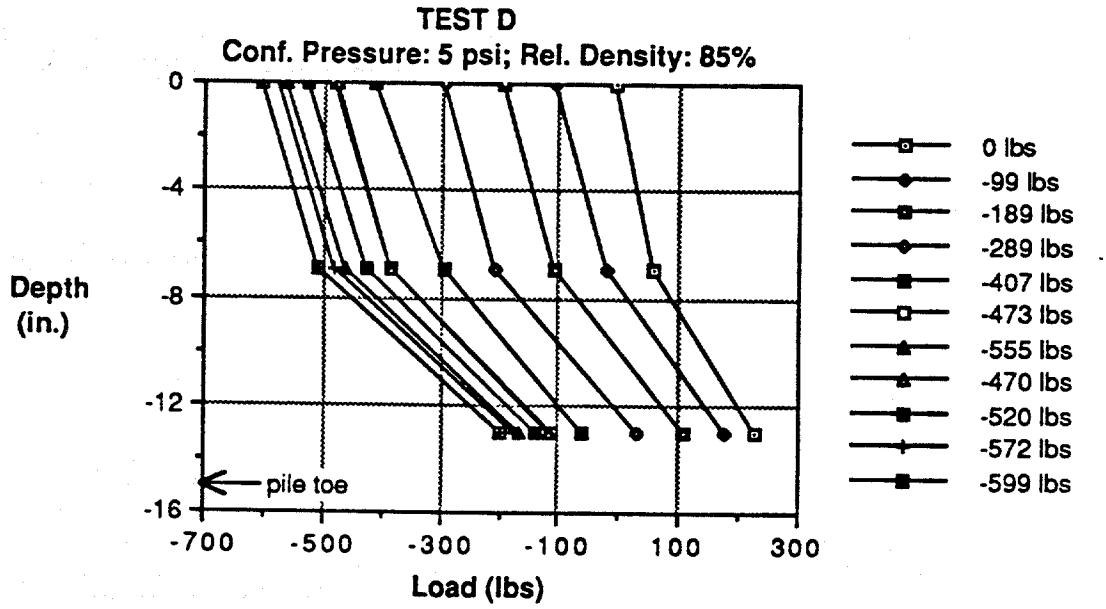

Fig. E.7. Load-Depth Relationships, Test D.

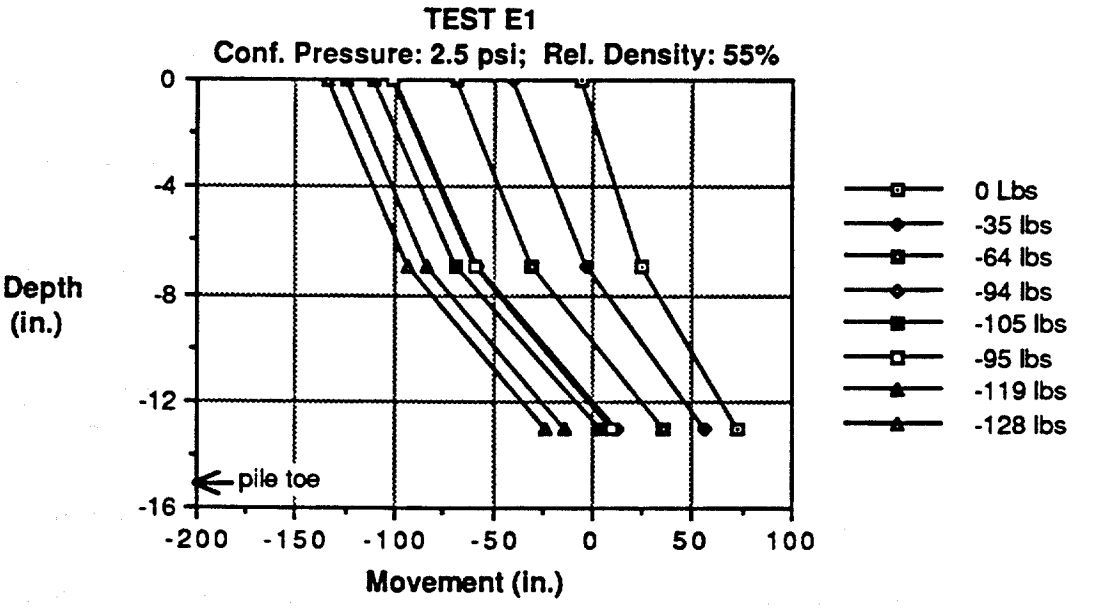

Fig. E.8. Load-Depth Relationships, Test E1.

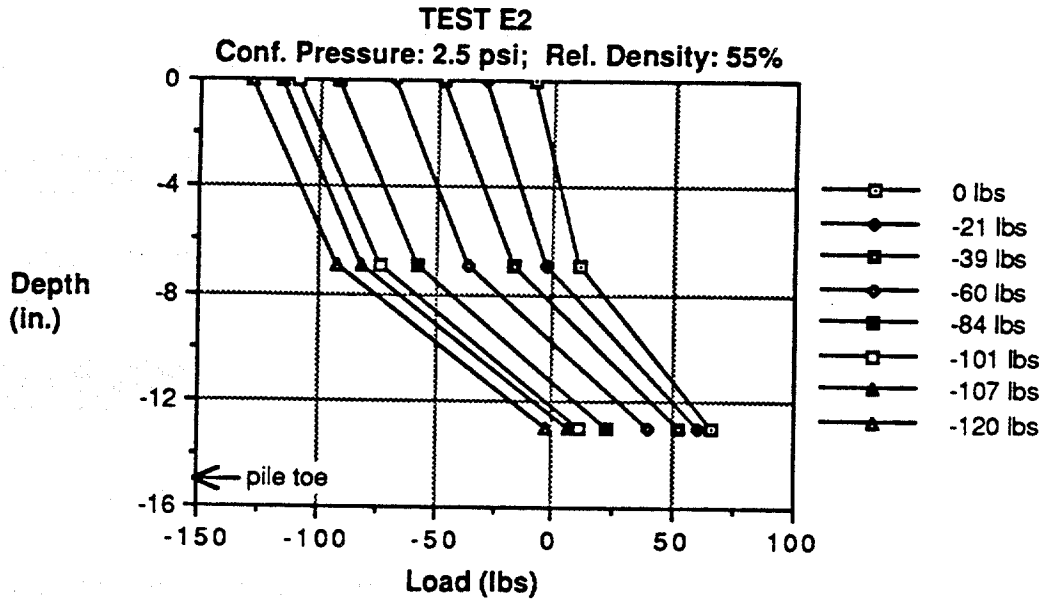

Fig. E.9. Load-Depth Relationships, Test E2.

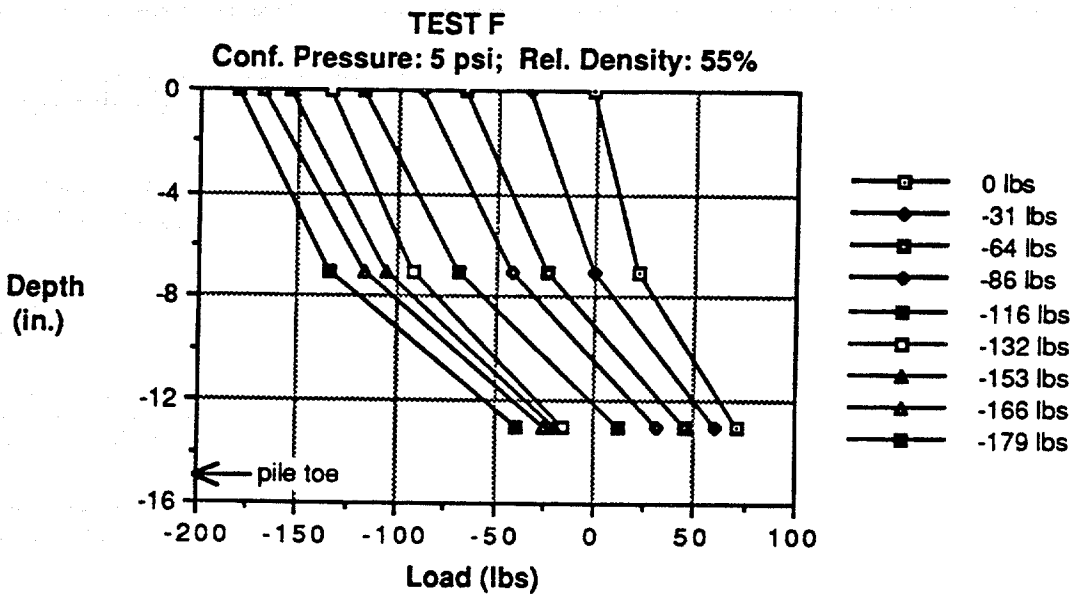

Fig. E.10. Load-Depth Relationships, Test F.

Appendix F

Time History Measurements During Dynamic Tests

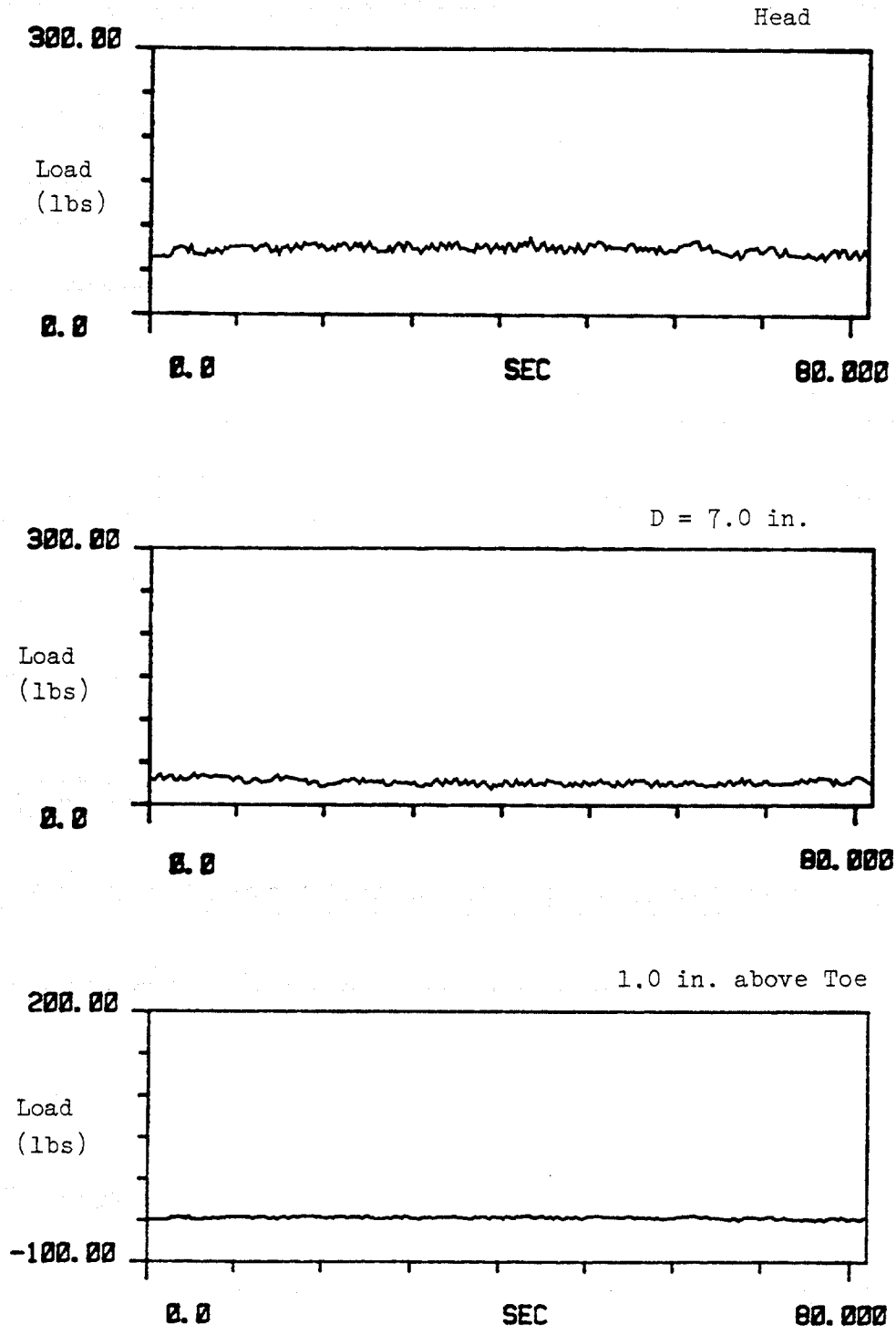

Fig. F.1. Time History Measurements of Dynamic Load on Pile, Test G.

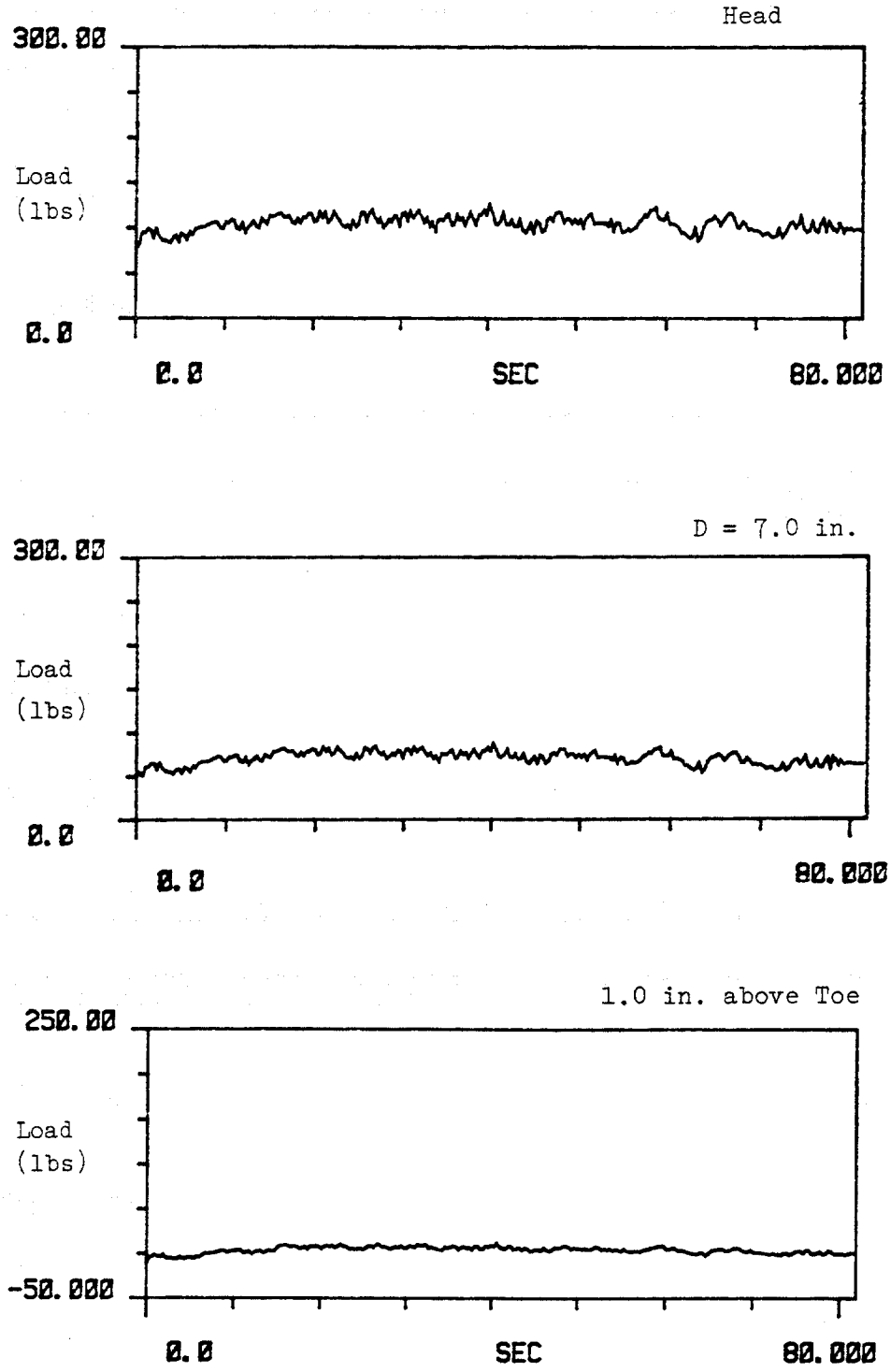

Fig. F.4. Time History Measurements of Dynamic Load on Pile, Test H2.

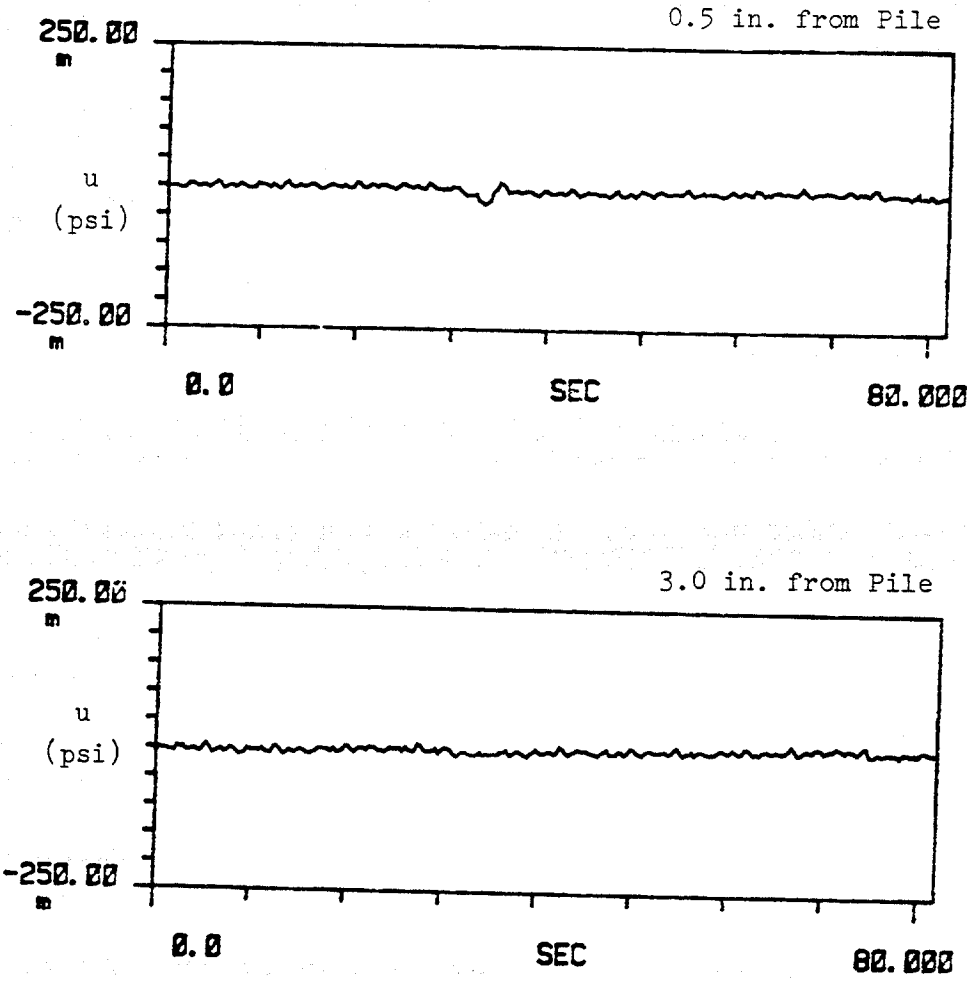

Fig. F.5. Time History Measurements of Near and Far Field Pore Water Pressures, Test H2, [m = milli].

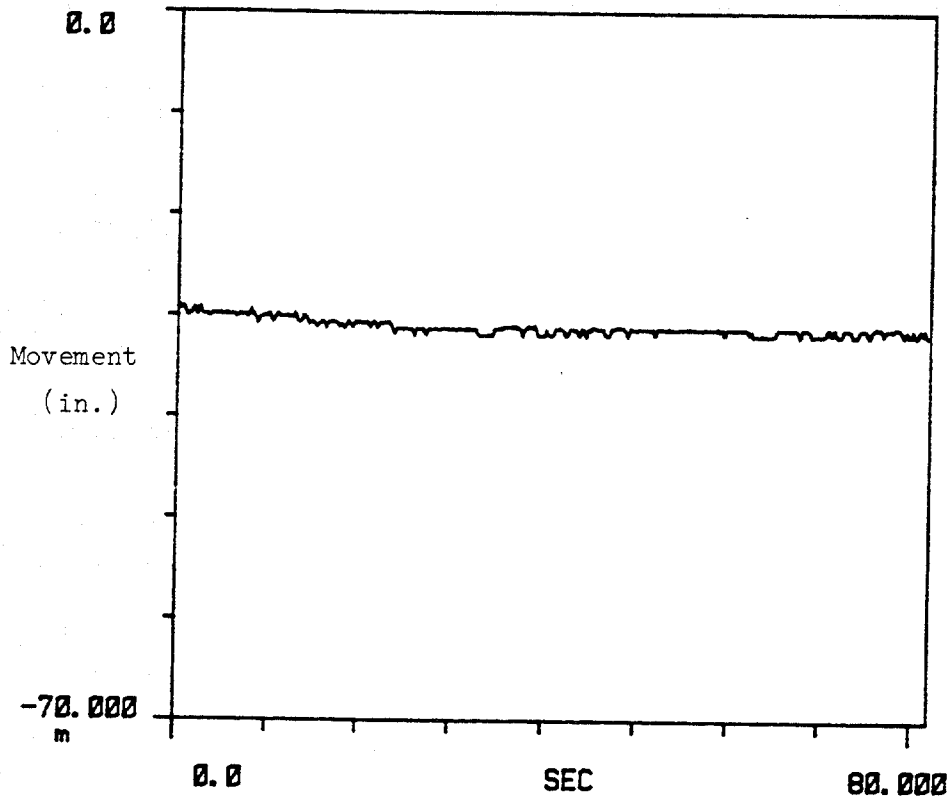

Fig. F.6. Time History Measurements of Pile Head Movement, Test H2, [m = milli].

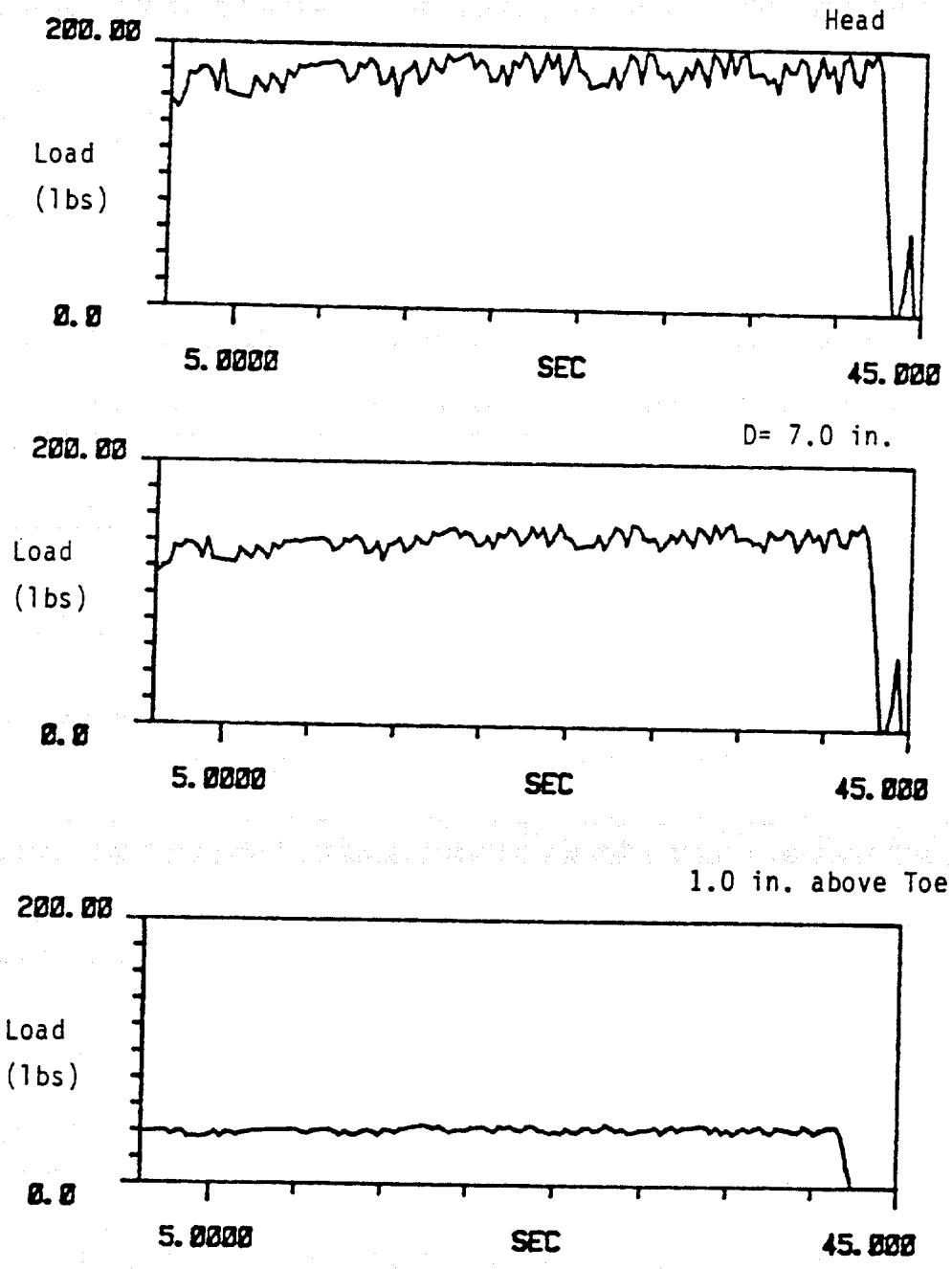

Fig. F.7. Time History Measurements of Dynamic Load on Pile, Test I1.

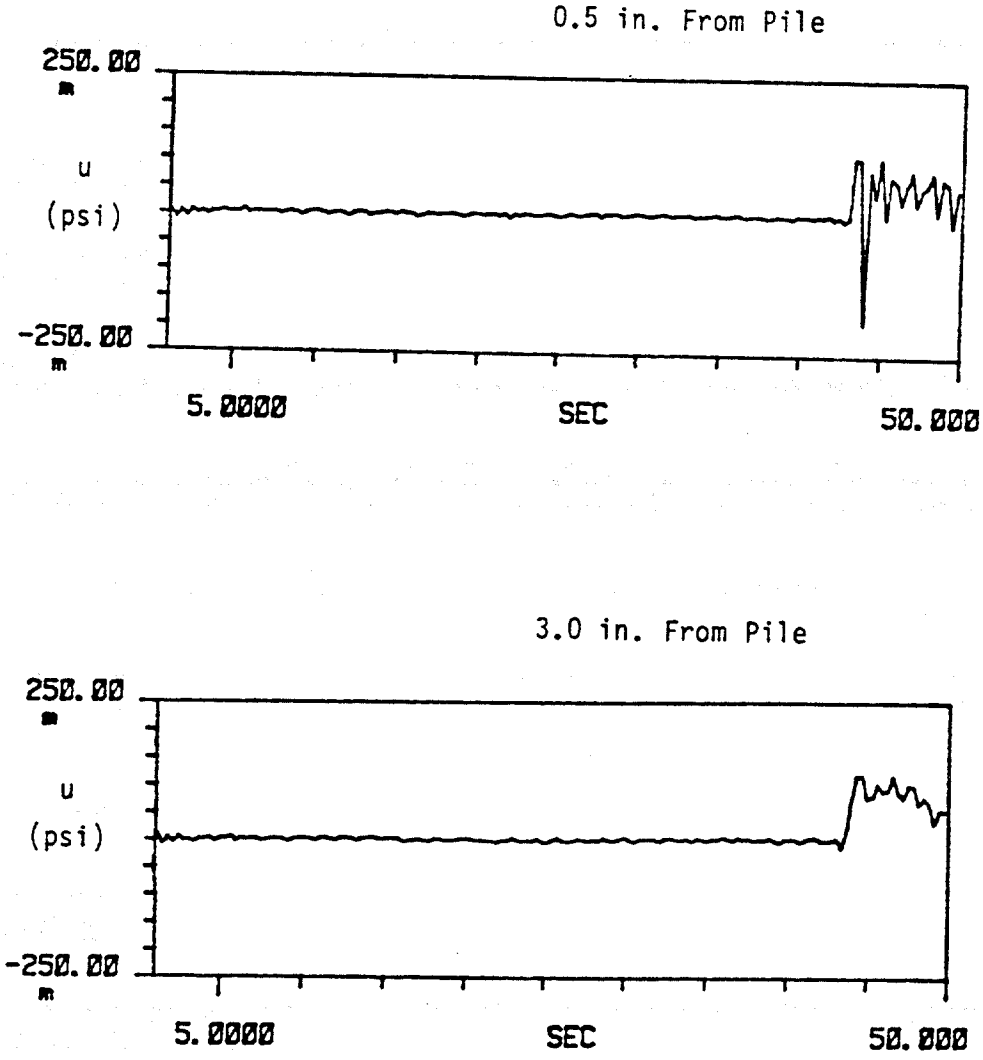

Fig. F.8. Time History Measurements of Near and Far Field Pore Water Pressures, Test I1, [m = milli].

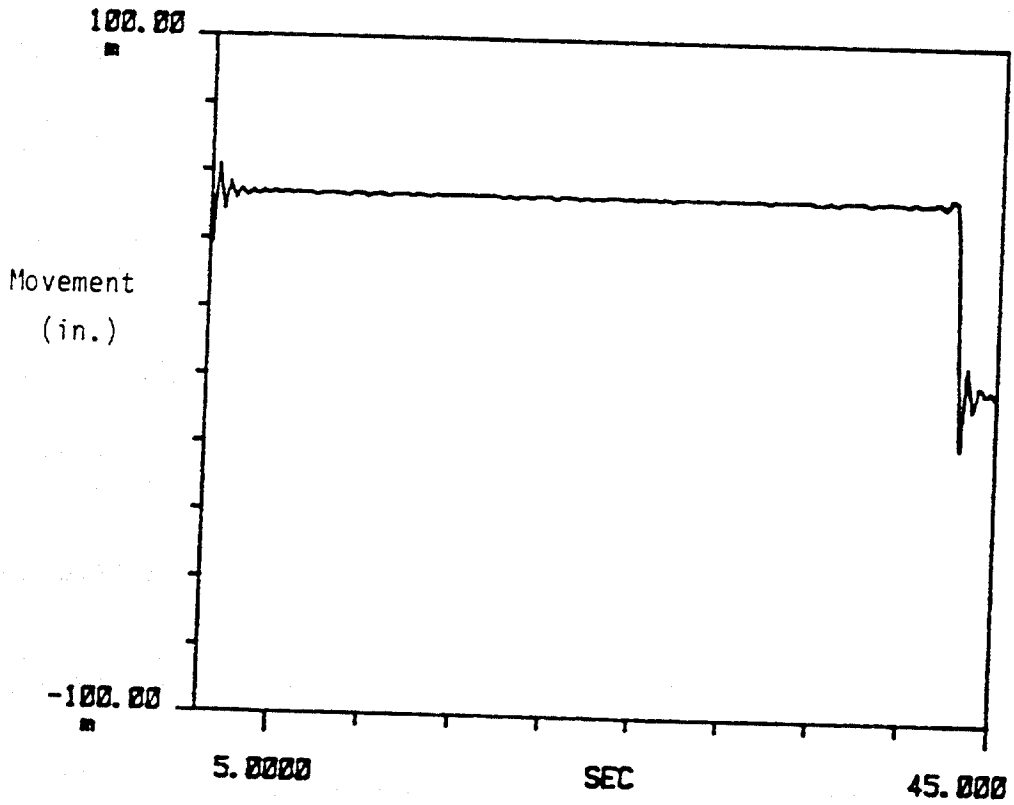

Fig. F.9. Time History Measurements of Pile Head Movement, Test I1, [m = milli].

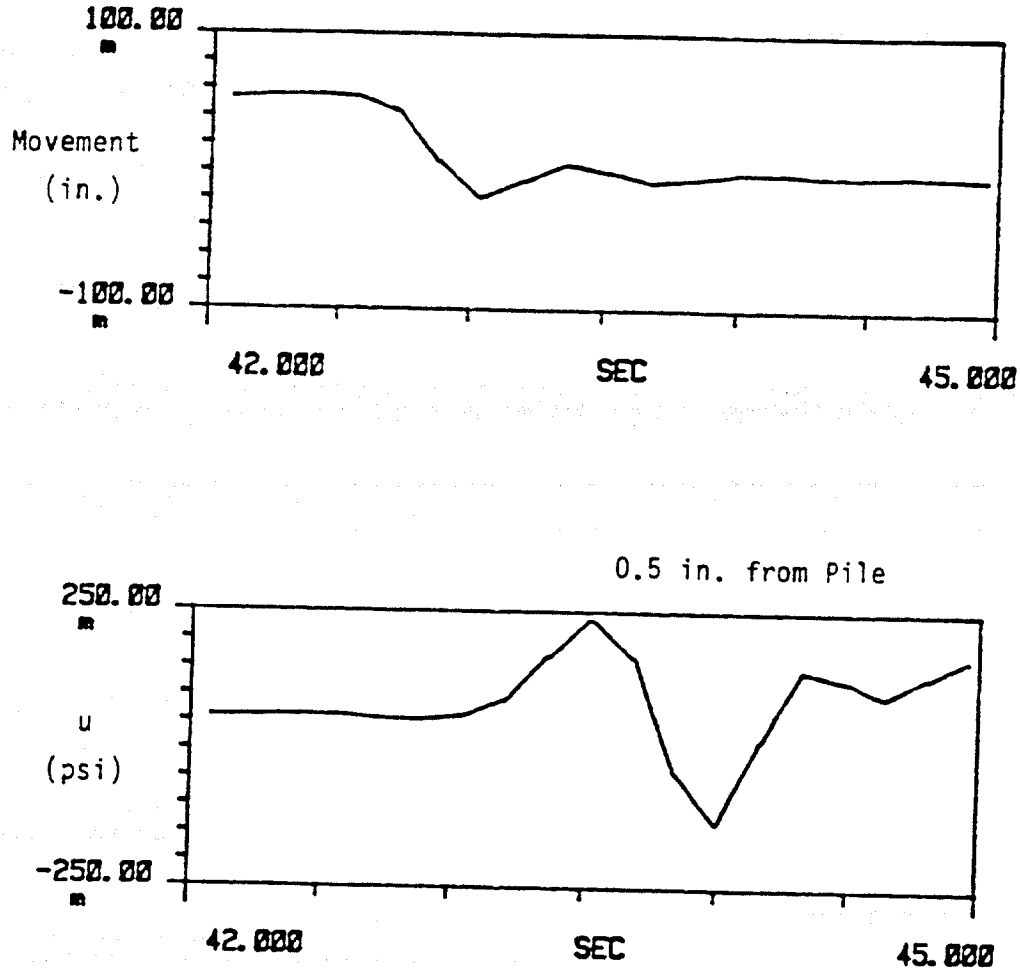

Fig. F.10. Time History Measurements of Pile Head Movement and Near Field Pore Water Pressure, Test I1, [m = milli].

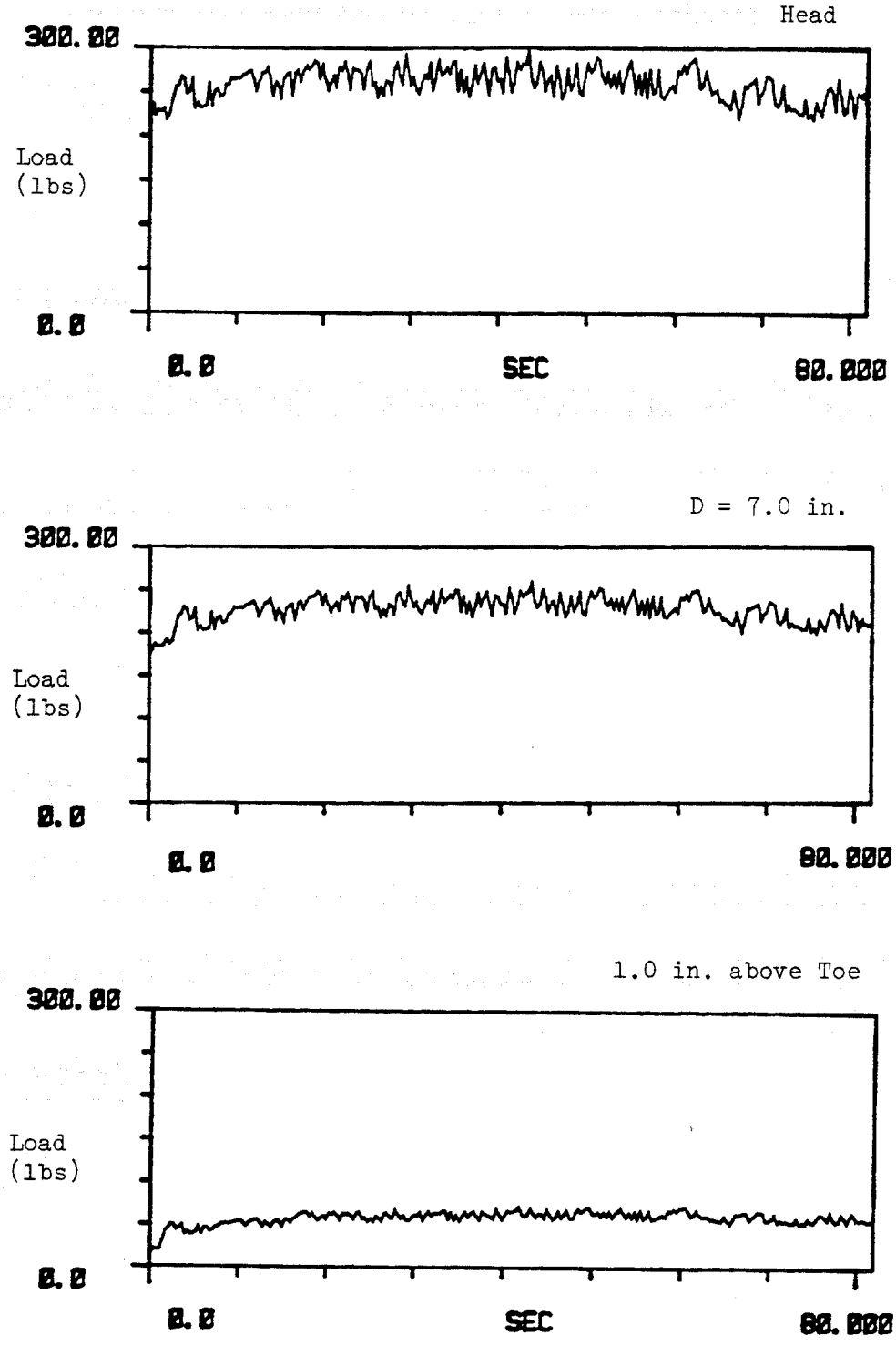

Fig. F.11. Time History Measurements of Dynamic Load on Pile, Test J.

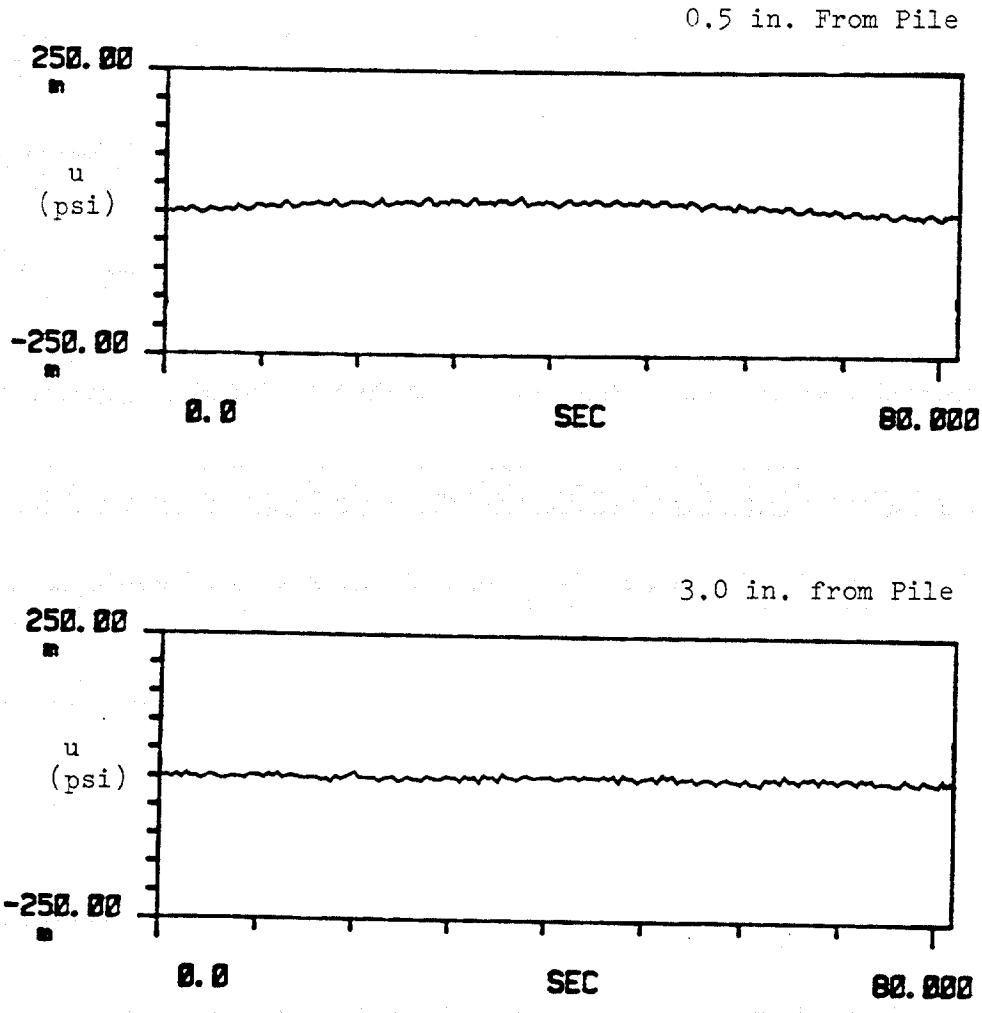

Fig. F.12. Time History Measurements of Near and Far Field Pore Water Pressures, Test J, [m = milli].

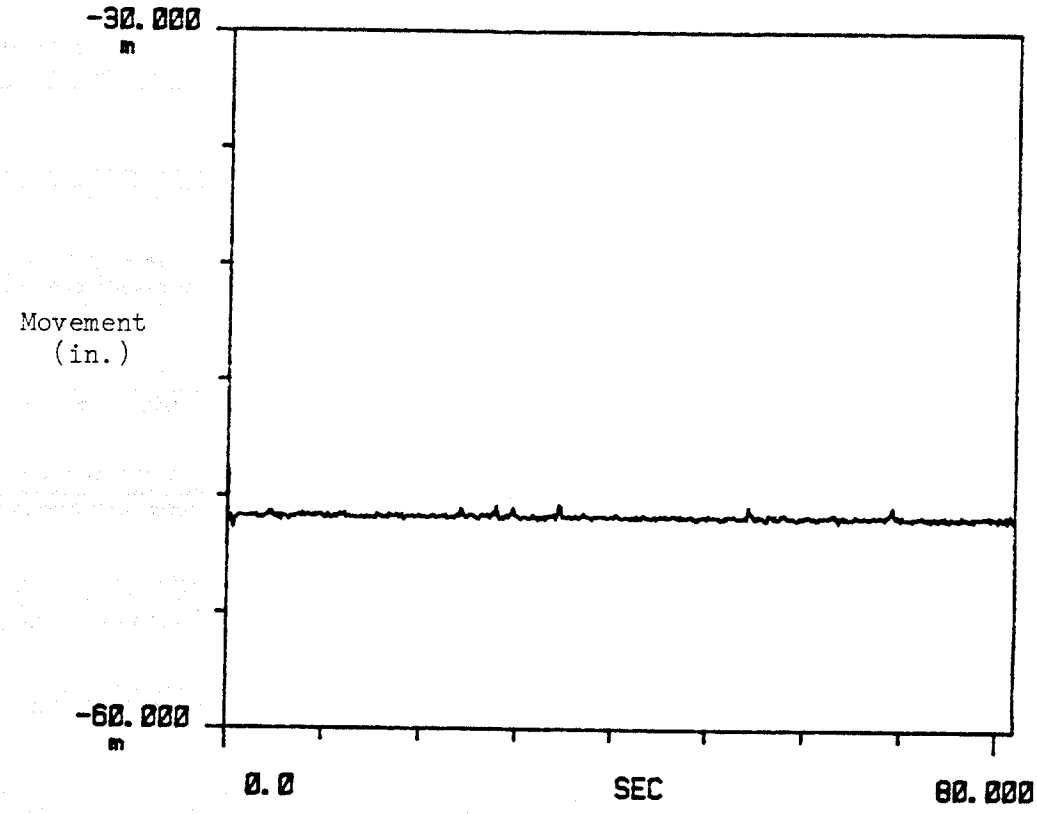

Fig. F.13. Time History Measurements of Pile Head Movement, Test J, [m = milli].

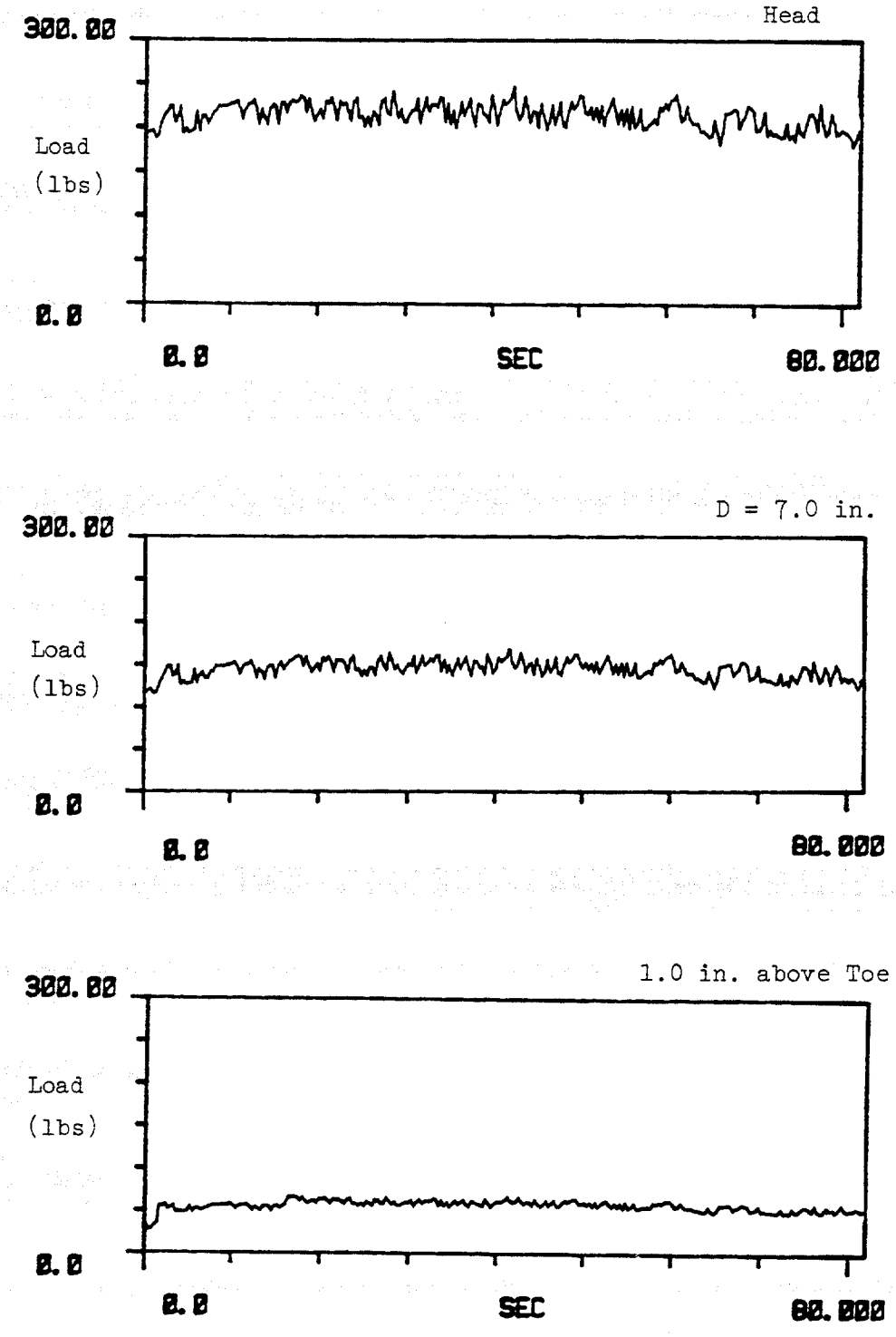

Fig. F.14. Time History Measurements of Dynamic Load on Pile, Test L1.

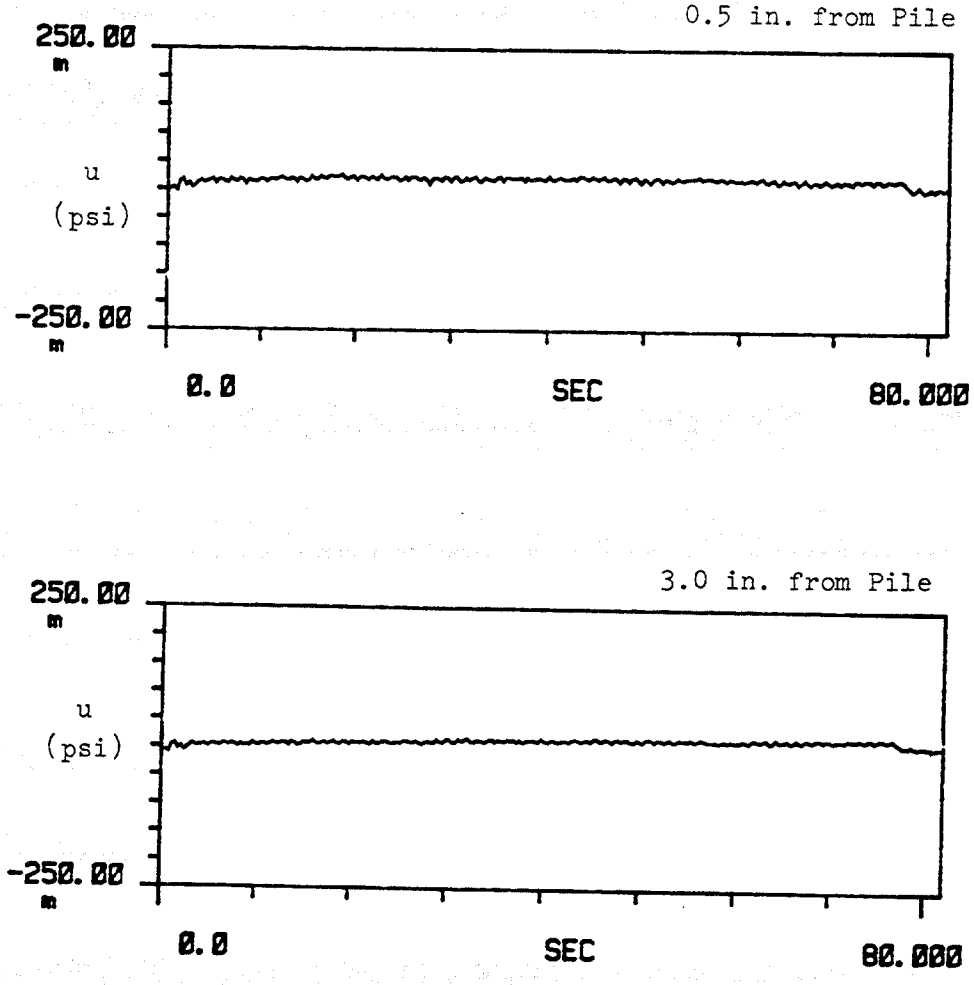

Fig. F.15. Time History Measurements of Near and Far Field Pore Water Pressures, Test L1, [m = milli].

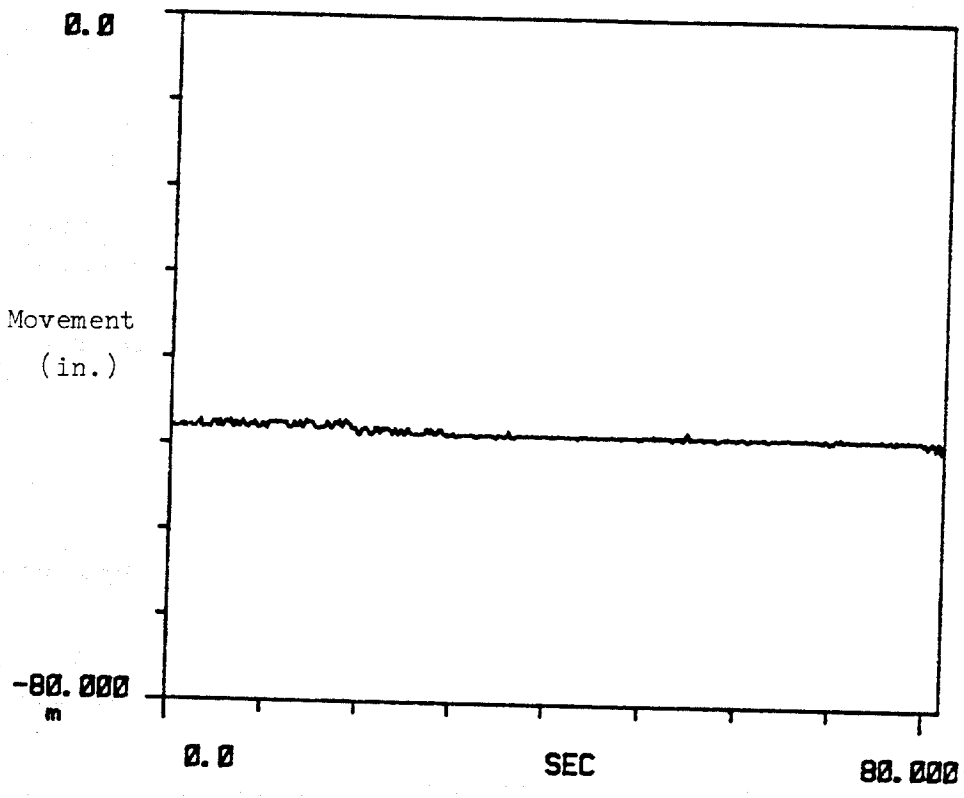

Fig. F.16. Time History Measurements of Pile Head Movement, Test J, [m = milli].

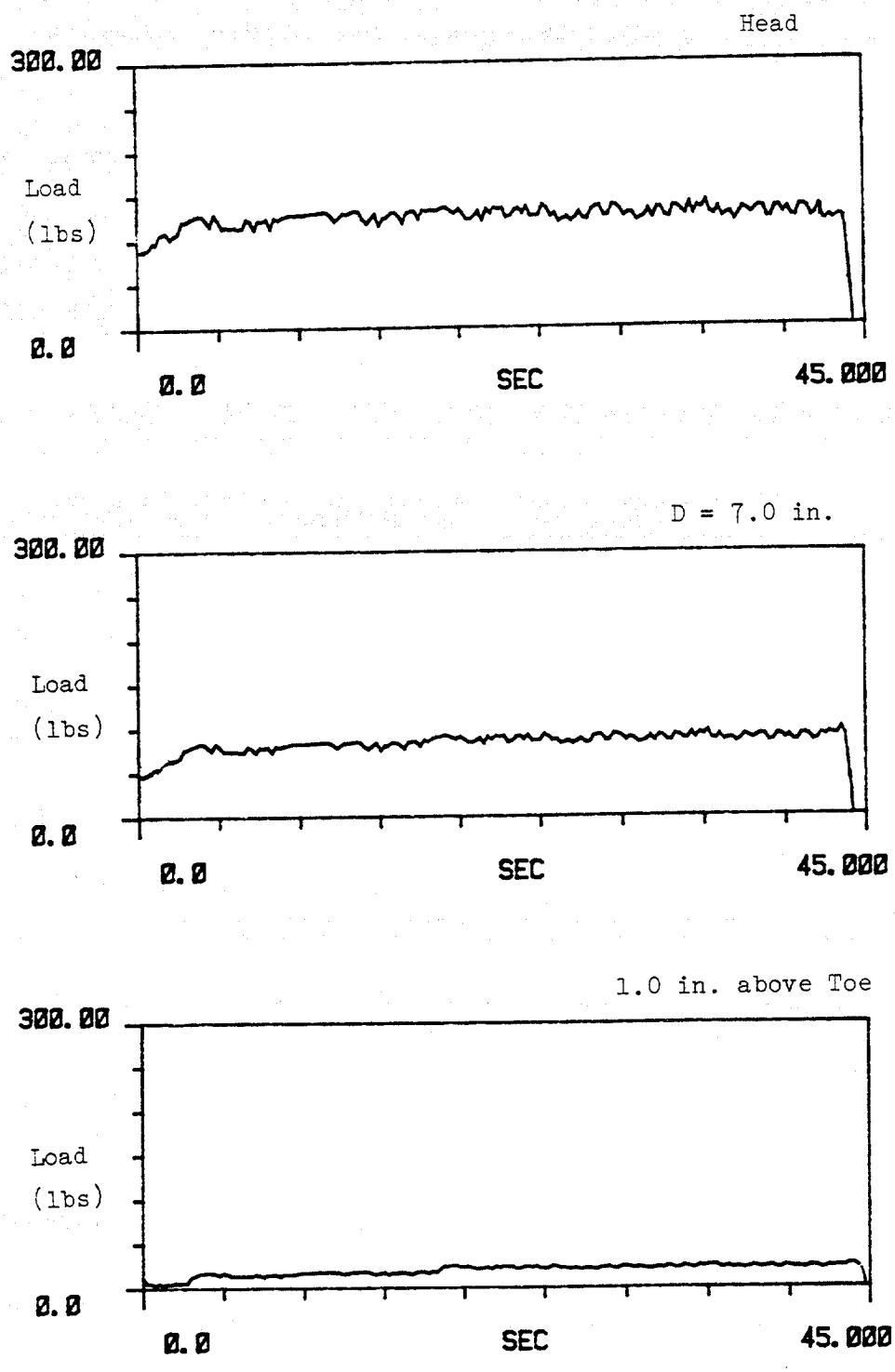

Fig. F.17. Time History Measurements of Dynamic Load on Pile, Test L2.

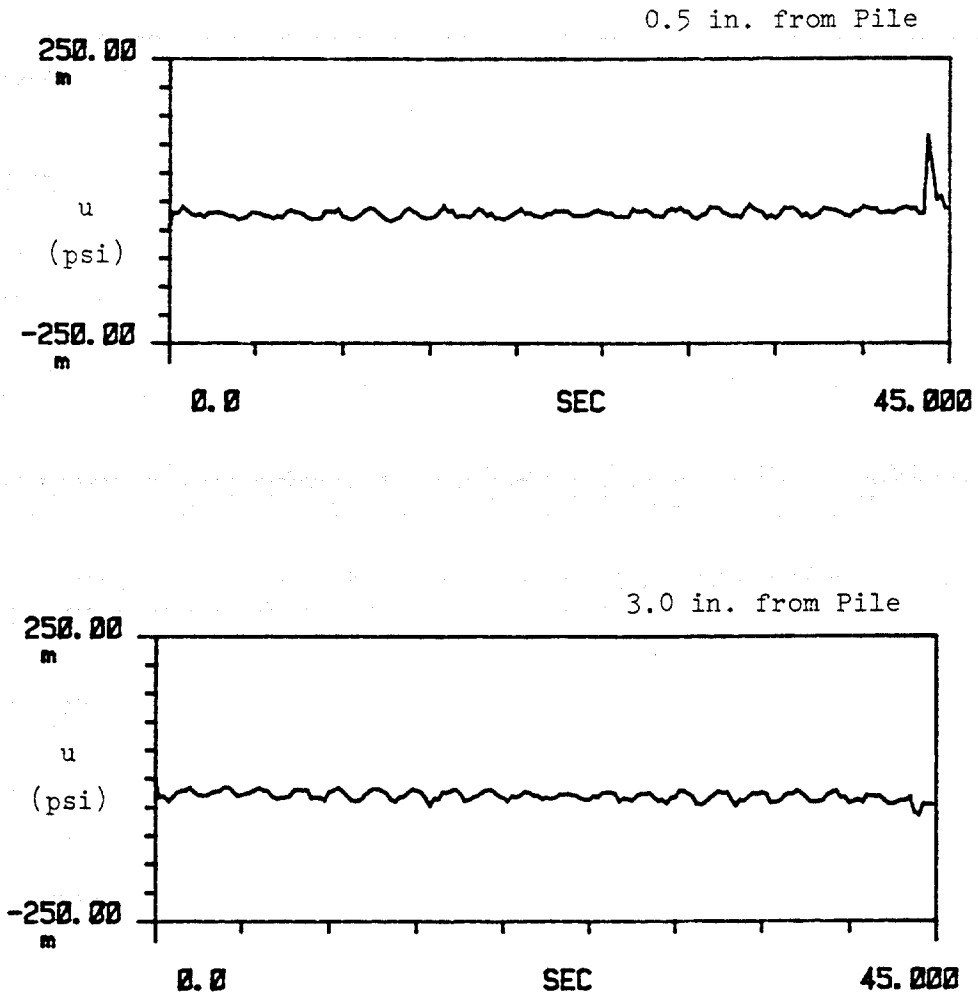

Fig. F.18. Time History Measurements of Near and Far Field Pore Water Pressures, Test L2, [m = milli].

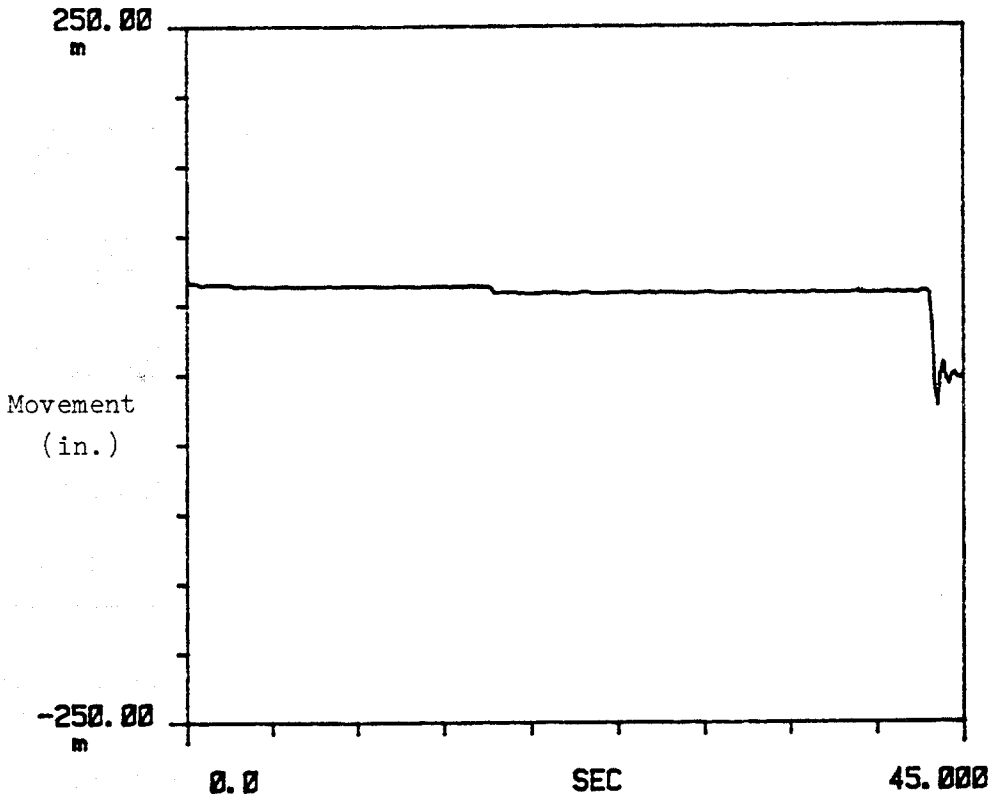

Fig. F.19. Time History Measurements of Pile Head Movement, Test L2, [m = milli].

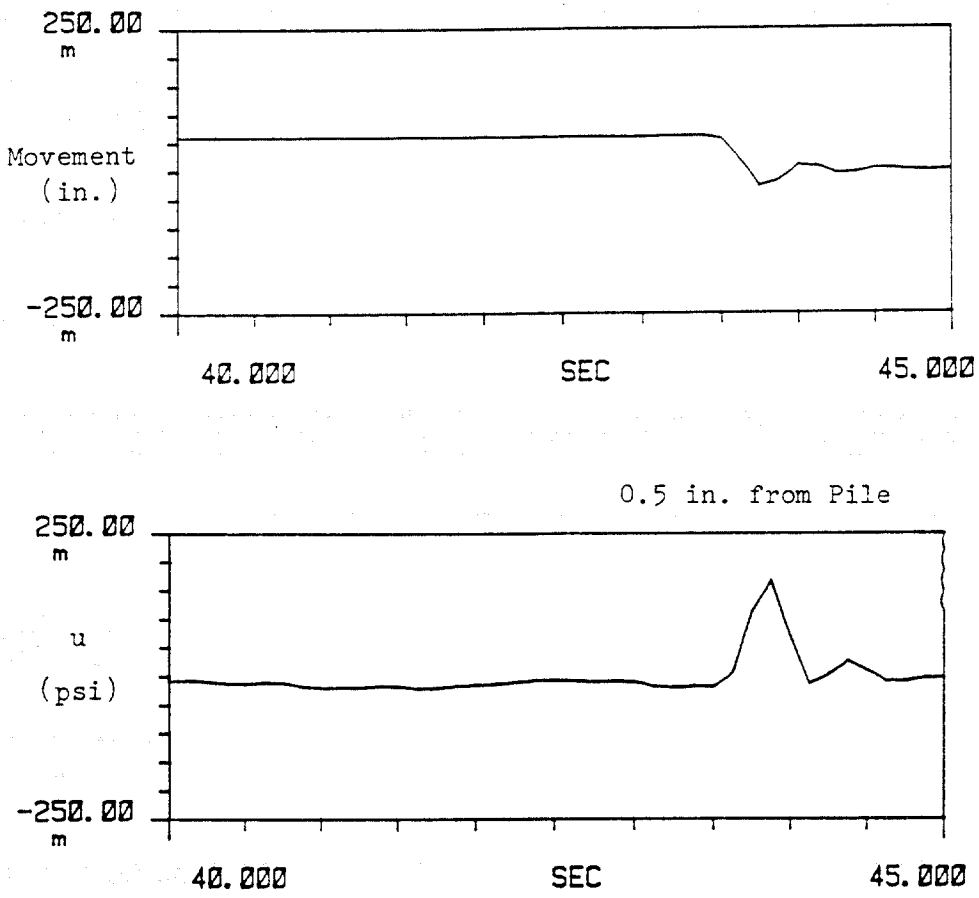

Fig. F.20. Time History Measurements of Pile Head Movement and Near Field Pore Water Pressure, Test L2, [m = milli].

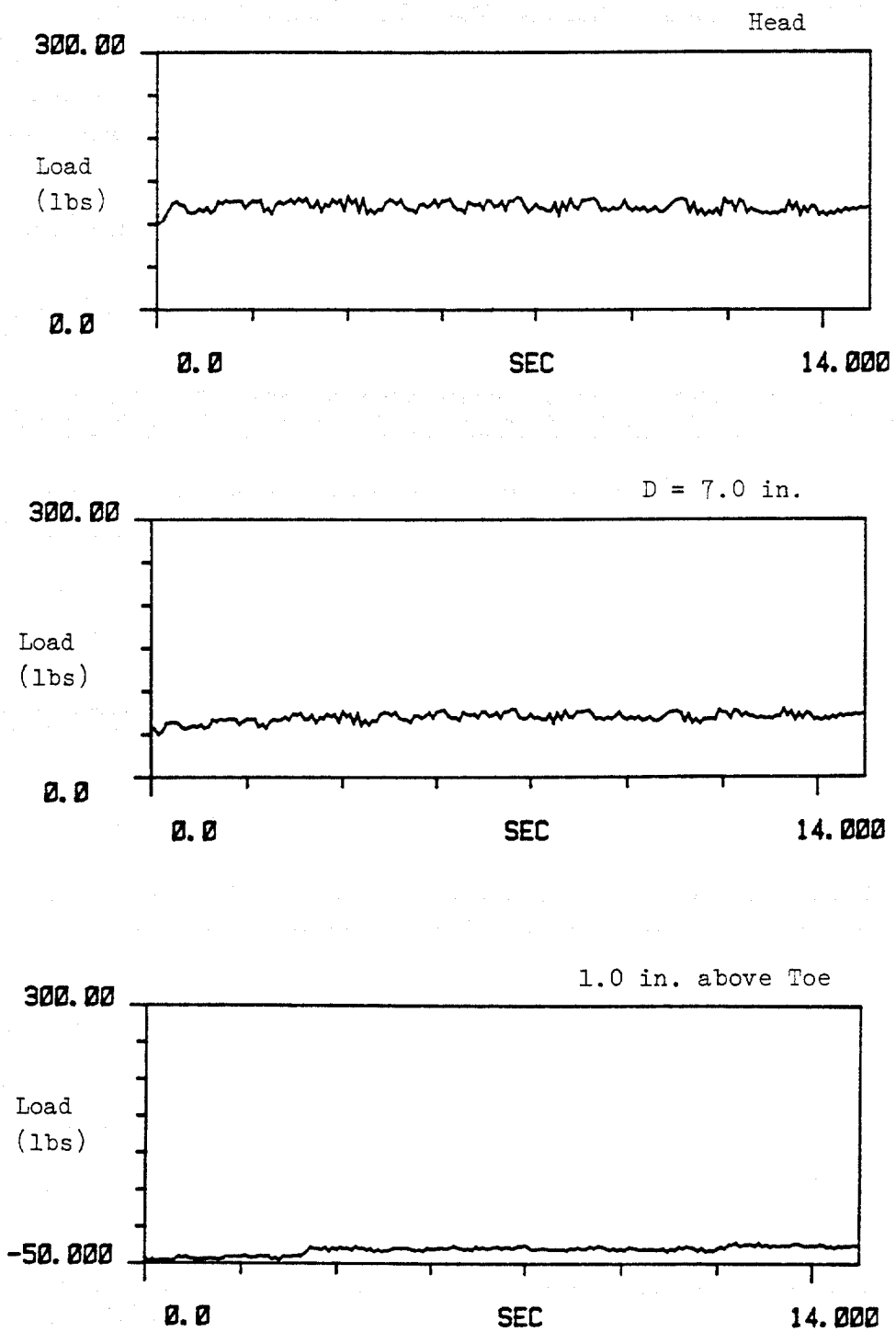

Fig. F.21. Time History Measurements of Dynamic Load on Pile, Test M1.

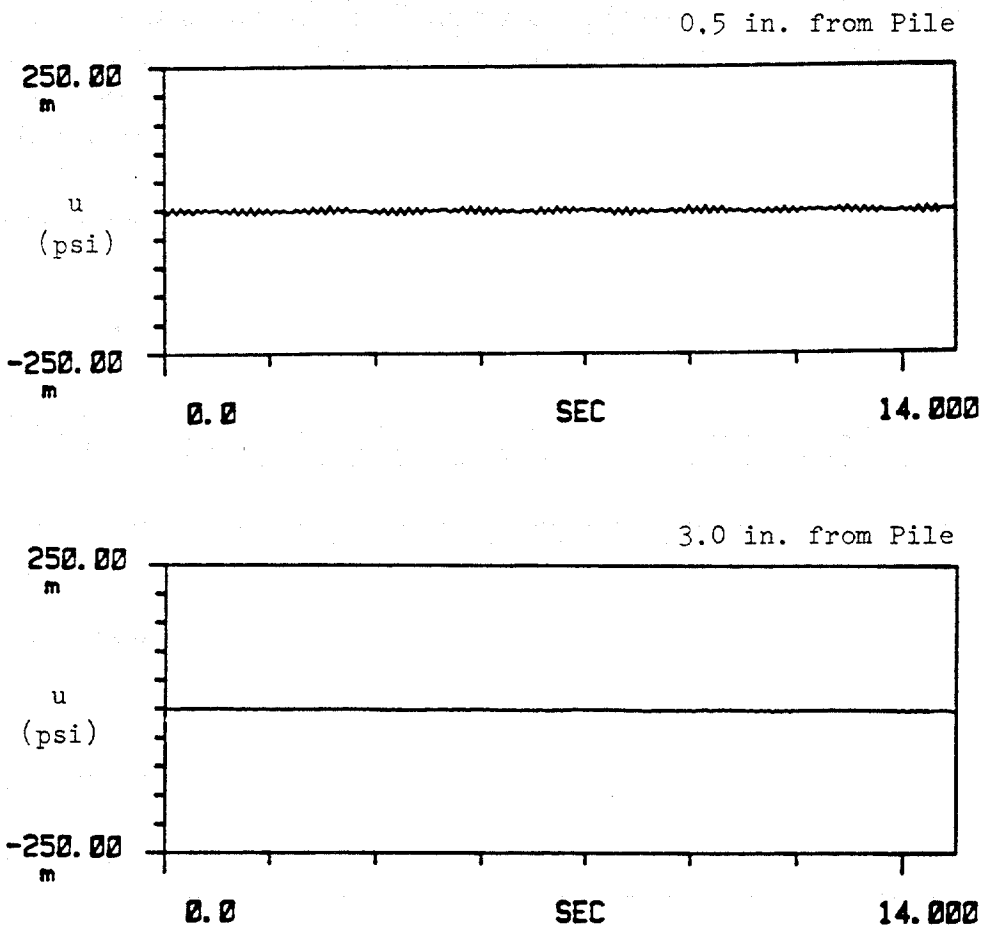

Fig. F.22. Time History Measurements of Near and Far Field Pore Water Pressures, Test M1, [m = milli].

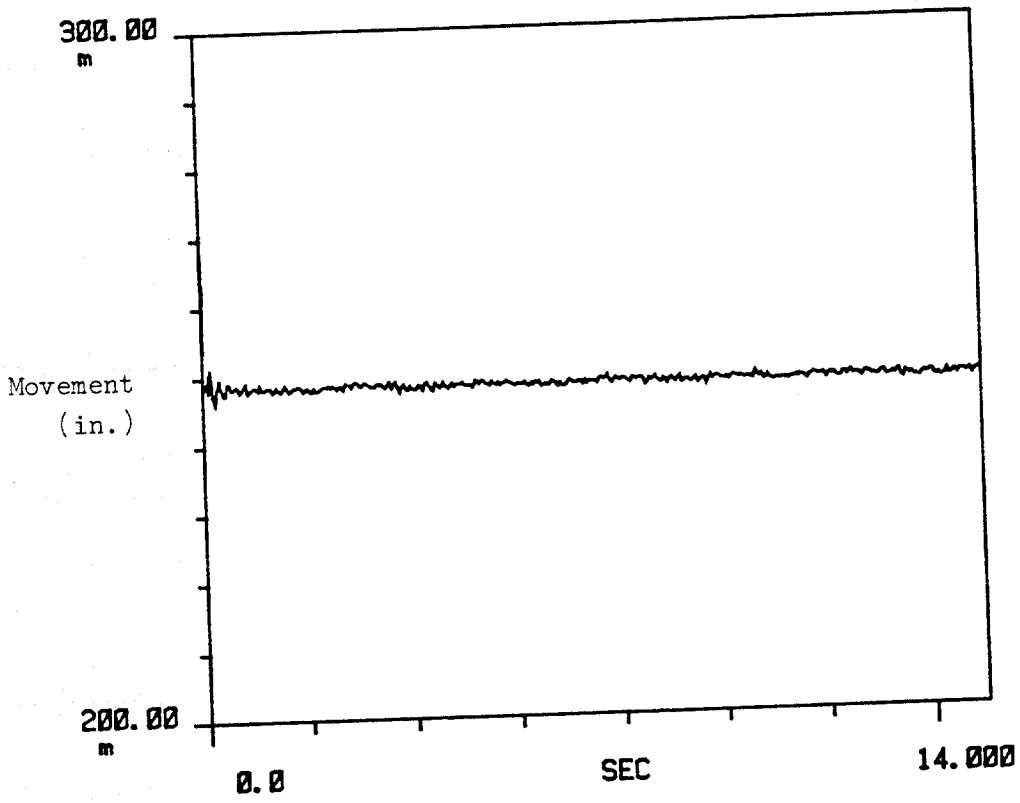

Fig. F.23. Time History Measurements of Pile Head Movement, Test M1, [m = milli].

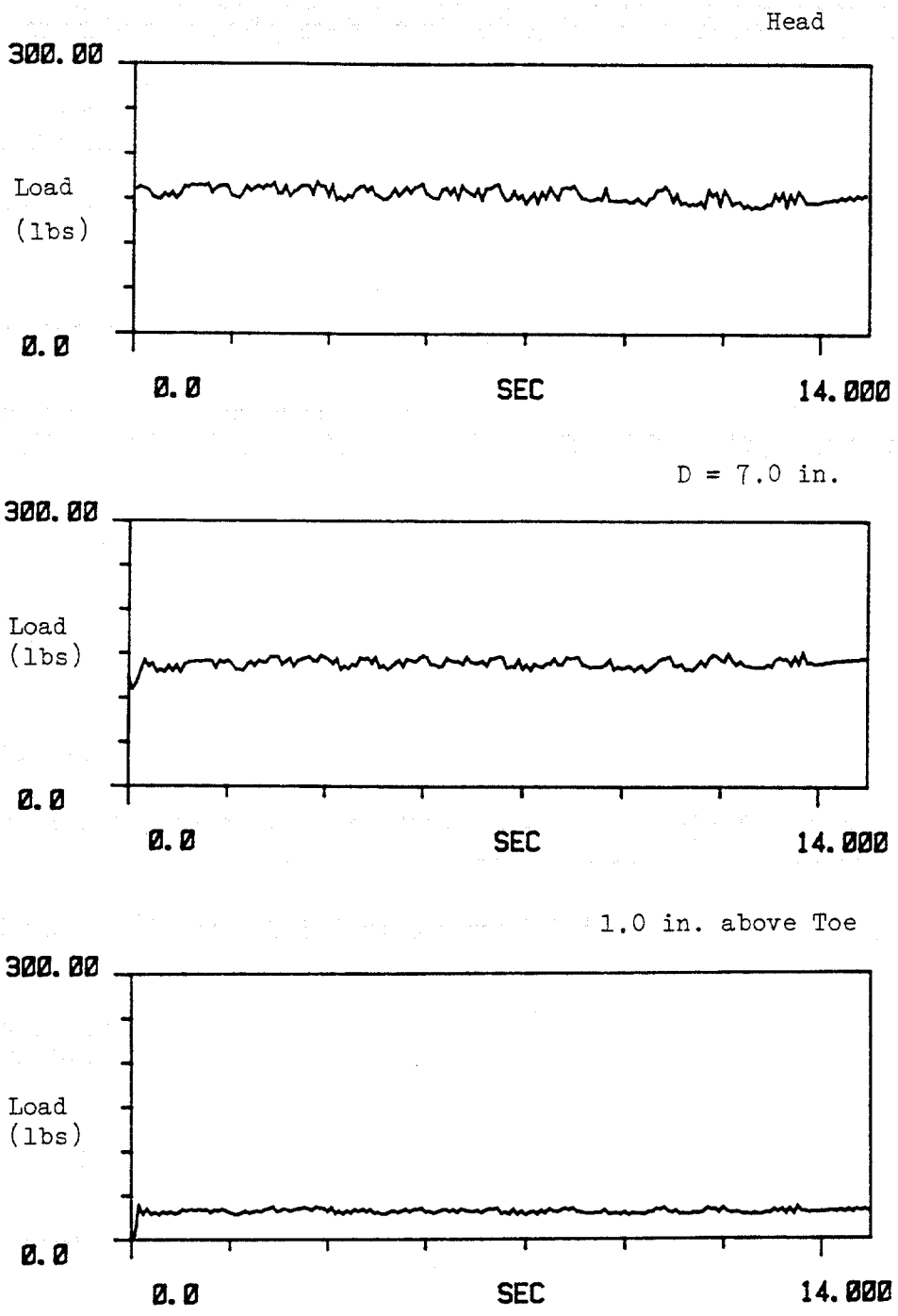

Fig. F.24. Time History Measurements of Dynamic Load on Pile, Test M2.

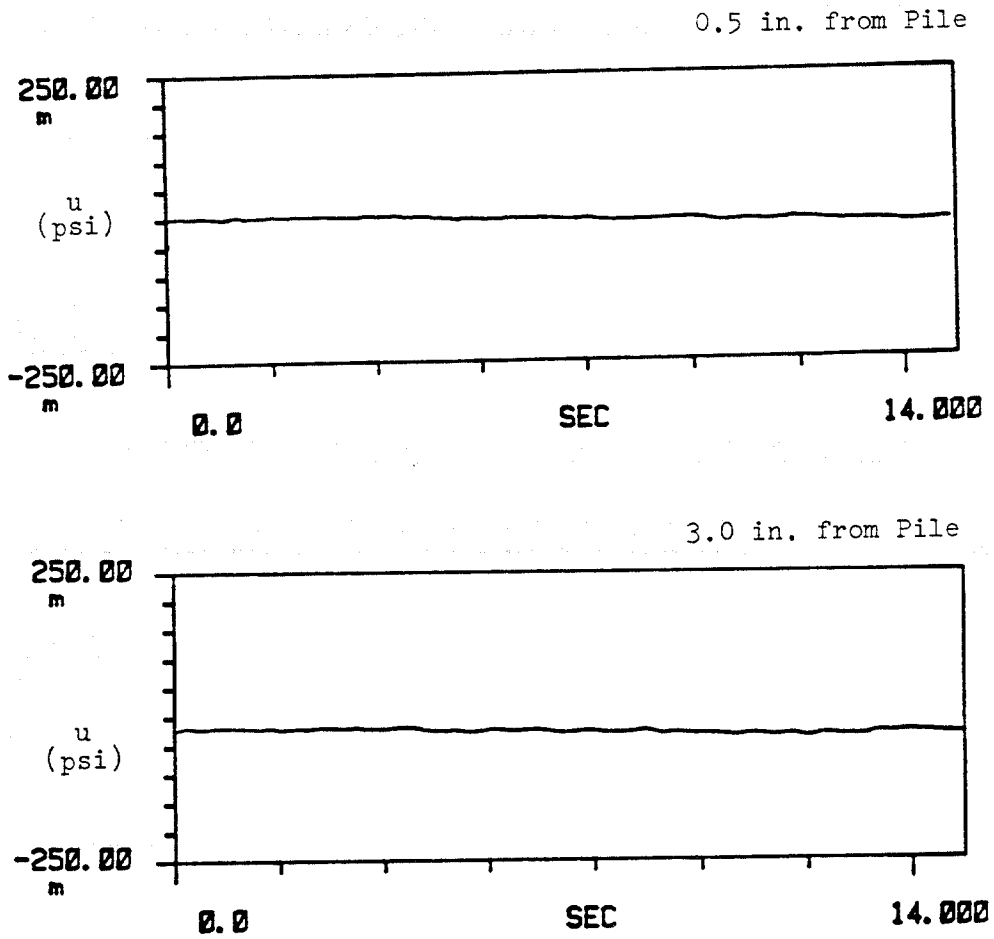

Fig. F.25. Time History Measurements of Near and Far Field Pore Water Pressures, Test M2, [m = milli].

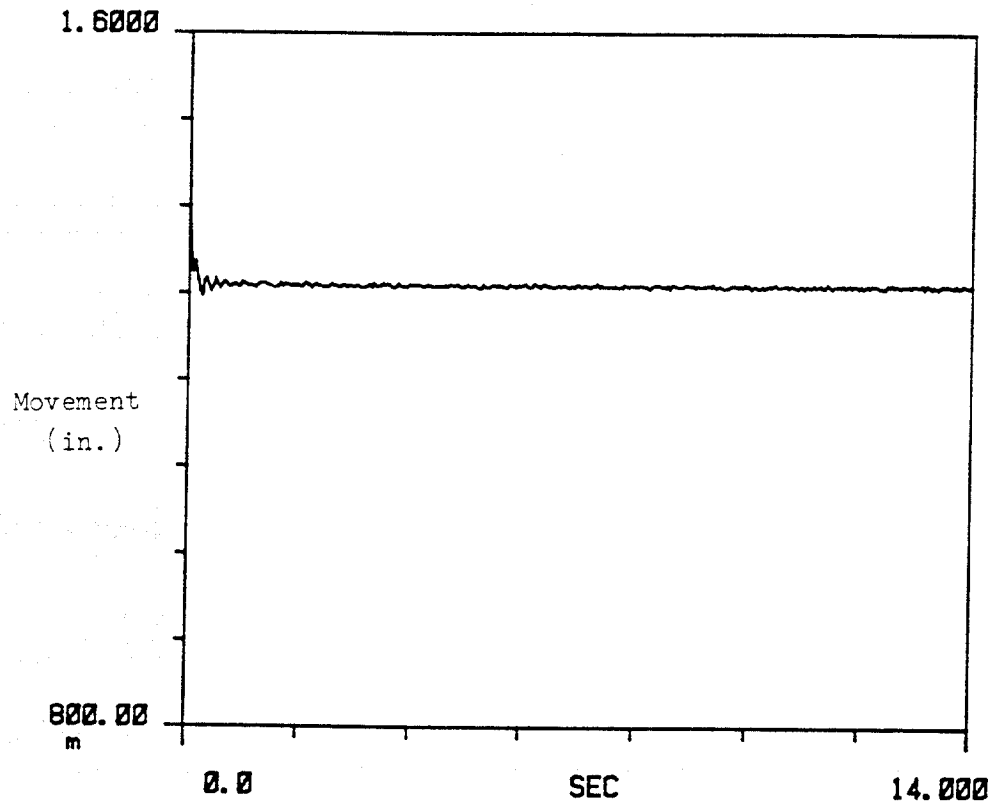

Fig. F.26. Time History Measurements of Pile Head Movement, Test M2, [m = milli].

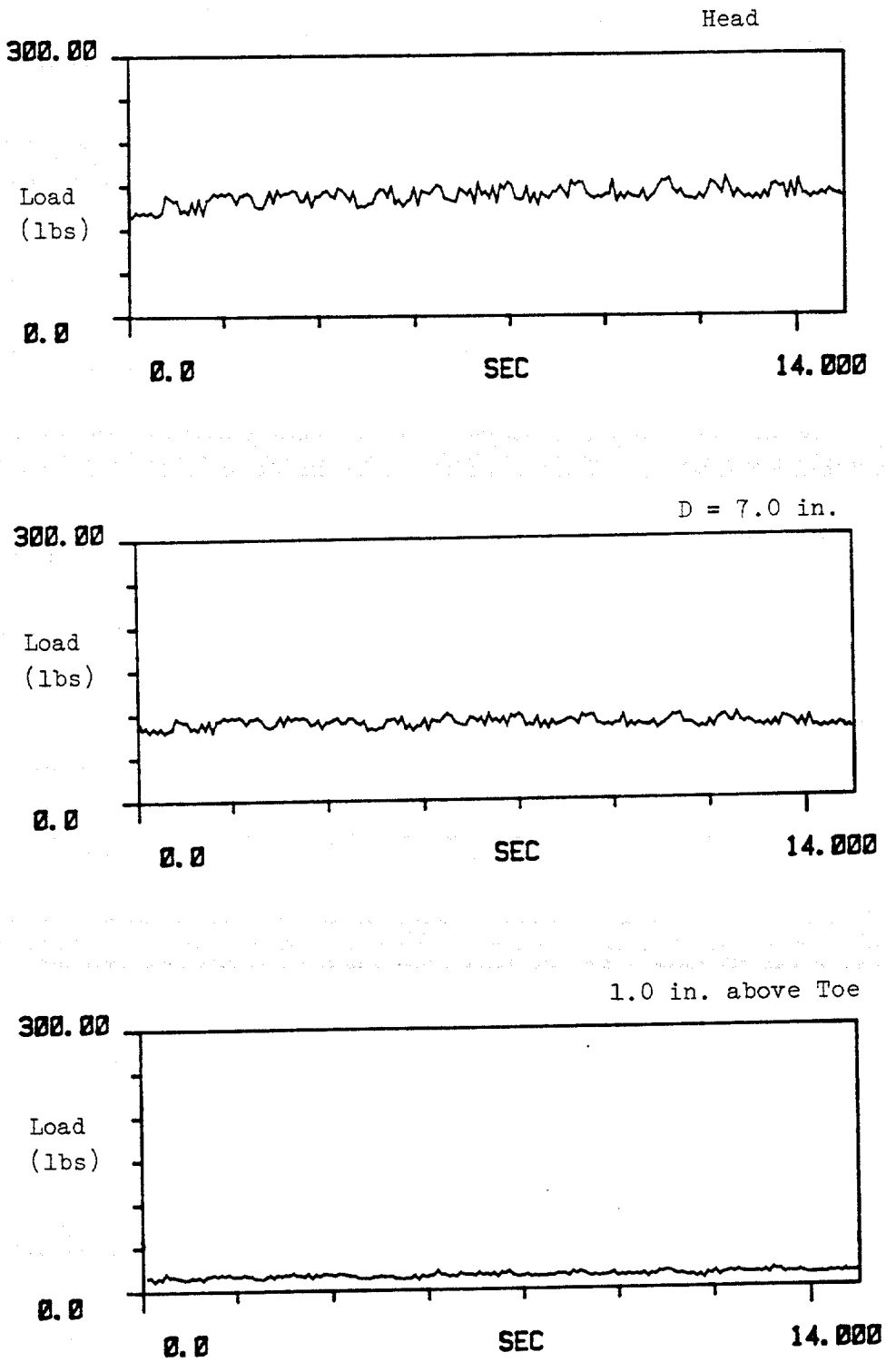

Fig. F.27. Time History Measurements of Dynamic Load on Pile, Test N1.

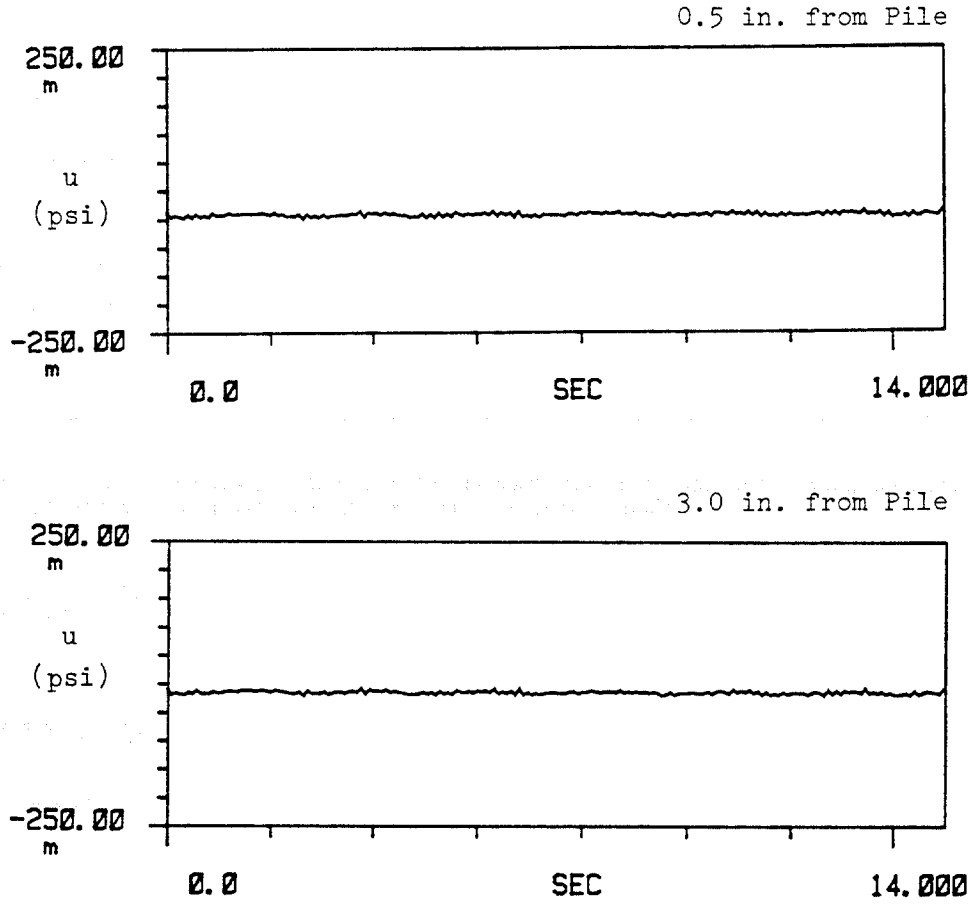

Fig. F.28. Time History Measurements of Near and Far Field Pore Water Pressures, Test N1, [m = milli].

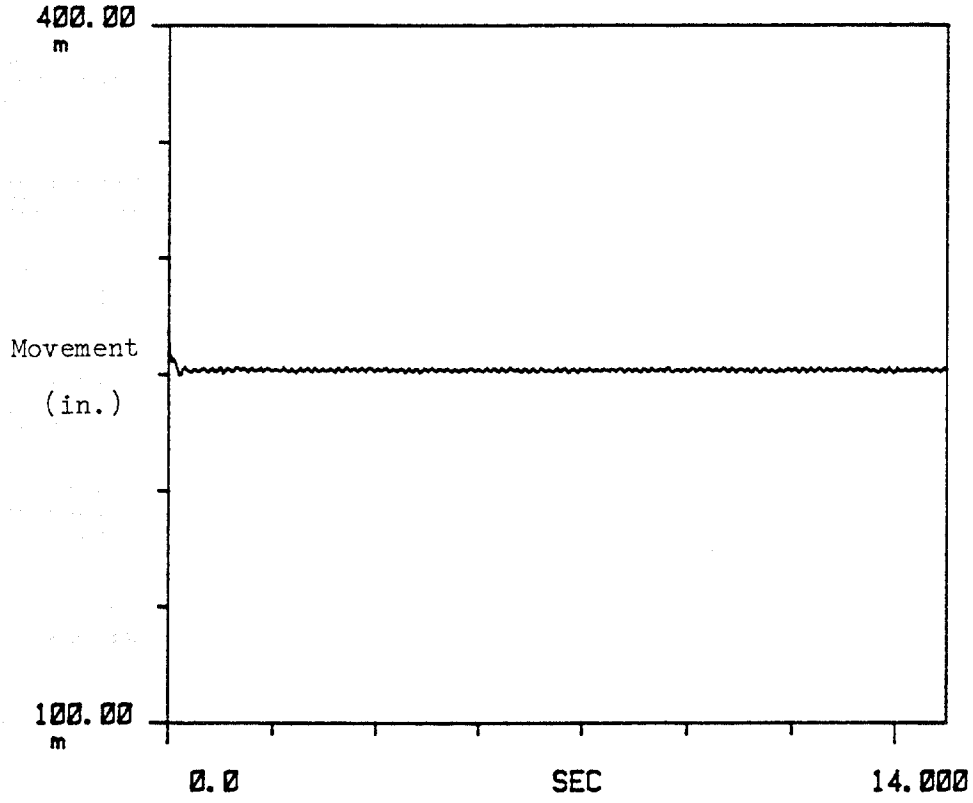

Fig. F.29. Time History Measurements of Pile Head Movement, Test N1, [m = milli].

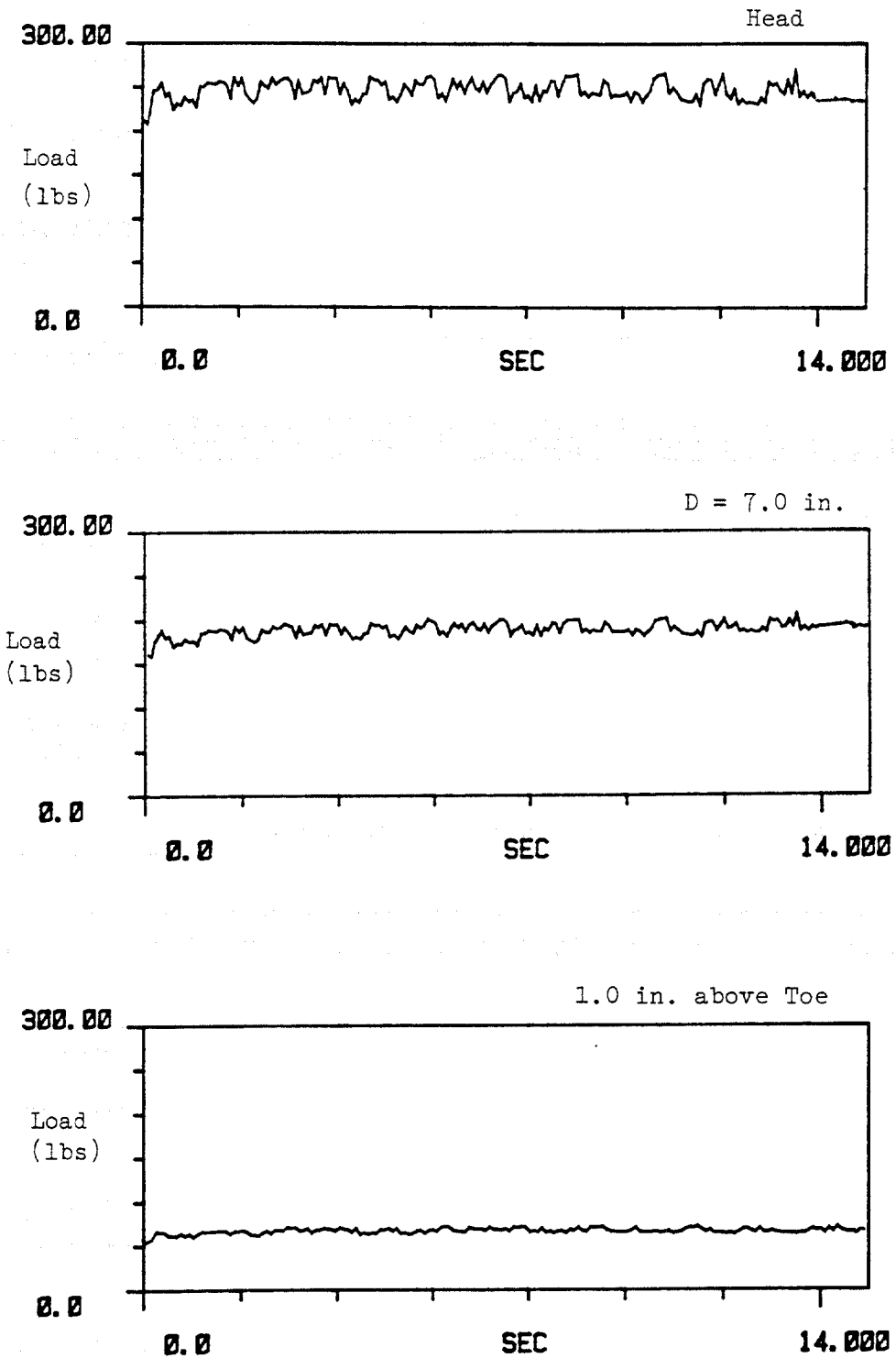

Fig. F.30. Time History Measurements of Dynamic Load on Pile, Test N2.

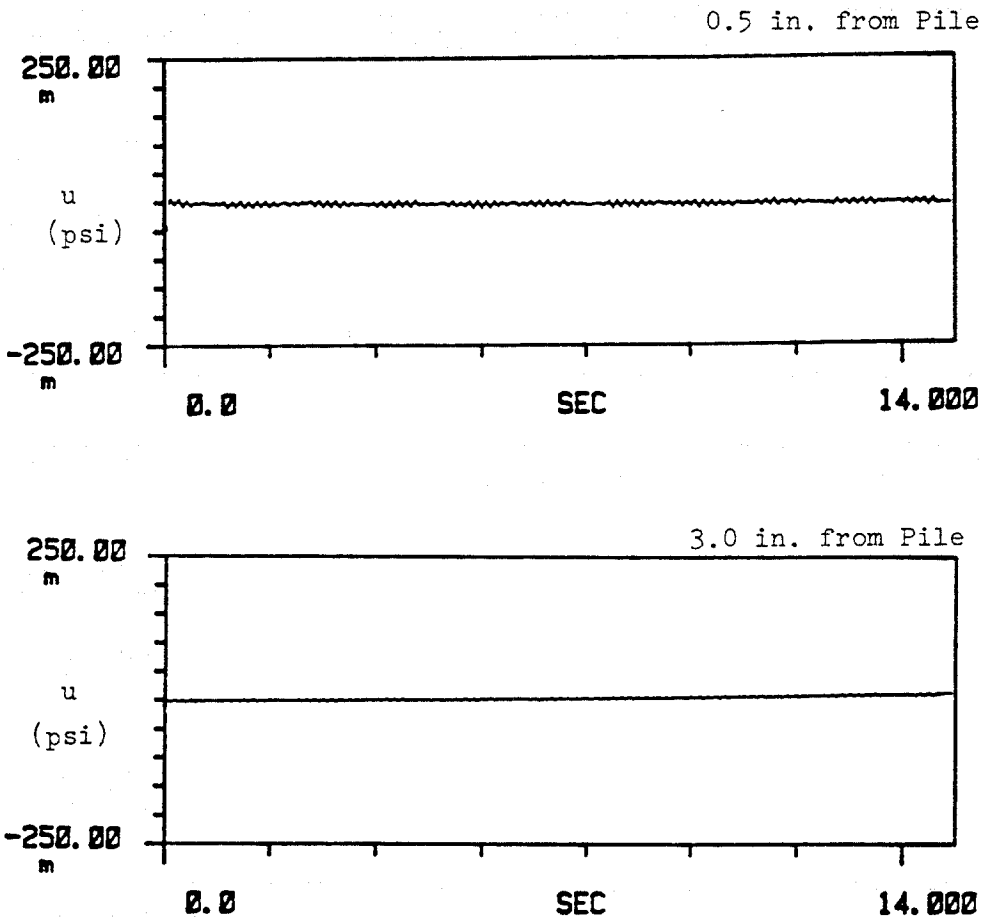

Fig. F.31. Time History Measurements of Near and Far Field Pore Water Pressures, Test N2, [m = milli].

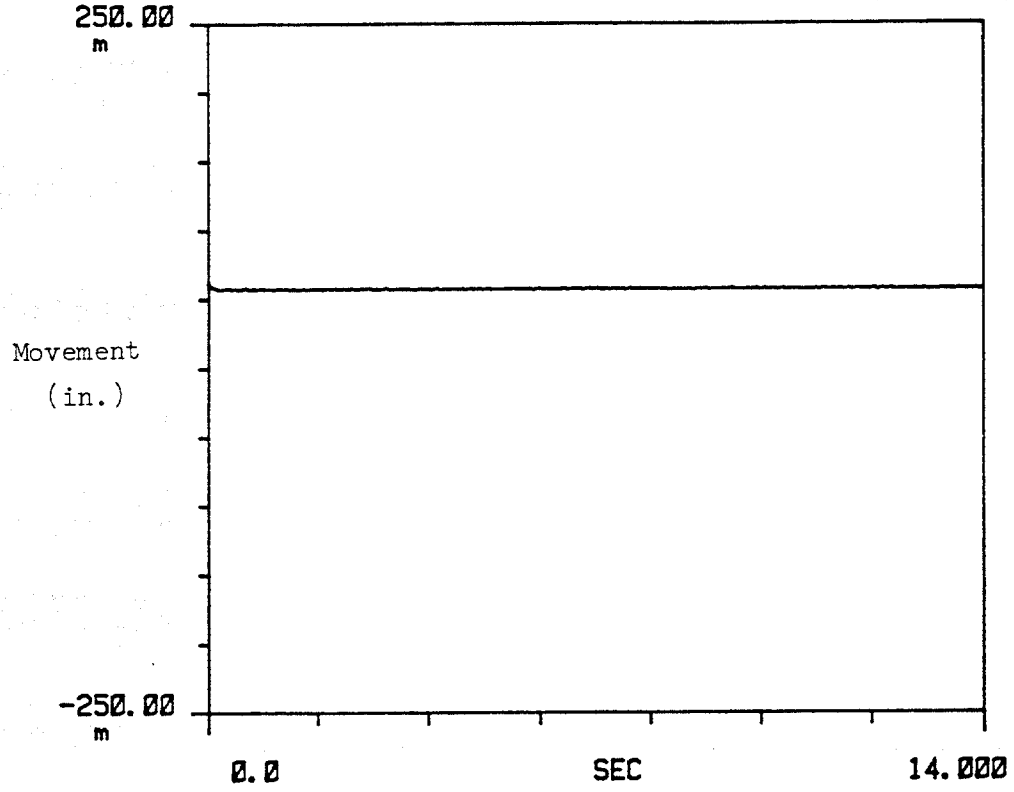

Fig. F.32. Time History Measurements of Pile Head Movement, Test N2, [m = milli].